MRI-based evaluation of MR-HIFU induced thermal effects
PhD thesis, Utrecht University, The Netherlands

The research in this thesis was performed in part within the framework of CTMM, the Center for Translational Molecular Medicine (www.ctmm.nl), project HIFU-CHEM (grant 03O-301).

ISBN: 978-90-393-6490-1
Cover & lay-out: Miekee Lam
Printing: Ridderprint BV

MRI-BASED EVALUATION OF MR-HIFU INDUCED THERMAL EFFECTS

MRI-GEBASEERDE EVALUATIE VAN DOOR MR-HIFU GEÏNDUCEERDE THERMISCHE EFFECTEN

(met een samenvatting in het Nederlands)

PROEFSCHRIFT

ter verkrijging van de graad van doctor aan de Universiteit Utrecht op gezag van de rector magnificus, prof.dr. G.J. van der Zwaan, ingevolge het besluit van het college voor promoties in het openbaar te verdedigen op maandag 14 maart 2016 des middags te 2.30 uur

door

MIE KEE LAM

geboren op 17 juli 1986
te Amersfoort

Promotoren:	prof. dr. ir. M.A. Viergever prof. dr. C.T.W. Moonen
Copromotor:	dr. ir. L.W. Bartels

CONTENTS

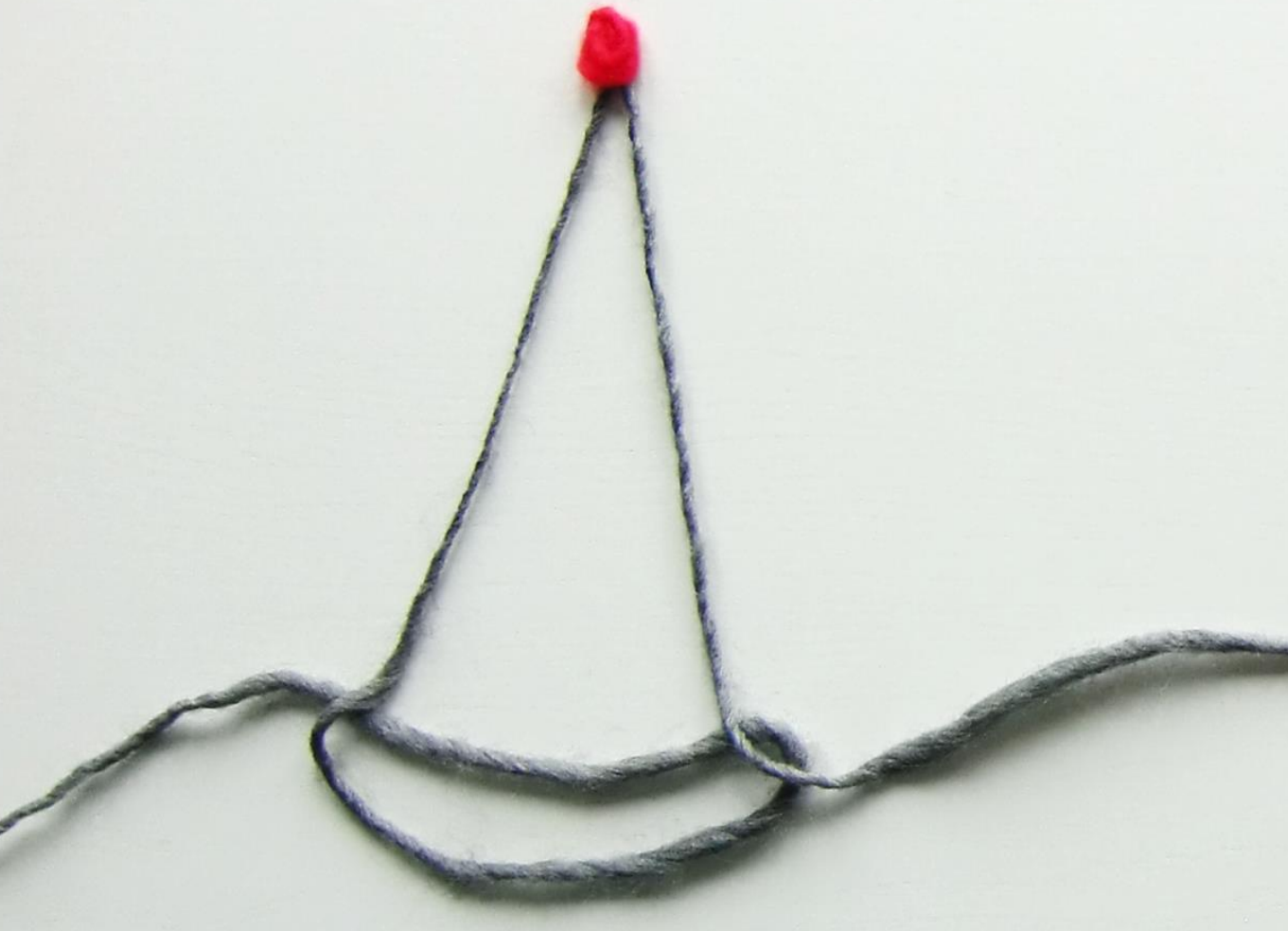

"THE FIRST PRINCIPLE IS THAT YOU MUST NOT FOOL YOURSELF

AND YOU ARE THE EASIEST PERSON TO FOOL"

– RICHARD P. FEYNMAN

Chapter 1

General introduction

MR-HIFU THERMAL THERAPY IN ONCOLOGY

In oncology, the standard treatment options are surgery, radiation therapy and chemotherapy. These are often combined to deliver optimal care for patients with cancer. In such combined treatment protocols, radiation therapy and systemic chemotherapy are usually applied as a (neo)adjuvant to surgical removal of the tumor mass (1). Thermal therapy has been proposed as an adjunctive therapy to various cancer treatments such as radiation therapy and systemic chemotherapy (2,3). With mild hyperthermia treatments, tissues are heated to temperatures between 40°C to 45°C for time periods up to an hour, inducing physiological effects without instantaneous damage to the tissue (4,5). One of the physiological effects is the improvement of tumor oxygenation, which has been reported to increase the effectiveness of radiotherapy (6,7). Other physiological effects are changes in blood flow and vascular permeability, which could enhance local drug delivery of chemotherapeutic agents (8,9). For these purposes, it would be preferable to induce mild hyperthermia locally at the tumor. Thermal ablation, a local high-temperature thermal therapy, has been proposed as an alternative to traditional surgery (10). By heating the targeted tissue until a lethal thermal dose has been reached, coagulative necrosis can be induced (11,12). Different types of energy sources may be used for local thermal therapies, including laser (13), radiofrequency ablation (14) and high intensity focused ultrasound (HIFU) (15).

MAGNETIC RESONANCE-GUIDED HIGH INTENSITY FOCUSED ULTRASOUND (MR-HIFU)

HIFU provides the opportunity to achieve non-invasive local heating. Ultrasound waves, generated by a piezoelectric transducer, are focused into a small volume called the focus, as illustrated in Figure 1a. By focusing the ultrasound waves, acoustic energy of high intensity can be locally deposited at the focus. Depending on the energy absorption, this will lead to thermal effects and non-thermal effects (16). Thermal effects can be distinguished in the direct heating process and the indirect physiological effects, such as coagulation, changes in perfusion and vessel shut-down (17,18).

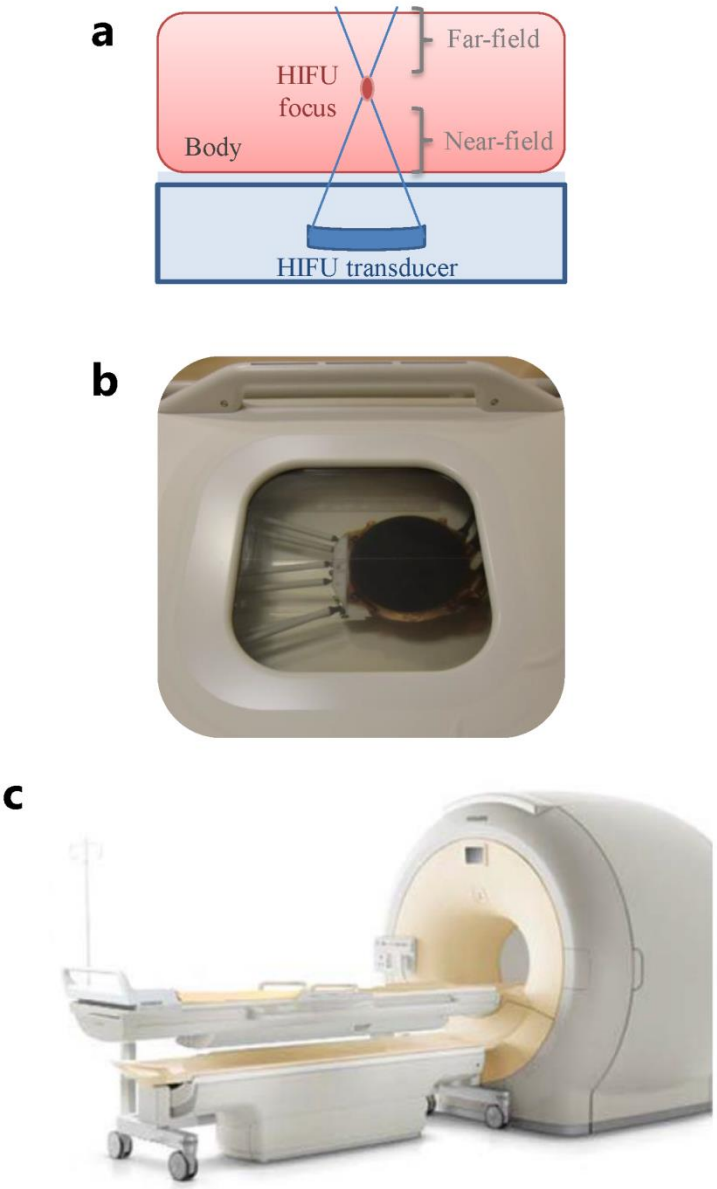

Figure 1. Overview of an MR-HIFU system: a) Illustration of focused ultrasound waves, propagating through the body into a focus; b) HIFU transducer embedded in an MR tabletop. c) Clinical MR-HIFU system integrated into an MR scanner (Image Courtesy: Philips Healthcare, Vantaa, Finland).

HIFU treatments can be guided using magnetic resonance imaging (MRI), which allows high resolution imaging with excellent soft tissue contrast (19) and temperature imaging (20). In clinical magnetic resonance-guided HIFU (MR-HIFU) systems, the HIFU transducer is embedded in a tank filled with water or oil and integrated into an MR tabletop (Figure 1b) (21). By using the MR-HIFU system (Figure 1c), MRI can be used for treatment planning, real-time monitoring of the heating process and evaluation the treatment effects (22-24).

MR THERMOMETRY

Tissue temperature changes are a direct measure of the heating process. There are several MR parameters that are temperature dependent, such as the resonance frequency, proton density, the longitudinal relaxation time (T1) and the transverse relaxation time (T2). A lot of work has been done develop MR methods which allow temperature mapping via these parameters, using MR sequences that were specially developed for this purpose (25-31).

The most commonly used method in clinic is the proton resonance frequency shift (PRFS) MR thermometry (MRT) (23). The method is based on the temperature dependent magnetic resonance frequency of hydrogen nuclei in water molecules. This is owing to the temperature dependence of the electron screening constant of hydrogen nuclei in water (32,33). The motion of water molecules increases with increasing temperature. Consequently, hydrogen bonds between hydrogen and oxygen are distorted and stretched, resulting in increased electron screening. Because of this, the resonance frequency of the hydrogen nuclei becomes lower (Figure 2) (34).

Measuring these resonance frequency changes in the frequency domain would seem the most obvious choice. However, the required spectroscopic MR sequences are typically slow and therefore not suitable for real-time monitoring (20). Instead, with PRFS MRT, the resonance frequency changes are measured from the phase changes of the complex MR signal at a certain echo time. Gradient-echo MR scans are used to dynamically acquire phase

maps. From the changes in phase, measured by subtracting subsequent phase map, relative temperature changes can be calculated (25,26). Because PRFS MRT is subtraction-based, the method is susceptible to non-temperature related changes in the phase, for instance those caused by motion. Absolute temperatures are calculated by adding the baseline temperature to the relative temperature changes measured with PRFS MRT. Since the exact temperature distribution at the imaging slice can usually not be determined, the patient's core temperature measured before the treatment procedure is generally used as the baseline temperature (35).

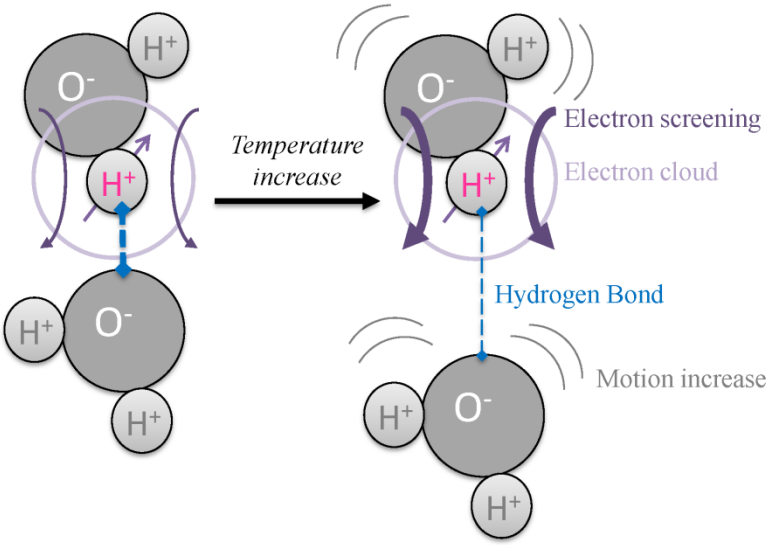

Figure 2. Illustration of the increased screening effect of hydrogen nuclei in water, as a result of temperature increase.

MR METHODS FOR MR-HIFU THERMAL THERAPIES

With thermally ablation treatments using MR-HIFU, generally the aim is to reach temperatures above 60°C for a few seconds (36). This combination of time and temperature will result in a lethal thermal dose leading to cell death, as was described by Sapareto and Dewey (11). Up to now, MR-HIFU has been approved for routine clinical uses for thermal ablation of uterine fibroids (37) and painful bone metastases (38). Thermal ablation of tumors in breast (39), liver (40), pancreas (41), prostate (42) and brain (43) is among the emerging oncological applications of MR-HIFU. For these applications, it is important to ensure that the whole target volume, covering the tumor and margins, receive a lethal thermal dose. Accurate temperature measurements are therefore required to further develop the MR-HIFU technology towards oncological applications of thermal ablation.

For the application of MR-HIFU induced mild hyperthermia (40°C to 45°C), real-time feedback control systems can be used (5,44,45). The measured MR temperatures are used as an input to control the applied ultrasound power. To achieve controlled mild hyperthermia in such a way that the temperature stays within a window of 40°C to 45°C, it is necessary to have accurate temperature measurements. As mentioned earlier, the indirect thermal effects of mild hyperthermia on the physiology were reported to enhance the therapeutic effect of chemotherapy and radiation therapy (6-9). In addition, mild hyperthermia can be used to achieve localized drug delivery in tumors using thermosensitive drug carriers. Pre-clinical MR-HIFU mild hyperthermia studies have been performed using low temperature-sensitive liposomes, which release the encapsulated chemotherapeutic drug upon being heated to mild hyperthermic temperatures (46,47). MRI can be used, as an alternative to histology, to determine the resulting damage (24). Tools to visualize the thermal effects on the physiology would be valuable, as they may provide insight in the expected treatment outcome.

While the current MR methodologies provide opportunities in monitoring and evaluation of MR-HIFU thermal therapies, further development is necessary to bring the technology closer to oncological applications in clinic.

THESIS OUTLINE

In this thesis, the focus is on MRI methods for the evaluation of MR-HIFU induced thermal effects. These thermal effects can be distinguished in two types: direct heating and the indirect physiological effects. The research was performed within the context of the HIFU-CHEM project carried out by a public-private consortium funded by the Dutch Center for Translational Molecular Medicine (CTMM). The purpose of the HIFU-CHEM project was to develop and test an MR-HIFU technology platform specifically for local drug delivery using thermosensitive liposomes. The primary clinical objective was to treat painful bone metastases.

PRFS MRT is the most commonly used method in the clinic to monitor MR-HIFU treatments, because of its high temporal resolution. The accuracy and precision of the temperatures measured may vary as they depend on several factors. In the clinic, the interest in the performance of PRFS MRT increased with the application of MR-HIFU as a palliative treatment of painful bone metastases. Clinical palliative MR-HIFU treatments of patients with painful bone metastases were performed in our hospital, as part of the clinical workpackage in the HIFU-CHEM project (48). In **CHAPTER 2**, we have evaluated the clinical performance of PRFS MRT used for monitoring MR-HIFU ablation procedures of these palliative treatments. This was done by retrospective analysis of the MRT data.

An emerging application of MR-HIFU is the treatment of tumors in abdominal organs. Since the liver, kidney and pancreas are well-perfused, relatively high acoustic power levels are needed (40,49-52). With mild hyperthermia, the required powers are lower, since lower temperatures are aimed for. However, the aimed temperatures should be achieved for longer periods of time. So even though lower powers are needed than for thermal ablation, consecutive exposures are required to keep the temperature within the aimed temperature window. In addition, consecutive sonications are also needed to cover the target volume. The combination of the high power levels and consecutive sonications may induce undesired cumulative thermal build-up in tissues outside the targeted region. This is especially true for the

tissue traversed by the HIFU beam on its way to the focus, the so-called near-field region of the HIFU beam. When targeting lesions in abdominal organs through an acoustic window in the ventral abdominal wall, the tissues potentially at risk in the near-field are the skin, subcutaneous fat layer and adjacent muscle layer. The presence of both fat and aqueous muscle tissue opens up the possibility to use the fat signal as a reference to the water signal; the resonance frequency of water is temperature dependent, but that of fat is not. By using fat as a reference, temperature measurements can be corrected for magnetic field drift (25) and absolute temperatures may be calculated (28,29). One way of using fat as a reference is by using the multi-gradient echo (MGE) MRT (29) method. Temperatures can be calculated from the difference frequency between water and fat by using a calibration value of the chemical shift difference between water and fat at a known temperature. When the two components contribute to the MR signal, by means of the partial volume effect, the modulus of the time-signal will oscillate with the frequency difference. With the MGE MRT method, temperatures are calculated from the frequency difference extracted from the time-signal sampled at multiple echo times, acquired with a gradient-echo sequence. In **CHAPTER 3**, we investigated the use of the MGE MRT method to monitor the temperature in the near-field area, using both absolute and relative temperature measurements.

For the calculation of absolute temperatures using MGE MRT, a calibration value is needed of the chemical shift difference between water and fat at a known temperature. However, this calibration value is dependent on the nuclear magnetic field of the two compartments. Due to the susceptibility difference between water and fat, the nuclear magnetic field may vary. Hence the used calibration value may not be correct everywhere, potentially inducing systematic errors in the absolute MGE MRT temperatures. **CHAPTER 4** is on a study in which the influence of the magnetic susceptibility difference between water and fat was investigated on the MGE MRT method. Spatial variations in magnetic susceptibility generate magnetic field inhomogeneities. Consequently, the sub-voxel magnetic resonance frequency distribution and the time-domain signal of the voxel are affected. The behavior of the time-domain signal of water in of sub-voxel magnetically

inhomogeneous systems has been described theoretically in the literature, showing different behavior on short and long time scales. We investigated the water and fat signal behavior in such systems with numerical simulations and explored the implications of the findings for absolute MGE MRT.

While the methods above all refer to the thermally ablative MR-HIFU applications, MR-HIFU can also be used to induce mild hyperthermia. The mechanisms of physiological changes upon mild hyperthermia are complex, making it difficult to predict tumor responses. MRI allows non-invasive mapping of parameters related to the physiology. Dynamic contrast enhanced (DCE)-MRI is a widely used method to make map parameters related to the permeability (K^{trans}, k_{ep}) and the blood volume fraction (v_p). With intravoxel incoherent motion (IVIM)-MRI, maps of the perfusion-related parameters f_p and D_p can be retrieved from diffusion-weighted MR data, where f_p is related to the blood volume fraction and D_p is the pseudo-diffusion. These parameters may provide insight in the effects of hyperthermia on the physiology. The advantage of IVIM-MRI is that no contrast agents are involved. In **CHAPTER 5**, we investigated the potential of DCE-MRI and IVIM-MRI to detect changes induced by hyperthermia using the MR-HIFU system.

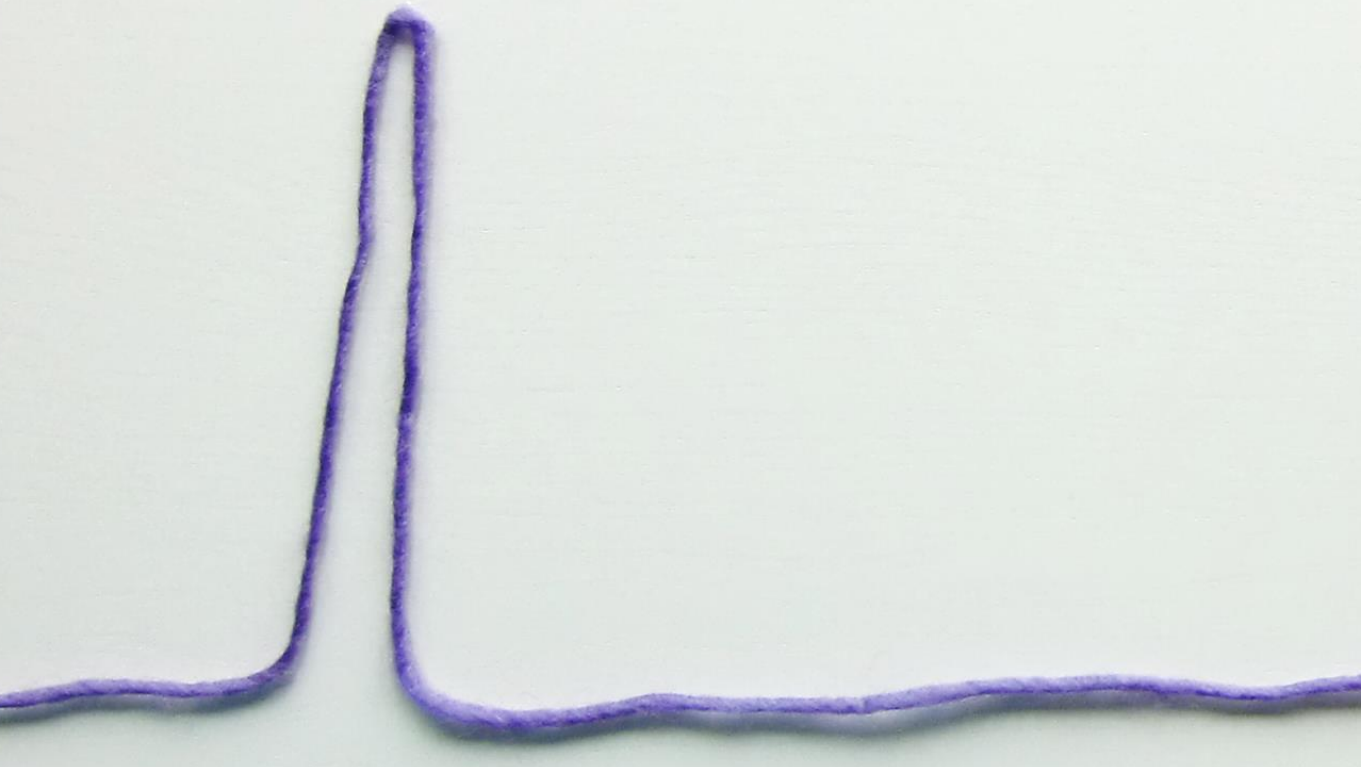

"Someone told me that each equation I included in the book would halve the sales"

– *Stephen Hawking*

Chapter 2

Quality of MR thermometry during palliative MR-HIFU treatment of bone metastases

Published in Journal of Therapeutic Ultrasound 2015, nr.5, vol.3 p.1-15

INTRODUCTION

Magnetic resonance-guided high-intensity focused ultrasound (MR-HIFU) is a modality for non-invasive thermal therapy. Focused ultrasound is used to locally heat the tissue, while the treatment can be monitored real-time using MR thermometry (MRT). MR-HIFU has been used for tumor ablation in the bone (53-56), liver (50,51,54,55,57-63), pancreas (51,55,64), kidney (61,65) and breast (54,63,66-69). Other clinical treatments that have been performed with MR-HIFU are the ablation of uterine fibroids (63,70-73) and of bone metastases for the purpose of pain palliation (63,74-78). In this study, we focused on the palliative treatment of bone metastases with MR-HIFU. The pain mechanism is thought to be closely related to the periosteal innervation (75,76), and therefore the aim is local periosteal denervation by heating the cortical bone. As cortical bone has a high acoustic absorption, the temperature in the bone will elevate more than that in the surrounding muscle tissue during exposure to HIFU (79). Another advantage of treating painful bone metastases with MR-HIFU is the time to response of typically a few days (75,76,78), compared to weeks when using external beam radiotherapy, the current standard of practice (80,81). Additionally, in contrast to external beam radiotherapy, MR-HIFU is not associated with radiation toxicity.

Unfortunately, the presence of the pain may complicate the treatment procedure. For example, the patient may not be able to lie still for a prolonged period of time or treatment-induced involuntary motion may occur if the treatment is not performed under general anesthesia. Patient motion may hamper the MR images that are used for treatment monitoring. Also, the image quality may be variable between specific cases for two reasons. First, bone metastases can occur at various locations. Second, there are three types of bone metastases: osteolytic, osteoblastic, and mixed. Osteolytic lesions are characterized by resorption of cortical bone, whereas osteoblastic lesions are characterized by formation of cortical bone. Mixed lesions exhibit both resorption and formation of cortical bone. Cortical bone has low water content (82) and a short T_2 (83) and will thus give very low MR signal. Therefore, the image quality may possibly be different between lesion types.

The most commonly used method for temperature mapping in MR-HIFU, used for treatment monitoring, is based on the temperature-dependent proton resonance frequency shift (PRFS) (25,26). Due to the lack of MR signal, PRFS-based MRT is unable to detect temperature changes in cortical bone. The bone marrow does give MR signal but has a high fat content. Since PRFS-based MRT only works in aqueous tissue, little to no temperature information can be retrieved from the bone marrow. The treatment monitoring during MR-HIFU of bone metastases is limited to the surrounding aqueous tissue. With PRFS-based MRT, temperature changes are calculated from phase differences obtained by phase image subtractions of gradient-echo scans (25). The method is therefore sensitive to non-temperature related spatiotemporal phase variations and subtraction errors, which will result in errors in the temperature images.
In this study, we evaluated the clinical performance of PRFS-based MRT used for monitoring of MR-HIFU ablation procedures of bone metastases that have been performed in our hospital. For this purpose, we assessed the general image quality by measuring the signal-to-noise ratio (SNR) and apparent temperature variations. Furthermore, potential artifacts in the temperature images were scored for their occurrence and hampering of treatment monitoring.

METHODS

ETHICS STATEMENT

Approval from the Institutional Review Board of the University Medical Center Utrecht (Utrecht, The Netherlands) was obtained for this study. All participants were counseled on the nature of the procedure, and all provided written informed consent for the treatment and use of their (anonymized) data.

PATIENT CHARACTERISTICS

Eleven patients, referred to our hospital for clinical palliative treatment of metastatic bone pain after exhaustion of the standard of care, were treated with a clinical MR-HIFU platform (Sonalleve, Philips Healthcare, Helsinki, Finland), integrated into a clinical 1.5-T MRI scanner (Achieva, Philips, Best,

The Netherlands). Two patients were retreated, resulting in 13 therapeutic sessions in total. Table 1 shows the patient characteristics. The treated lesions were located in the upper body (n = 4), the pelvis (n = 7), and in a lower extremity (n = 2). There were seven osteolytic lesions, five mixed lesions, and one osteoblastic lesion. Three types of intravenous procedural sedation and analgesia (PSA) were used: four patients received a combination of fentanyl (50–100 μg) and midazolam (2–5 mg) and will be referred to as PSA type A, four patients received propofol (induction 0.5–1 mg/kg, maintenance 5 mg/kg/h) combined with opioid analgesic at the discretion of the PSA specialist and will be referred to as PSA type B, and five patients received propofol (induction 0.5–1 mg/kg, maintenance 5 mg/kg/h) and esketamine as analgesic at the discretion of the PSA specialist and will be referred to as PSA type C. One patient treated in a lower extremity was retreated after 2 weeks at a different location and had metal internal fixation material in the target region. One patient treated in the pelvis was retreated after 4.5 months at the same location. A more detailed description of the treatments has been published elsewhere (48).

MRI SEQUENCES

The built-in radio frequency (RF) receiver coil inside the HIFU window was used together with a HIFU pelvis RF receiver coil positioned on top of the patient. Patients were positioned with the target lesion above the transducer window in the MR-HIFU tabletop. The first two treatments were performed on an earlier version of the clinical MR-HIFU system (Sonalleve, Release 2), where the HIFU window coil consisted of one element and the HIFU pelvis coil of two elements. The remaining treatments were performed on the most recent version of the clinical MR-HIFU system (Sonalleve, Release 3), where the HIFU window coil had three elements and the HIFU pelvis coil had two. In the treatment of the metastasis in the shoulder, the patient did not fit into the bore with the pelvis receiver coil positioned on top due to the patient positioning and the built-in body coil of the MR scanner was used instead (Table 1).

Table 1. Description of the patient group

Treatment number.	Sex	Age	Location	Lesion type	Receiver coil(s)	Number of datasets[g]
1[a,d]	M	58	Femur	Osteolytic	HIFU 3-elem	13
2[a,d]	M	58	Femur	Osteolytic	HIFU 3-elem	7
3[a]	F	55	Sacrum	Osteolytic	HIFU 5-elem	7
4[a]	F	56	Pubic bone	Mixed	HIFU 5-elem	11
5[b]	M	60	Pubic bone	Osteolytic	HIFU 5-elem	16
6[b,e]	F	64	Sacrum	Mixed	HIFU 5-elem	13
7[b]	F	53	Shoulder	Osteoblastic	MR Body coil	31
8[c]	M	86	Rib	Mixed	HIFU 5-elem	20
9[b,e,f]	F	64	Sacrum	Mixed	HIFU 5-elem	23
10[c,f]	M	55	Pubic bone	Osteolytic	HIFU 5-elem	27
11[c]	M	71	Pubic bone	Osteolytic	HIFU 5-elem	23
12[c]	M	65	Rib	Mixed	HIFU 5-elem	15
13[c]	M	64	Rib	Osteolytic	HIFU 5-elem	18
Total						224

[a] Performed under PSA type A (fentanyl and midazolam).

[b] Performed under PSA type B (propofol and opioid analgesic).

[c] Performed under PSA type C (propofol and esketamine).

[d] Same patient, retreated after 2 weeks, metal internal fixation material in target region.

[e] Same patient, retreated after 4.5 months.

[f] Higher resolution MRT scans used.

[g] For each sonication, one dataset was acquired, containing a dynamic series of multi-slice magnitude images, phase images, and calculated temperature maps.

Multi-planar reconstructed 3D T1-weighted spoiled gradient-echo scans were used for HIFU treatment planning with the following scan parameters: echo time = 4.6 ms, repetition time = 20 ms, flip angle = 30°, number of signal averages (NSA) = 2, number of slices = 100, field of view = 240 × 303 mm^2, acquisition matrix = 184 × 201, acquired voxel size = 1.3 × 1.5 × 2.6 mm^3. For HIFU treatment monitoring, a dynamic multi-slice, 2D spoiled gradient-echo echo-planar imaging (EPI) PRFS-based MRT sequence was used with water-selective binomial RF excitation pulses (1-2-1) with the following scan parameters: echo time = 19 ms, repetition time = 36 ms, flip

angle = 20°, NSA = 2, EPI factor = 11, number of slices = 4, field of view = 400 × 310 mm^2, acquisition matrix = 160 × 121, acquired voxel size = 2.5 × 2.6 × 7 mm^3, and dynamic scan duration = 3.7 s. During two treatments, higher resolution PRFS-based MRT scans were used with the same scan parameters, except for NSA = 1, field of view = 400 × 307 mm^2, acquisition matrix = 224 × 165, voxel size = 1.8 × 1.9 × 6.3 mm^3, and dynamic scan duration = 2.7 s. The positions of three imaging slices (coronal, sagittal, transverse) were fixed, with the centers of the imaging slices positioned at the center of the HIFU focus location, as shown in Figure 1. A fourth imaging slice (coronal) was positioned in a muscular area closest to the transducer, also known as the near-field area of the HIFU beam (Figure 1). Two dynamics of the dynamic MRT scan were acquired before sonication, and images were acquired continuously up to 2 min of the total acquisition time.

HIFU TREATMENT

The MR-HIFU treatments were performed by volumetric sonications, where ellipsoidal volumes were treated by electronic steering of the HIFU focus in concentric circular trajectories of increasing diameter (84). Treatment planning was done using the T1-weighted 3D scan. PRFS-based MRT images were used for temperature monitoring during the HIFU treatment. For each HIFU sonication, one dataset was obtained using an MRT pulse sequence, containing dynamic series of multi-slice magnitude images, phase images, and calculated temperature images. The temperatures were calculated by adding the patients' baseline body temperature (auricularly measured) measured before treatment to the temperature differences derived from the phase images of the dynamic MRT data. No field drift correction was performed for the MRT data, since little drift was expected during the acquisitions (duration up to 2 min). Each HIFU treatment was preceded by one or more test sonications at low power (median 30 W, range 20–50 W) and with short duration (median 16 s, range 16–20s). Therapeutic HIFU sonications were performed with variable power (median 95 W, range 10–160 W), variable duration (median 16 s, range 0.2–36 s), and variable cross-sectional diameter of the treatment volume (median 4 mm, range 2–12 mm) (84). The acoustic power levels of the HIFU sonications were determined by the treating physician and could be selected up to the maximum power level

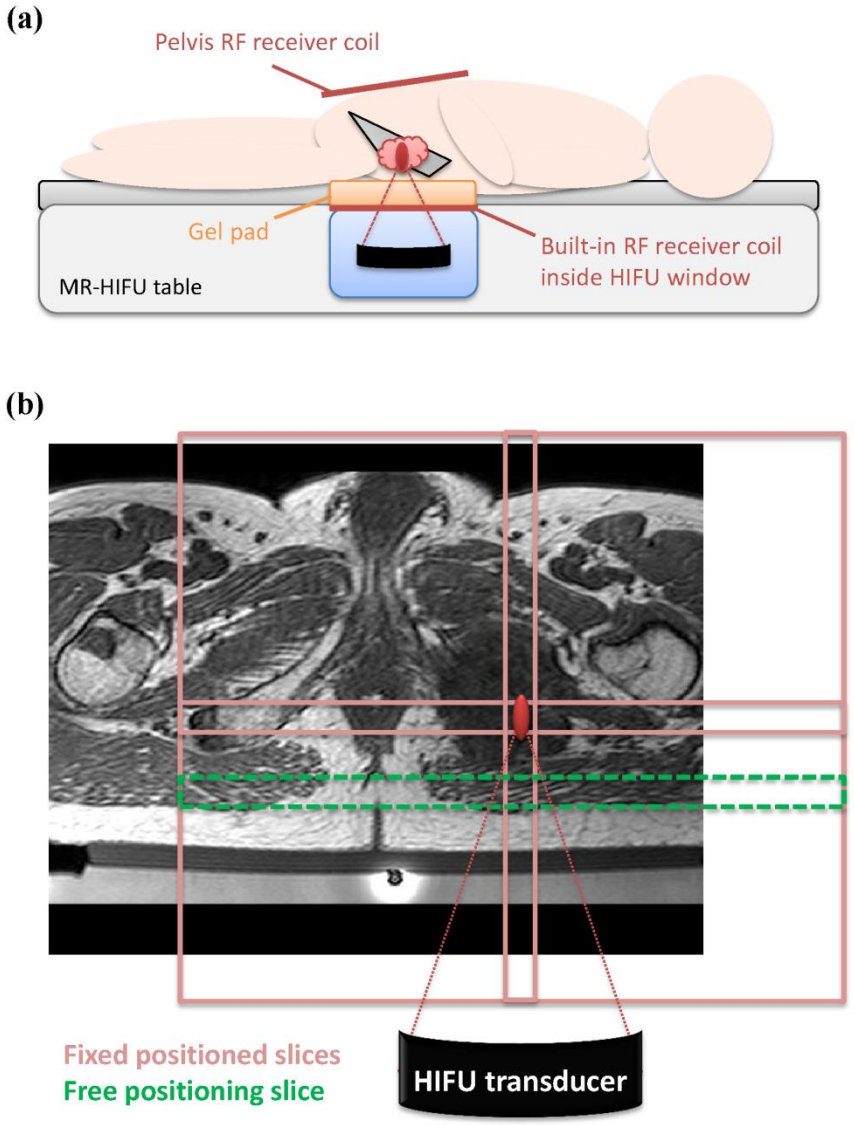

Figure 1. Slice positioning of the MRT scans. An example of an MR-HIFU setup for a treatment in the pelvis is shown in (a). An example of the MRT scan slice positioning is shown in (b), on a T1-weighted planning scan of an osteolytic lesion in the pubic bone (treatment 10). Three slices (light-red) were fixed with the centers to the location of the HIFU focus; one slice could be freely placed by the user and was placed in the near-field area of the HIFU beams (green, dashed).

allowed by the system, which ranged from 190 W for the smallest treatment volume to 80 W for the largest treatment volume. Data of both the test sonications and the therapeutic sonications were included. The total number of sonications within one treatment session ranged from 7 to 31, with a median of 16 (Table 1). A total number of 224 MRT datasets of 11 patients were used for the analysis, which included the datasets related to the test sonications.

DATA ANALYSIS: GENERAL IMAGE QUALITY

The general image quality was assessed by measuring the signal-to-noise ratio in the magnitude images acquired with the PRFS sequence and the apparent temperature variation in the calculated temperature images.

An important indicator for general image quality is the SNR of the magnitude images of the datasets. To avoid the influence of tissue structure in SNR measurements, we measured the SNR in single voxels over time. For each dataset, two voxels were selected for each imaging slice: one in the target lesion region and one in a muscle region near the lesion region. The voxels were selected in the temperature image, away from the heated area and away from any obvious local artifacts. When muscle contraction and/or body movement was observed visually in the magnitude image, the whole dataset was excluded from the analysis. When the lesion region and/or the muscle region were not visible in an imaging slice, the slice was excluded from the analysis. The temporal mean and temporal standard deviation of the magnitude signal intensities in the selected voxels over all dynamics were determined. Subsequently, the SNR of each voxel was calculated by dividing the mean by the standard deviation. Per dataset, the SNR values of the voxels in the target lesion were averaged and the SNR values of the voxels in the surrounding muscle were averaged. Finally, the average SNR over all datasets in the target lesion and surrounding muscle was calculated per treatment.

As another measure of the general image quality, we measured the apparent temperature variation that was not influenced by heating or obvious artifacts. For each dataset, one voxel was selected for each slice in the temperature image in a muscle region, away from the heated area and away from any obvious local MRT artifact. The datasets that were excluded

from the SNR analysis because muscle contraction and/or body movement were observed visually were also excluded from this analysis. When the muscle region was not visible in an imaging slice, the slice was excluded from the analysis. The apparent temperature variation was defined as the temporal standard deviation of the measured temperatures with PRFS-based MRT in the selected voxel over all dynamics. Per dataset, the apparent temperature variation values of the voxels were averaged. Finally, the average apparent temperature variation was calculated per treatment.

Qualitative comparisons were done between different lesion types (osteolytic, mixed, and osteoblastic) and locations (upper body, pelvis, and lower extremity). To make the comparisons as fair as possible, datasets were excluded of the treatments where metal fixation material was present and higher resolution scans were used.

DATA ANALYSIS: ARTIFACTS

As PRFS-based temperature images are reconstructed from subtracted phase images (25), non-temperature related phase changes will result in errors in the temperature images. From here on, these errors will be referred to as MRT artifacts. The dynamic multi-slice temperature images were scored by one observer (ML) for the occurrence of MRT artifacts and hampering of the treatment monitoring by MRT artifacts caused by the following sources: time-varying field inhomogeneities, arterial ghosting, and patient motion.

Field inhomogeneities are caused by the susceptibility distribution. Static field inhomogeneities will not lead to errors in temperature images, as they are canceled out by the subtraction of subsequent phase images. However, temporal changes of the susceptibility distribution will cause time-varying field inhomogeneities, leading to local non-temperature-related phase changes and resulting in MRT artifacts. Changing volumes of air is one of the most prominent sources of this type of artifact, as the susceptibility of air (χ = 0.36 ppm) differs considerably from that of human tissues (χ = −11.0 to −7.0 ppm) (85). As the air volume in the lungs varies over the respiratory cycle, respiration can cause periodical phase variations in regions near the lungs (85). Two categories of time-varying field inhomogeneity artifacts were distinguished: respiratory and non-respiratory. The respiratory MRT artifacts were classified as periodical temperature variations in the whole temperature

map; the non-respiratory MRT artifacts as local highly variable temperatures near interfaces (e.g., bowel, rectum) and can be verified by looking at the phase images.

Arterial ghosting is caused by pulsatile blood flow, which leads to reconstruction of the MR signal of the blood at a different position than where it originated from (86). In the phase image, this ghosting will appear as vessel-shaped areas with variable phase values, displacing over the image in the phase-encoding direction. The resulting MRT artifacts were classified as vessel-shaped objects with variable observed temperatures, displacing over the image in the phase-encoding direction.

Patient motion will lead to misregistration between subtracted phase images. Artifacts due to patient motion were scored as either due to muscle contraction or due to gross body movement. When both muscle contraction and gross body movement were observed, the artifact was scored as being caused by gross body movement. Classification was done by the observation of muscle contraction and gross body movement in the magnitude image; the resulting MRT artifacts were large observed temperature changes at the location and time of the motion. With gross body movement the MRT artifact typically affected the whole temperature image. With muscle contraction, the MRT artifact occurred typically locally at the location of the muscle. However, due to the displacement of the tissue, non-respiratory time-varying field inhomogeneity artifacts may increase in size and severity. As the occurrence of patient motion may depend on different factors, distinction was made between lesion type, location, and PSA type.

An MRT artifact was scored as "occurred" when it was observed in at least one of the temperature imaging slices. The dataset was also scored as "hampered" if the visualization of the heat built-up due to the HIFU treatment and the following cooldown was distorted due to the MRT artifact. This could be observed as either temperature errors in and around the focus or the inability to detect (expected) HIFU heating: both may hamper the treatment monitoring. How often a type of MRT artifact occurred and/or hampered the treatment monitoring was determined per treatment and expressed as a percentage of the number of MRT datasets of the treatment, which will be referred to as the "occurrence rate" and the "hampering rate" from here on. Also, the total occurrence and total hampering of each artifact

were determined and expressed as a percentage of all 224 MRT datasets, which will be referred to as the "total occurrence rate" and "total hampering rate".

RESULTS

GENERAL IMAGE QUALITY

Figure 2a shows the average SNR per treatment, distinction was made between the lesion types. The average SNR in the lesions ranged from 2.3 to 30 and in surrounding muscles from 8.7 to 39. Figure 2b shows the average SNR per lesion type and Figure 2c the average per location, where treatments 1, 2, 9, and 10 were excluded because of either the presence of a metal internal fixation material or the use of higher resolution scans. In the comparison between lesion types (Figure 2b), the highest average SNR was found in and around osteolytic lesions (lesions: 21 ± 8, surrounding muscles: 27 ± 6, n = 4). The average SNR in mixed lesions was 11 ± 8 and 15 ± 5 in surrounding muscles (n = 4); the average SNR in osteoblastic lesions was 5 and 18 in surrounding muscles (n = 1). In the comparison between locations (Figure 2c), the average SNR was higher in the pelvis (lesions: 19 ± 8, surrounding muscles: 24 ± 9, n = 5), as compared to the upper body (lesions: 9 ± 7, surrounding muscles: 16 ± 5, n = 4). Because of the exclusion of the treatments with metal fixation material present, there were no datasets left in the lower extremity region.

Figure 3a shows the average apparent temperature variation per treatment, distinction was made between the locations. The apparent temperature variation ranged from 0.5°C to 3°C. Treatments 4 and 9 are the only two with a variation larger than 2°C and were both mixed lesions in the pelvis. Similar to the SNR analysis, treatments 1, 2, 9, and 10 were excluded in the comparisons between lesion types and locations. In the comparison between lesion types (Figure 3b), the apparent temperature variation in the datasets of the osteolytic lesion (1.2 ± 0.5°C, n = 4) was found to be lower than in the datasets of the mixed (1.8°C ± 0.8°C, n = 4) and osteoblastic lesions (1.7°C, n = 1).

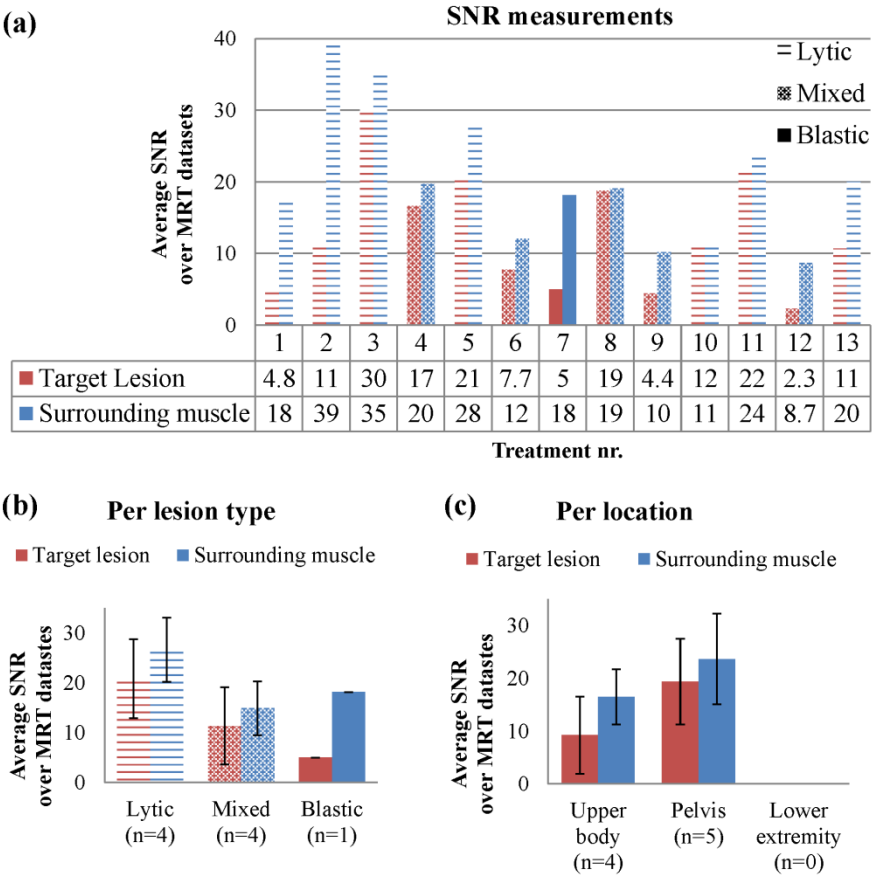

Figure 2 The SNR measured in the magnitude images. The average SNR is shown per treatment (a), per lesion type (b), and per location (c). The rows with numbers below the graph in (a) show from top to bottom: treatment numbers, average SNR values in the target lesion, and average SNR values in the surrounding muscle. Treatment numbers 1, 2, 9, and 10 were excluded in (b) and (c). The error bars in (b) and (c) represent the standard deviations.

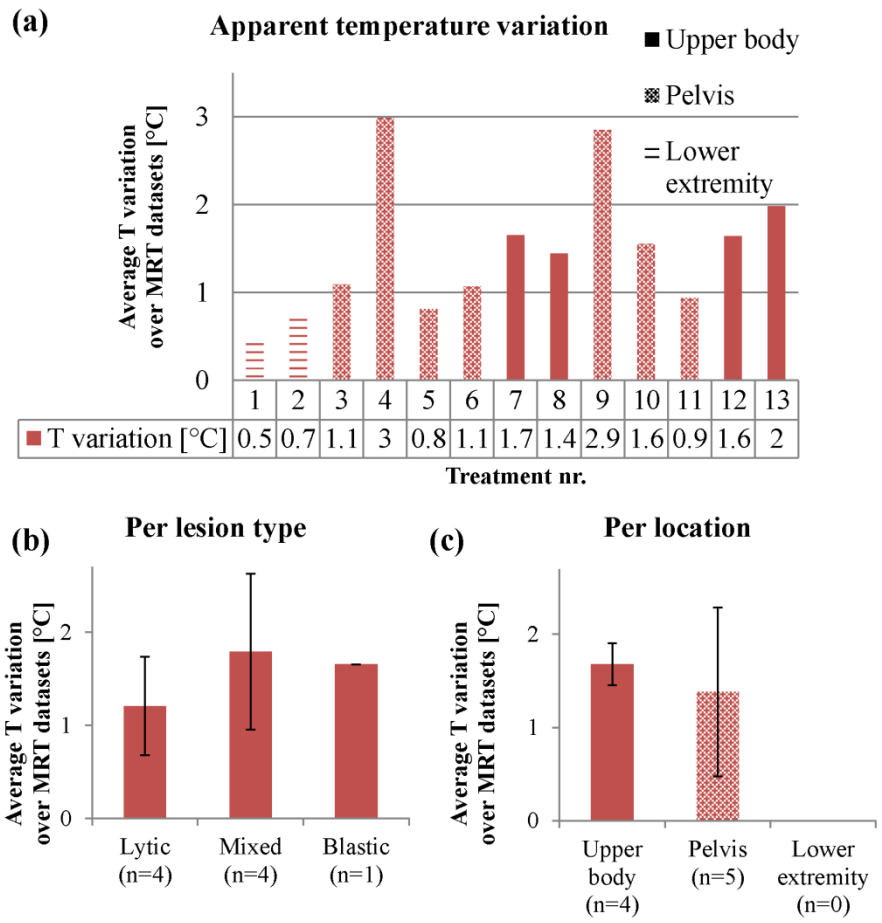

Figure 3 The apparent temperature variation measured in the temperature images. The average temperature variation is shown per treatment (a), per lesion type (b), and per location (c). The rows with numbers below the graph in (a) show the treatment numbers (top) and average apparent temperature variation values (bottom). Treatment numbers 1, 2, 9, and 10 were excluded in (b) and (c). The error bars in (b) and (c) represent the standard deviations.

In the comparison between locations (Figure 3c), the apparent temperature variation was found to be higher in the upper body (1.7°C ± 0.2°C, n = 4) compared to the pelvis (1.4°C ± 0.9°C, n = 5). Because of the exclusion of the treatments with metal fixation material present, there were no datasets left in the lower extremity region.

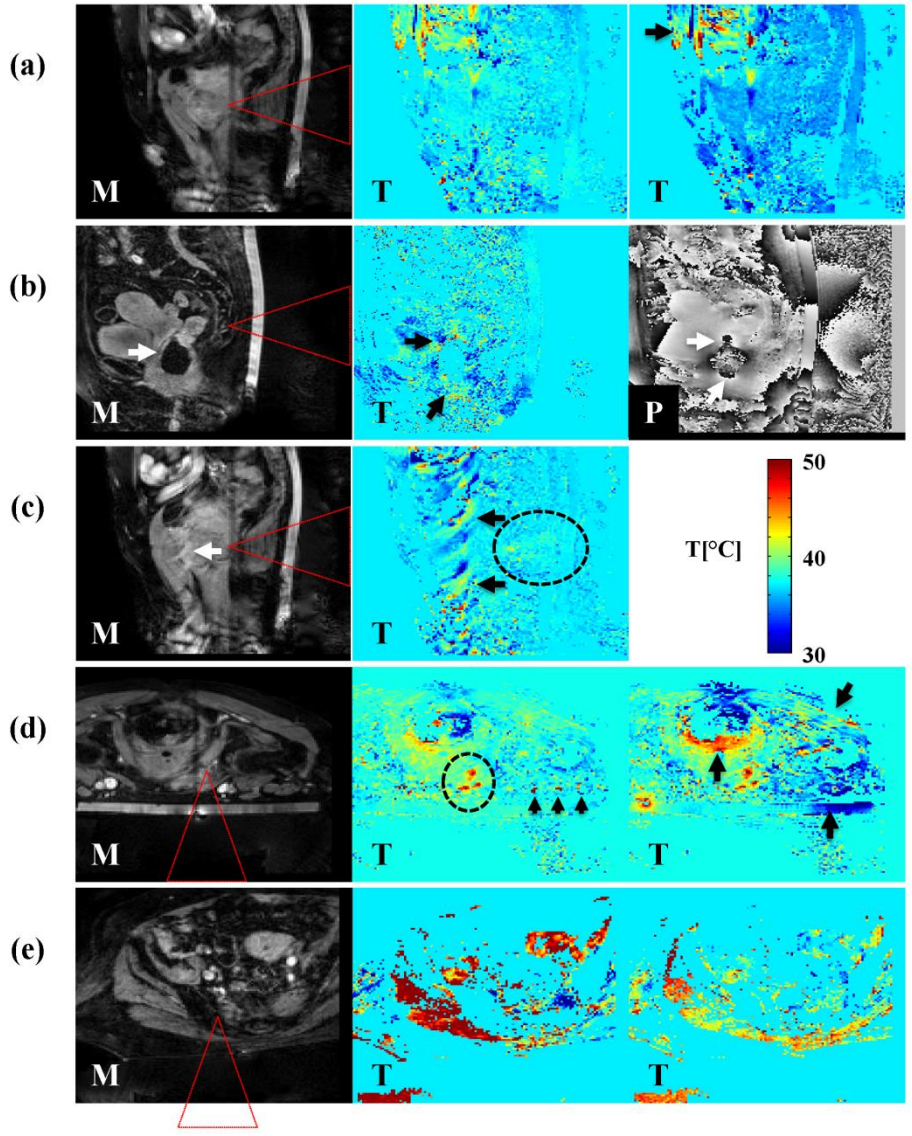

ARTIFACTS

Typical examples of the MRT artifacts that were scored are shown in Figure 4, together with the corresponding magnitude images for the visualization of the anatomy: Figure 4a shows a respiratory time-varying field inhomogeneity MRT artifact; Figure 4b shows a non-respiratory time-varying field inhomogeneity MRT artifact, of which the origin of the artifact could be verified in the phase image; Figure 4c shows a typical arterial ghosting MRT artifact; Figure 4d shows patient motion MRT artifacts due to muscle contraction; and Figure 4e shows patient motion MRT artifacts due to gross body movement.

Figure 4 (on the left page). Typical examples of MRT artifacts. The arrows point out MRT artifacts in magnitude (M) images, temperature (T) images, and phase (P) images. The red dashed triangles indicate the expected HIFU cone. **(a)** A respiratory time-varying field inhomogeneity MRT artifact (treatment 5, sagittal slice, supine position, osteolytic lesion in the pubic bone). The artifact causes periodical "blinking" of the temperature map. The arrow points out an additional non-respiratory time-varying field inhomogeneity MRT artifact. **(b)** A non-respiratory time-varying field inhomogeneity MRT artifact (treatment 9, sagittal slice, supine position, mixed lesion in the sacrum). The artifact is caused by an air cavity, which can also be seen in the magnitude image. The local changes in the phase image around the location of the air cavity verify that the air cavity is the source. **(c)** An arterial ghosting MRT artifact (treatment 5, sagittal slice, supine position, osteolytic lesion in the pubic bone) caused by the femoral artery, which can also be seen in the magnitude image. **(d)** Muscle contraction MRT artifacts (treatment 5, transverse slice, prone position, mixed lesion in the pubic bone). The artifacts occur not only at the location of the contracting muscles (two arrows at the most right) but also around the rectum. The three arrowheads point out additional arterial ghosting MRT artifacts. **(e)** A gross body movement MRT artifact (treatment 6, transverse slice, supine position, mixed lesion in the sacrum, affects the whole temperature image drastically. In the dashed ellipses in **(c)** and **(d)**, heating due to the HIFU treatment can be observed. The image shown in **(b)** was acquired before HIFU sonication started; thus, no HIFU heating was expected to be observed. In **(a)** and **(e)**, the visualization of potential HIFU heating was hampered due to the presence of the artifact.

Figure 5 shows the total occurrence of and hampering of the treatment monitoring by MRT artifacts in percentage of all datasets of all treatments, per source. It can be seen that when artifacts occurred due to respiratory time-varying field inhomogeneities or patient motion, the artifacts hampered the visualization of the heat built-up in most cases. MRT artifacts due to non-respiratory time-varying field inhomogeneities and arterial ghosting were observed in almost all datasets, but only few have hampered the treatment monitoring.

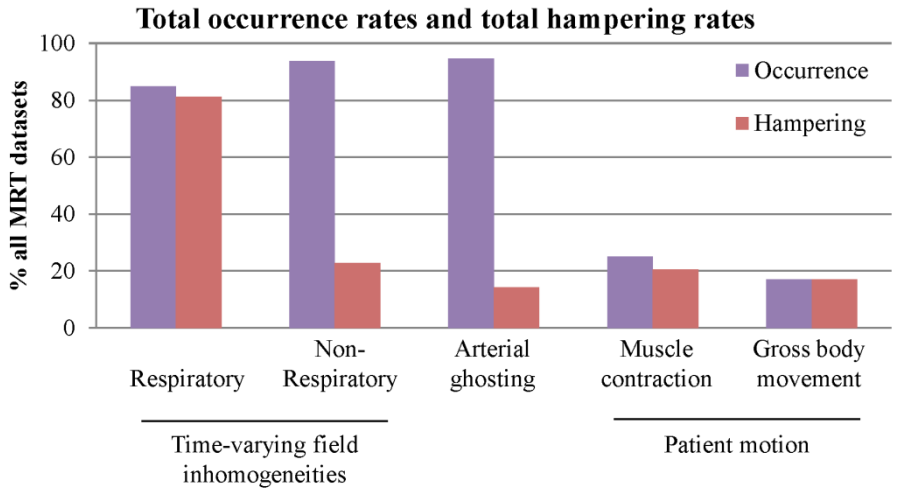

Figure 5. Total occurrence rates and total hampering rates of MRT artifacts. The occurrence rates and hampering rates are shown per source, in % of all MRT datasets.

The occurrence rates and hampering rates of the MRT artifacts per treatment are shown in Table 2 as percentage of the total number of datasets. The total occurrence rate of respiratory time-varying field inhomogeneity MRT artifact was 85%, and the total hampering rate was 81%. This artifact did not occur in the two treatments in the lower extremity, while in 8 treatments, the occurrence rate was 100%. The total occurrence rate of non-respiratory time-varying field inhomogeneity MRT artifact was 94%, and the total hampering rate was 23%. This artifact did not occur at all in one treatment but occurred 97% in one treatment and 100% in the remaining treatments. The total

Table 2. Occurrence rates and *hampering rates* of the MRT artifacts in % of the total number of datasets per treatment

Treatment number	Location	Lesion type	Time-varying field inhomogeneities				Arterial ghosting		Patient motion			
			Respiratory		Non-Respiratory				Muscle contraction		Body movement	
1[a,d]	Femur	Osteolytic	0	*0*	0	*0*	100	*0*	15	*0*	0	*0*
2[a,d]	Femur	Osteolytic	0	*0*	100	*0*	100	*0*	14	*0*	0	*0*
3[a]	Sacrum	Osteolytic	100	*100*	100	*0*	0	*0*	43	*29*	0	*0*
4[a]	Pubic bone	Mixed	82	*64*	100	*82*	100	*82*	91	*73*	0	*0*
5[b]	Pubic bone	Osteolytic	69	*38*	100	*0*	100	*0*	6.3	*6.3*	13	*13*
6[b,e]	Sacrum	Mixed	100	*100*	100	*0*	100	*0*	38	*31*	54	*54*
7[b]	Shoulder	Osteoblastic	100	*100*	97	*9.7*	100	*3.2*	39	*35*	35	*35*
8[c]	Rib	Mixed	100	*100*	100	*0*	100	*20*	10	*10*	0	*0*
9[b,e,f]	Sacrum	Mixed	100	*100*	100	*0*	83	*0*	17	*17*	39	*39*
10[c,f]	Pubic bone	Osteolytic	100	*100*	100	*33*	100	*0*	3.7	*3.7*	3.7	*3.7*
11[c]	Pubic bone	Osteolytic	70	*65*	100	*22*	96	*35*	22	*17*	13	*13*
12[c]	Rib	Mixed	100	*100*	100	*100*	100	*67*	53	*47*	33	*33*
13[c]	Rib	Osteolytic	100	*100*	100	*56*	100	*0*	11	*11*	0	*0*
Total			85	*81*	94	*23*	95	*14*	25	*21*	17	*17*

Note: The occurrence rates are shown in normal font, the hampering rates in italic font.

[a] Performed under PSA type A (fentanyl and midazolam).

[b] Performed under PSA type B (propofol and opioid analgesic).

[c] Performed under PSA type C (propofol and esketamine).

[d] Same patient, retreated after 2 weeks, metal internal fixation material in target region.

[e] Same patient, retreated after 4.5 months.

[f] Higher resolution MRT scans used.

occurrence rate of arterial ghosting MRT artifacts was 95%, and the total hampering rate was 14%. This artifact did not occur in one treatment but occurred more than 80% in the remaining treatments, of which in 10 treatments the occurrence rate was 100%. The total occurrence rate of muscle contraction MRT artifact was 25%, and the total hampering rate was 21%. This artifact occurred in all treatments but less than 20% in 7 treatments. The total occurrence rate of gross body movement MRT artifact was 17%, and the total hampering occurrence rate was 17%.

The variation of patient motion occurrence rate between treatments is visualized in Figure 6a, where distinction was made between PSA types. In some treatments, almost no patient motion occurred, while in some treatments, patient motion was dominantly present. Figure 6b shows the comparison between lesion types, and the lowest rates were found in osteolytic lesion types. The total patient motion occurrence rate was 20% (16% muscle contraction, 4% gross body movement, n = 7) in the osteolytic lesion datasets as compared to the 67% (42% muscle contraction, 25% gross body movement, n = 5) in the mixed lesion datasets and 74% (39% muscle contraction, 35% gross body movement, n = 1) in the osteoblastic lesions datasets. Figure 6c shows the comparison between locations: the total patient motion occurrence rate was similar for the upper body (45% in total: 28% muscle contraction, 17% gross body movement, n = 4) and the pelvis (49% in total: 32% muscle contraction, 17% gross body movement, n = 7) and lowest in the lower extremity (15% in total: 15% muscle contraction, 0% gross body movement, n = 2). The total patient motion occurrence rates are compared between PSA types in Figure 6d. For PSA type A, the total patient motion occurrence rate was 41% (41% muscle contraction, 0% gross body movement, n = 4); please note that this group includes the two lower extremity treatments. The total patient motion occurrence rate was higher for PSA type B (60% in total: 25% muscle contraction, 35% gross body movement, n = 4) as compared to PSA type C (30% in total: 20% muscle contraction, 10% gross body movement, n = 5).

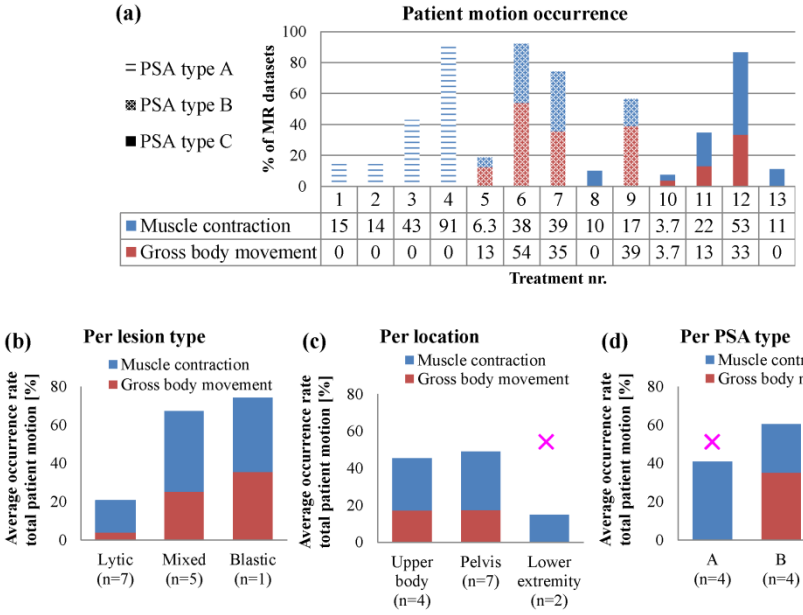

Figure 6. Overview of the patient motion MRT artifacts occurrence rates. The patient motion occurrence rates are shown in % of all MRT datasets. (a) The patient motion occurrence rates per treatment. The average occurrence rates are shown per lesion type (b), per location (c), and per PSA type (d). PSA type A: fentanyl and midazolam, PSA type B: propofol and opioid analgesic, PSA type C: propofol and esketamine. The rows with numbers below the graph in (a) show from top to bottom: treatment numbers, patient motion occurrence rates in % due to muscle contraction, and patient motion occurrence rates in % due to gross body movement. Please note that the lower extremity treatments were only performed using sedation A (indicated with the pink ×).

DISCUSSION

The quality of the MR thermometry used for the monitoring of 13 palliative treatment patients with painful bone metastases with MR-HIFU was assessed in terms of general image quality and artifacts.

GENERAL IMAGE QUALITY

The comparison between lesion types shows descending average SNR in the target lesion with increasing amount of cortical bone (osteolytic: 21, mixed: 11, osteoblastic: 5). The average SNR in the surrounding muscle was highest around osteolytic lesions (27) and was similar for the mixed and osteoblastic type (15 compared to 18). The apparent temperature variation was high in the mixed lesions (1.8°C) and osteoblastic lesions (1.7°C) and low in the osteolytic lesions (1.2°C). The descending SNR in the lesions could be explained by the difference in the amount of cortical bone present. Cortical bone has a very short T_2^* (83) and will thus give very little signal in PRFS-based MRT sequences, which need a relatively long echo time. It was therefore expected that osteoblastic lesions will have a lower SNR compared to osteolytic lesions. However, no differences in SNR in the surrounding muscle would be expected between lesion types. There are several possible explanations for the observed differences in SNR in the surrounding muscle. First, in two treatments of mixed lesions, the apparent temperature variations were larger than 2°C, implying a relatively large influence of respiration effects in the measured SNR values. Second, only one osteoblastic lesion was treated in this study. For this treatment, the MR body coil was used for the image acquisition, while the dedicated HIFU coil combination was used in all other treatments.

The comparison between locations showed lower SNR in the upper body (9 in lesion, 16 in surrounding muscle) than in the pelvis (19 in lesion, 24 in surrounding muscle). The smallest apparent temperature variation was found in the lower extremity (0.6°C), where no respiratory time-varying field inhomogeneity artifacts were observed. The apparent temperature variation was higher in the upper body (1.7°C) as compared to in the pelvis (1.4°C). The standard deviation of the apparent temperature variation in the pelvis was relatively large (0.9°C), which can be explained by the fact that this

group contained the two outliers with an apparent temperature variation larger than 2°C (treatment numbers 4 and 9). Please note that these outliers were both mixed lesion in the pelvis. Both the SNR and apparent temperature variation measurements indicate an increasing image quality with increasing distance to the upper body. This has also been observed previously by Peters, et al. (87), in their measurements of respiratory field changes in the breast of volunteers using a dedicated scan sequence to investigate the effects of respiration. They reported maximum field fluctuations values over time during regular respiration of 0.13 ppm, corresponding to 13°C, which is much larger than the observed temperature variations in this study. The discrepancy can be explained by two differences between the study by Peters et al. and our study. First, we measured respiration-induced fluctuations over time, while Peters et al. measured fluctuation values that were spatially averaged over a region of interest covering both breasts; average fluctuations over time were not reported. Second, the dynamic scan duration in the study of Peters et al. was 0.64 s, while it was 3.7 s in our study. Also, the MRT sequence in our study was a segmented EPI, with 11 segments per *k*-space. In the presence of respiration of which the period is in the same order as the dynamic scan duration, the different *k*-space segments may have been affected differently by the field offsets induced by the respiration. Therefore, respiration-induced fluctuations may appear differently than in a non-segmented EPI scan, such as spoiled gradient-echo scan (87).

Voxels were selected carefully for the assessment of the general image quality, such that influences of HIFU heating, patient motion, and obvious local artifacts in the MR images were avoided. No corrections were made for the respiration. Since variations due to respiration were observed in the majority of the datasets (85%), exclusion of affected datasets would result in too few datasets for analysis. Frequency analysis could be an alternative way to filter out respiration effects. However, the datasets contained few samples (16 time points on average) and had a low sampling frequency (once per 3.7 s, corresponding to about 0.3 Hz). The respiration rate was not measured during the treatment. The range of respiration rates in adults is 12 to 18 per minute (88), corresponding to 0.2-0.3 Hz, which cannot be resolved with the current sampling. Also, we observed that the breathing pattern was typically

irregular in both amplitude and frequency during the treatment, making accurate frequency analyses even more difficult. For these reasons, filtering of the respiration effects by frequency analysis was deemed not feasible in this study. Therefore, the SNR and apparent temperature variation measurements in this study represent the image quality (degradation) due to noise and variations induced by the respiration. Although the respiration effects could not be filtered or corrected, these measurements can still be used as a rough estimate of the image quality for the purpose of treatment monitoring. Because the SNR was measured in the magnitude images, it predominantly represents the image quality in terms of noise. Similarly, because the apparent temperature variations were measured in the PRFS-based temperature images, they predominantly represent the image degradation due to respiration.

Recently, Deckers, et al. (89) reported the effects of sedation on the respiration and the thermometry quality in four patients for MR-HIFU ablation of breast cancer. They observed that the use of propofol and esketamine (PSA type C in this study) resulted in more shallow and regular breathing patterns of the patients during treatment as compared to the use of propofol and opioid analgesic (PSA type B in this study). In this study, no reduction of the apparent temperature variation was measured with the use of propofol and esketamine (Figure 7). As the apparent temperature variation predominantly represented the image degradation due to respiration, this implies no regularization of the breathing pattern with the use of propofol and esketamine. The study reported by Deckers, et al. (89) was performed on patients with breast cancer; the patients of this study were patients with bone metastases in an advanced stage of their disease. The purpose of the MR-HIFU treatment of these patients was to palliate the pain that could not be reduced sufficiently by the standard of care, often including opioid analgesics. As a consequence of their history of opioid usage, the patients included in our study may have reacted differently to the same type of PSA than patients with breast cancer who were typically opioid-naive.

The observations made in this study suggest that in MR-HIFU treatments of patients with bone metastases, the general MRT image quality is related to the lesion type and location. However, no statistical analyses were performed due to the small sample size and heterogeneous patient

population, which limit the validity of the outcome. To establish and further quantify this association, a larger dataset is needed.

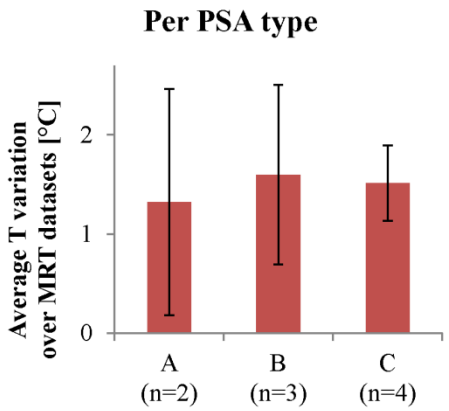

Figure 7. Apparent temperature variation, averaged per PSA type. PSA type A: fentanyl and midazolam, PSA type B: propofol and opioid analgesic, PSA type C: propofol and esketamine. Treatment numbers 1 and 2 were excluded due to the presence of metal internal fixation material, and treatment numbers 9 and 10 were excluded due to the use of higher resolution scans.

ARTIFACTS

The most dominant MRT artifact was the respiratory time-varying field inhomogeneity MRT artifact (85% occurrence rate, 81% hampering rate). Although the non-respiratory time-varying field inhomogeneity artifacts and arterial ghosting occurred more often (94% and 95%), these artifacts hampered the treatment monitoring only in a small number of cases (23% and 14%). This difference can be explained by the fact that non-respiratory time-varying field inhomogeneities and arterial ghosting induce local MRT artifacts, whereas respiratory time-varying field inhomogeneities induce large spatial field gradients, and thereby, temperature offsets potentially in the whole field of view. The total occurrence of and hampering of the treatment monitoring by patient motion MRT artifacts, both muscle contraction and gross body movement, was low compared to the other artifacts.

The patient motion occurrence rates of the individual treatments show that there is a large variation between treatments. Interestingly, patient

motion occurred less in the datasets of the osteolytic lesions (14%) as compared to the mixed (61%) and osteoblastic lesions (70%). This observation suggests a relation between the presence of cortical bone in the lesion and patient motion. If the presence of bone implies the presence of periosteal nerves, this relation could possibly be explained by (involuntary) motion induced by periosteal nerve stimulation. In the comparison between locations, the average occurrence rate was lowest in the lower extremity, which is likely easier to control in terms of motion as compared to the pelvis and the upper body. In the comparison between PSA types, type A contained the two treatments in the lower extremity and may therefore be biased. The average occurrence rate was lower for PSA type C (30%) as compared to PSA type B (60%). This observation is in the same line as the observed regularization of the breathing pattern by Deckers, et al. (89), with the use of propofol and esketamine (PSA type C) as compared to propofol and opioid analgesic (PSA type B). However, as the sample size is small and the patient population is heterogeneous, more data is required to further investigate the potential relations found in this study.

FUTURE PROSPECTS

Although the analyzed data was of a small patient group, a large number of datasets was analyzed and we have made observations possibly allowing improvements for future MR-HIFU treatments of bone metastases.

Measurement of the SNR and the apparent temperature variation could serve as a rough estimator of the general image quality. Higher SNR was observed in osteolytic lesions, and the apparent temperature variations were observed to decrease as the distance to the lungs increased. The observations made in this study should be kept in mind, as they could indicate a potential dependency of the expected image quality on the lesion types and/or location.

The MRT artifact analysis revealed the highest occurrence rate for non-respiratory time-varying field inhomogeneity artifacts and arterial ghosting. Although the direct hampering of the heat built-up visualization was minimal, the presence of the artifacts may cause problems when the temperature maps are automatically post-processed before they are shown to the clinician. For example, a post-processing algorithm could be used to

classify observed temperature changes as apparent or true temperature changes and mask out apparent temperature changes. However, if the classification is based on observed temperature changes in a region where local MRT artifacts occur, these local MRT artifacts will indirectly hamper the treatment monitoring. Placement of a saturation slab can be considered to remove local artifacts. In case arterial ghosts do hamper the visualization of the heat built-up, changing the phase encoding direction could be considered so that the ghosting direction will be changed as well. In all cases, the adjustments should be made case-specific and care should be taken when interpreting the MR temperature images. Recently, an advanced spatiotemporal filtering post-processing method was proposed to remove MRT artifacts due to air bubbles in the rectum and was tested retrospectively (90). This technique has potential to improve the MRT quality in real time for treatment monitoring but requires further investigation before it can be applied in clinical practice.

The occurrence rate of patient motion was variable, and two important observations were made: the occurrence rate was lower in the treatments of osteolytic lesions and the occurrence rate was lower with the use of PSA type C (propofol and esketamine). Although the number of treatments included in this study was small, these observations should be kept in mind for future MR-HIFU treatments of bone metastases.

Respiratory time-varying field inhomogeneity artifacts were found to occur and hamper the treatment monitoring in the majority of the cases. This "blinking artifact" makes it challenging to determine the actual temperature increase due to HIFU heating. Nevertheless, the MRT used in this study allows localization of the heat built-up, which is the most important aspect of the treatment monitoring of the pain palliative treatment of bone metastases. However, for the other (potential) MR-HIFU applications in bone (metastases), i.e., tumor control by ablation (53-56) and local drug delivery (91,92), accurate temperature measurements are necessary. For total tumor ablation, a lethal thermal dose should be reached in the whole tumor without damaging the surrounding healthy tissue and thus reliable temperature measurements are required. In the pre-clinical local drug delivery study by Staruch, et al. (91) it was shown that doxorubicin encapsulated in temperature-sensitive liposomes could be released *in vivo* in

femurs of rabbits by MR-HIFU-induced mild hyperthermia. The release temperature window is typically between 41°C and 43°C and this mild hyperthermia was achieved and controlled by means of a feedback algorithm, using the real-time MR temperature information (5). However, temperature errors due to the presence of MRT artifacts may affect the feedback algorithm and impede the temperature control. If tumor ablation and local drug delivery are to be applied in the patient population reported in this study, advanced methods to compensate for the respiration (93,94) and more sophisticated MR thermometry methods will be necessary, as these applications require more than solely localization of the heat deposition (95-97).

CONCLUSION

The image quality of PRFS-based temperature images used for monitoring MR-HIFU palliative treatments of bone metastases was assessed. The general image quality was variable and was observed to be better in osteolytic lesions as compared to other lesion types and worse in the upper body as compared to the pelvis, in terms of SNR and apparent temperature variation. However, more treatment data is required to verify these potential relations. The MRT images were scored for the occurrence of MRT artifacts and hampering of treatment monitoring by MRT artifacts. Respiratory time-varying field inhomogeneity MRT artifacts were the most dominant and were also observed in the pelvic area, which is rather distal from the upper body. The MRT artifacts with the highest occurrence rate were those induced by non-respiratory time-varying field inhomogeneities and arterial ghosting. But because these were local artifacts, the hampering rate was low. The occurrence rate of patient motion was variable between treatments and seemed to be related to the presence of cortical bone in the lesion. Lower occurrence rates were observed with the use of propofol and esketamine as compared to the other PSA types. Clinicians should be aware of these artifacts and interpret the MRT images carefully when used for monitoring MR-HIFU treatments in bone.

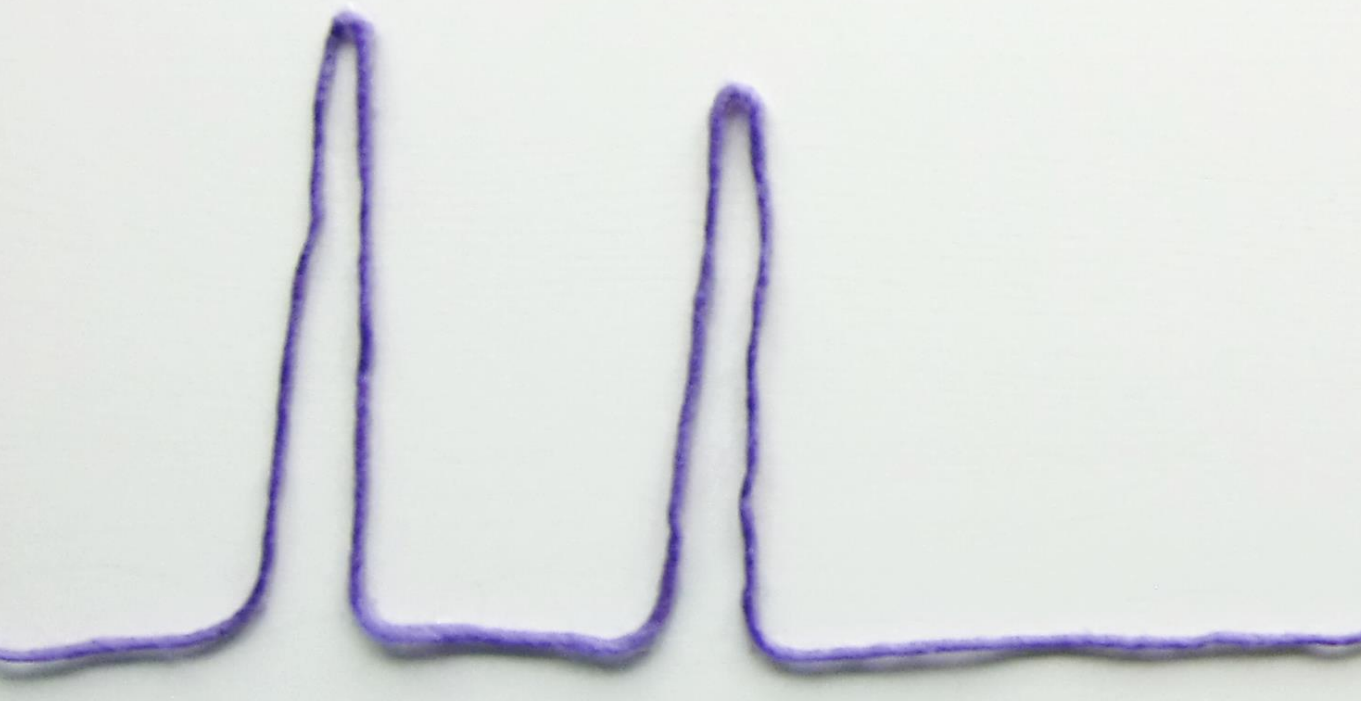

"No problem can be solved

from the same level of consciousness that created it"

– Albert Einstein

Chapter 3

Multi-gradient echo MR thermometry for monitoring of the near-field area during MR-HIFU heating

Published in Physics in Medicine & Biology 2015, vol. 60, p. 7729-7746

INTRODUCTION

Magnetic resonance-guided high intensity focused ultrasound (MR-HIFU) is a non-invasive thermal therapy modality where MR thermometry (MRT) allows temperature monitoring in the targeted region during sonications (35). An emerging application of MR-HIFU is tumor ablation in abdominal organs using extracorporeal transducers, where the non-invasive nature and the real-time image guidance provide the opportunity to preserve healthy tissue outside the target area. Clinical ultrasound-guided HIFU tumor ablation in abdominal organs was reported in liver (49,50,57-61), pancreas (51,55,64) and kidney (61,65). On MR-guided HIFU, pre-clinical tumor ablation studies have been performed in kidney and liver (40,52,98,99) and two clinical case-studies were reported in primary tumors in liver and in pancreas (100,101).

Abdominal organs are generally well-perfused, so thermal build-up is less effective than for example muscle tissue due to the heat-sink effect (102,103). Relatively high acoustic power levels (100W-450W) are needed to achieve the targeted temperatures (40,49-52). Also, while the HIFU focus volume is typically 7 to 17 mm^3 (59,84), typical target volumes are in the order of a few to tens of cm^3 (49,50,55,57-59,61,64,65) and consecutive sonications may be required to cover the target volume. Such consecutive sonications at high powers may induce undesired cumulative thermal build-up in tissue traversed by the HIFU beam on its way to the focus, i.e. the region in the pre-focal beam path, the so-called near-field of the HIFU beam (104,105), and may result in undesired necrosis (51) and skin burns (51,55,58-61). While the case-specific cooling rate is hard to predict, a compromise should be found between the prevention of overheating and the reduction of the treatment duration (104). It is therefore desirable to be able to monitor the temperature in the near-field, as well as to estimate adequate cooling times between sonications.

In clinical MR-HIFU applications, subtraction-based proton resonance frequency shift (PRFS) is the most commonly used MR thermometry (MRT) method (15,23). Temperature changes are calculated from changes in the phase of the complex gradient echo MR signal (25). During clinical MR-HIFU treatments, dynamic series of gradient-echo scans are normally acquired for

each sonication and phase differences are calculated by subtraction of the first image of the dynamic series, which serves then as a reference image. Temperature maps are then calculated by adding the assumed baseline temperature of the reference image (normally 37°C in patients) to the derived temperature change maps. It is assumed that the tissue has cooled down to the baseline temperature before starting the next sonication and dynamic series of PRFS MRT scans. If the cooling time between sonications is too short, the actual temperature in previously heated areas will be underestimated. In theory, this could be circumvented by using the firstly acquired image in the treatment procedure as a reference, instead of the first image of the dynamic series. However, when scanning over prolonged periods of time using subtraction-based PRFS MRT, temperature errors may occur due to field drift (25). Monitoring of heating over prolonged periods of time and estimating cooling times with the subtraction-based PRFS MRT method is therefore limited by field drift.

Multi-gradient echo (MGE) sequences allow the acquisition of spectroscopic data at high temporal and spatial resolution and efforts have been made to use this data for temperature imaging (28,34,106,107). Sprinkhuizen, et al. (29) proposed the MGE MRT method, which uses the MGE time-domain signal containing signal contributions of a component with a temperature dependent frequency and of a temperature independent component, such as water and fat. The method calculates temperatures from the resonance frequency difference between the components, which is extracted from the modulus of the MGE time-domain signal. The major difference with subtraction-based PRFS MRT is that each MGE MRT temperature map is individually reconstructed, without the need of a reference image. And as macroscopic magnetic field variations affect both resonance frequencies, field drift has minimal influence on MGE MRT (29).

In the application of MR-HIFU in abdominal organs, the tissues potentially at risk in the near-field area are the subcutaneous fat layer and adjacent muscle layer in the abdominal wall. Interestingly, these layers may provide the opportunity to use MGE MRT by placing the imaging slice at the interface, so as to make use of the partial volume effect to mix the signals of water and fat. As the MGE MRT measures temperatures in the muscle layer, it could be an alternative method to the recently published T2-based MRT

method, which measures temperature changes in the fat layer for near-field monitoring (31).

Here, we propose to use MGE MRT at the interface of the muscle and fat layers found in the abdominal wall, to monitor MR-HIFU induced heating. The performance of the method was assessed in an ex vivo water bath experiment, with probe measurements as the gold standard. An ex vivo HIFU experiment was performed to show both the ability to monitor heating of consecutive HIFU sonications in the presence of field drift and the ability to estimate cooling time constants. Also, the interleaved use of MGE MRT between scans of a clinical protocol was demonstrated in vivo in a patient during a clinical uterine fibroid MR-HIFU treatment.

METHODS

MULTI-GRADIENT ECHO MR THERMOMETRY (MGE MRT)

Due to the temperature dependence of the electron screening constant of hydrogen nuclei in water, the resonance frequency of protons in aqueous tissue is temperature dependent (25,26,34). By using fat, for which this is not the case, as a reference, the frequency difference Δf_{wf} can be used to calculate the temperature T via:

$$T = \frac{1}{\alpha}\left(\Delta\delta_{wf}(T_{ref}) - \frac{2\pi\Delta f_{wf}}{\gamma B_0}\right) + T_{ref} \qquad [1],$$

where α is the electron screening thermal coefficient and $\Delta\delta_{wf}(T_{ref})$ is the chemical shift difference between water and fat, measured at reference temperature T_{ref}. It is generally assumed that a calibrated value of $\Delta\delta_{wf}(T_{ref})$ can be used for the temperature calculations. Several values for $\Delta\delta_{wf}(T_{ref})$ have been reported in the literature (108-111). In our current study, the water and fat components originated from subcutaneous fat and adjacent muscle in the abdominal wall. The calibration measurement in gluteal subcutaneous fat and adjacent muscle ($\Delta\delta_{wf}(T_{ref} = 37℃) = 3.20\ ppm$) by Schick, et al. (108) was therefore the most suitable for this study and was used together with the electron screening thermal coefficient $\alpha = 0.01\ ppm/℃$ (33,34,112).

Recently, it was reported that the magnetic susceptibility distribution of aqueous and fatty tissue may introduce errors in temperature calculations based on water-fat frequency difference measurements (113). The magnetic susceptibility distribution induces local magnetic field variations that may be different for the water and fat components and thereby lead to variations in the observed $\Delta\delta_{wf}$. Therefore, the calibrated value of $\Delta\delta_{wf}(T_{ref})$ that should be used in equation [1] may not be the same for each voxel and using one single calibration value would thus lead to erroneous temperature calculations. As the magnetic susceptibility distribution depends on the spatial distribution of water and fat, these errors are systematic. Therefore, we propose to reconstruct relative MGE MRT temperature maps by subtracting subsequent MGE MRT temperature maps, in which systematic errors are cancelled out. And as the absolute temperature maps are reconstructed individually from scans started at different time points, it allows the interleaved use of relative MGE MRT. Unlike subtraction-based PRFS MRT, with MGE MRT relative temperature maps can be reconstructed by subtraction of any previously acquired scan without being affected by field drift that may have occurred during the period of time in between the two scans.

With the MGE MRT method, Δf_{wf} is extracted by voxel-wise fitting of the signal expression of a mixture of two resonance frequencies, each with their own transverse relaxation rate, to the MGE signal (29). In this case the sum signal can be written as:

$$S(t,T) = \sqrt{{A_w}^2 e^{-2R_{2,w}^* t} + {A_f}^2 e^{-2R_{2,f}^* t} + 2A_w A_f e^{-\left(R_{2,w}^* + R_{2,f}^*\right)t} \cdot \cos(2\pi\Delta f_{wf}(T)t + \Delta\varphi_{wf})} \quad [2],$$

where A_w is the water signal amplitude, A_f is the fat signal amplitude, $R_{2,w}^*$ and $R_{2,f}^*$ are the effective relaxation rates of water and fat and $\Delta\varphi_{wf}$ is the phase offset difference between water and fat directly after excitation.

In the current study, the number of fitting parameters was reduced to make the fitting procedure more robust. First, we assumed no significant phase offset difference between water and fat directly after excitation:

$\Delta\varphi_{wf} = 0$. Second, as numerical simulations showed modest sensitivity of Δf_{wf} to variations in the $R^*_{2,w}$ and $R^*_{2,f}$ values, we chose to exclude them from the fitting procedure by using measured values around body temperature. Last, numerical simulations also showed that the water-fat ratio influences the performance of the fit. Therefore, continuing on the assumption underlying the model described by Sprinkhuizen, et al. (29) that only two components are present, the signal amplitudes were rewritten as $A_w = A_0$ and $A_f = A_0(1-\lambda)$, where λ is a value between 0 and 1, representing the relative water signal amplitude in a voxel. By this redefinition, a water-fat ratio mask can be applied on the calculated temperature map based on the estimated λ. All this leads to the adapted fit function:

$$S(t,T) = A_0\sqrt{\lambda^2 e^{-2R^*_{2,w}t} + (1-\lambda)^2 e^{-2R^*_{2,f}t} + 2\lambda(1-\lambda)e^{-\left(R^*_{2,w}+R^*_{2,f}\right)t}\cdot\cos(2\pi\Delta f_{wf}(T)t)} \quad [3],$$

where A_0, λ and Δf_{wf} are left as fitting parameters.

Equation [3] was fitted to the data using an iterative nonlinear least-squares method with the following starting value, lower and upper boundary settings: $A_{0,start} = A_{0,estimation}$, $A_{0,low} = 0$, $A_{0,upp} = \infty$, $\lambda_{start} = 0.25$, $\lambda_{low} = 0$, $\lambda_{upp} = 1$, $\Delta f_{wf,start} = \Delta f_{wf}(40℃)$, $\Delta f_{wf,low} = \Delta f_{wf}(0℃)$, $\Delta f_{wf,upp} = \Delta f_{wf}(100℃)$. Here, $A_{0,estimation}$ was determined by extrapolating the signal value at the time point closest to the first water-and-fat in-phase time point to t=0 with a single exponential, with the mean of the measured $R^*_{2,w}$ and $R^*_{2,f}$ as the effective relaxation rate. From the extracted Δf_{wf} values, temperatures were calculated using equation [1]. To exclude potentially unreliable temperature values, voxels were masked out when the fitting procedure found $\lambda < 0.2$ or $\lambda > 0.8$ and when the coefficient of determination was $R^2 < 0.8$. For all experiments, both absolute temperature maps and relative temperature maps were reconstructed, where the latter were reconstructed by subtraction of the firstly acquired temperature map. The current implementation, made for this proof-of-concept study, was written in MATLAB (2013b, Mathworks, Natick, MA) and has not been optimized for speed. With this implementation, the computation time for

one voxel was 0.04 second using one CPU (Intel Xeon, 3.60 GHz) on a Windows 64-bit operating system (32 GB RAM).

EX VIVO WATER BATH EXPERIMENT

To measure the $R^*_{2,w}$ and $R^*_{2,f}$ values around body temperature and to investigate the MGE MRT performance on a muscle-fat interface, a water bath experiment was performed with an ex vivo porcine abdominal wall tissue sample. A closed circuit pump was used that circulated water of an adjustable temperature through a heat exchanger. The sample was spanned and kept in place by two wooden skewers which were fixated to the water bath. A schematic overview of the set-up is shown in Figure 1a.

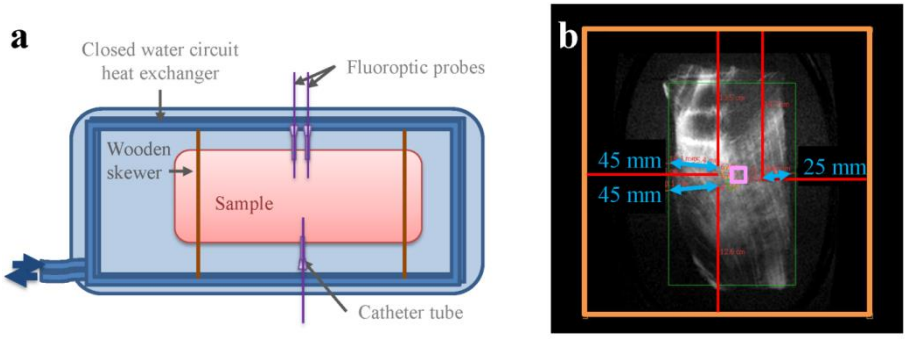

Figure 1. A schematic overview of the experimental setup of the ex vivo water bath experiment is shown in (a). In (b), a coronal T1-weighted image is shown, with blue arrows indicating the fibre lengths inside the sample. The probe locations are defined as distances from the edges of the MGE MRT image (red lines) of which the slice placement is depicted in orange. The pink square indicates the ROI used for the quantitative analysis, placed at the centre-of-mass of the three probe tips.

PERFORMANCE ASSESSMENT OF MGE MRT AT MUSCLE-FAT INTERFACE

MR images were acquired using an RF receiver coil consisting of two circular elements, with each an inner radius of 17 cm and an outer radius of 20 cm (Flex-L, Philips, Best, The Netherlands) on a clinical 1.5T MR scanner (Achieva, Philips Healthcare, Best, The Netherlands). Coronal MGE MRT imaging slices were positioned at the muscle-fat interface using T1-weighted anatomical

images. For these MGE MRT scans, the following parameter settings were used: number of echoes = 32, first echo (TE_0) = 1.4 ms, echo spacing (ΔTE) = 1.3 ms, flip angle (FA) = 20°, repetition time (TR) = 52.5 ms, slice thickness = 8mm, acquired in-plane pixel size = 2.8×2.8 mm^2, field of view (FOV) = 280×280 mm^2, reconstruction matrix = 112×112, resulting in a scan duration of 5.6s.

Three calibrated fluoroptic temperature probes (Luxtron, Santa Clara, CA) were inserted in the sample along the muscle-fat interface, using two guiding catheters of 45-mm length and one catheter of 25-mm length. First the catheters were fully inserted into the sample, the fibres were then inserted through the catheters and the catheters were retracted slightly while keeping the probes in position. This way, the probe tips were directly surrounded by tissue and the fibre lengths inside the sample equalled the catheter lengths. The probe tips were localized in the T1-weighted scan by the direction of the catheters, which produced voids, and the known length of the fibre (Figure 1b, blue arrows). Accordingly, the probe tip locations were defined in the MGE MRT scan as distances to the edges of the imaging slice (Fig.1b, orange square). A region of interest (ROI) of 5×5 voxels was defined at the centre-of-mass of the three probe tip locations for quantitative analysis (Fig.1b, pink square). The mean and standard deviation (SD) of the calculated temperatures within the ROI were calculated for each temperature point. Also, as a measure for the accuracy of the (relative) temperature measurements, the mean absolute error with respect to the mean (changes) of the three probe readings was calculated.

The sample was first heated and thermally stabilized, that is, a homogeneous temperature distribution in the sample. It was assumed that a stable situation was reached when the differences between the three temperature probe readings were less than 0.5°C and the readings were constant for at least 2 minutes. The sample was then measured during controlled cool down at four temperatures in the range of 37°C and 43°C, typically expected in the near-field (104). The controlled cooling was done by setting the heater of the closed circuit water pump stepwise to a lower temperature relatively close to the previous temperature, preventing large temperature gradients in the sample. An MGE MRT scan (5.6s duration) was

acquired once the temperature in the sample, measured by the probes, had been stable for at least two minutes.

R_2^* MEASUREMENTS IN WATER AND FAT

During the initial heating, R_2^* values of water and fat ($R_{2,w}^*$ and $R_{2,f}^*$) were measured around body temperature, when the probe readings were stable for at least 2 minutes. The MGE MRT sequence described above was used, with additional binomial RF excitation pulses to achieve selective excitation of either water or fat. R_2^* maps were created using the software of the MR console (Achieva, Philips Healthcare, Best, The Netherlands), which fits a single exponential with a maximum likelihood estimation algorithm. Mean $R_{2,w}^*$ and $R_{2,f}^*$ values were retrieved from an ROI of 300 voxels, placed in the middle of the sample, and were used in the data processing.

EX VIVO HIFU EXPERIMENT

MONITORING OF HIFU HEATING

To show the ability of the method to monitor HIFU heating, a porcine abdominal wall tissue sample was exposed to multiple consecutive sonications using a clinical MR-HIFU system (Sonalleve, Philips Healthcare, Vantaa, Finland) integrated into a clinical 1.5T MR scanner (Achieva, Philips Healthcare, Best, The Netherlands). The sample was placed on the HIFU window of the MR-HIFU table, with a gel pad in between. To mimic the near-field situation in the sample, the HIFU focus was placed in the agar gel placed on top of the sample (Figure 2a). An ultrasound gel-water emulsion was used to couple the gels with the sample.

Images were acquired using the built-in four-channel RF receiver coil inside the HIFU window together with the sixteen-channel top half of a cardiac RF receiver coil. Coronal MGE MRT imaging slices were positioned at the muscle-fat interface using T1-weighted anatomical images. The parameter settings for the MGE MRT scans were: number of echoes = 32, TE_0 = 1.4 ms, ΔTE = 1.3 ms, FA = 20°, TR = 52.5 ms, slice thickness = 8mm, acquired in-plane pixel size = 2×2 mm^2, FOV = 250×200 mm^2, reconstruction matrix = 432×432, resulting in a scan time of 5.2s.

First one location was sonicated three times and then two other locations were sonicated once (80W, 4-mm volumetric cells (114)). For each sonication

30 MGE MRT scans were acquired dynamically and the dynamic series of subsequent sonications started directly after each other, so that the temperature was measured continuously throughout the experiment. The sonication started with the start of the fourth dynamic scan and ended after 60 seconds.

MAGNETIC FIELD DRIFT MEASUREMENT

To have an indication of the magnetic field drift during this experiment, the non-temperature related temporal phase evolution was measured in MGE MRT scans acquired at echo time TE = 19.6 ms (15th echo), similar to the echo times typically used in clinical PRFS MRT sequences (70,115). In an ROI of 5×5 voxels, selected away from the heated regions, the field drift was calculated from the temporal evolution of the mean phase value in the ROI. Accordingly, it was converted to the equivalent temperature change as calculated by the subtraction-based PRFS MRT method.

2.3.3. Cooling constant mapping. To estimate cooling time constants (τ), the time-evolutions of the calculated temperatures during the cooling phases were modeled of each voxel using a mono-exponential model:

$$T(t) = (T_0 - T_{baseline})\, e^{-\frac{t-t_0}{\tau}} + T_{baseline} \qquad [4],$$

where t_0 is the known time at which the cooling started, T_0 is the temperature at which the cooling started and $T_{baseline}$ is the baseline to which the temperature equilibrates. An iterative nonlinear least-squares method was used with the following settings: $T_{0,start} = 37$°C, $T_{0,low} = 0$°C, $T_{0,upp} = 100$°C, $T_{baseline,start} = 37$°C, $T_{baseline,low} = 0$°C, $T_{baseline,upp} = 100$°C, $\tau_{start} = 250\ s$, $\tau_{low} = 0\ s$, $\tau_{upp} = \infty\ s$. A τ map was reconstructed for voxels with the coefficient of determination $R^2 > 0.5$ and $T_{baseline} > 20$°C. Voxels of interest (VOI) were selected in four different heating areas: 1st sonication area, heated three times (VOI 1); 2nd sonication area, heated once (VOI 2); overlapping area of 2nd and 3rd sonication, heated twice (VOI 3); and 3rd sonication area, heated once (VOI 4). ROIs of 15×15 were drawn around these voxels and the mean τ values of the ROIs were calculated.

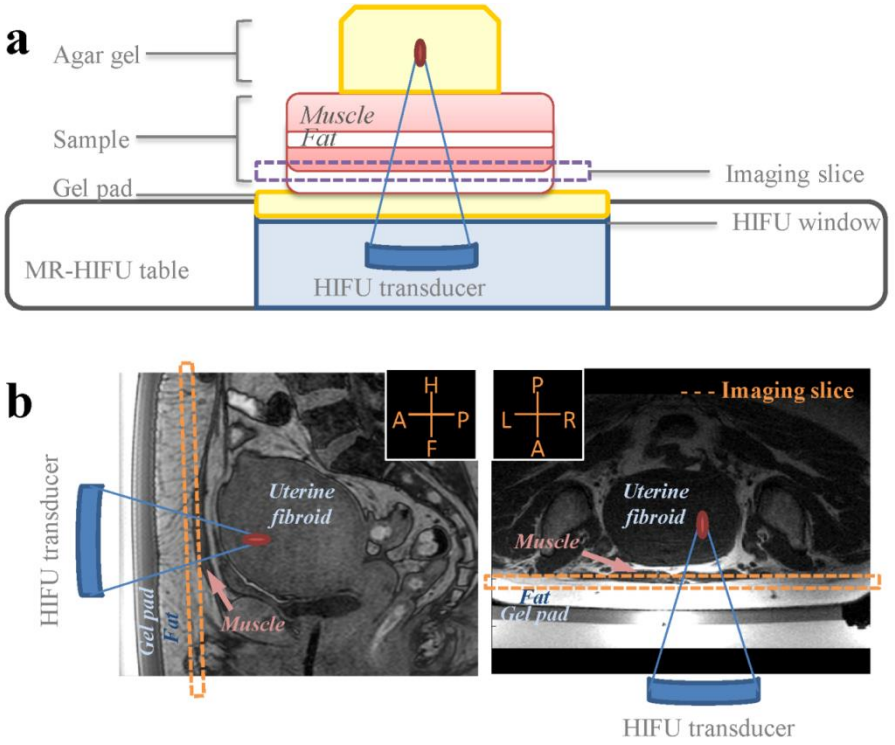

Figure 2. Schematic overviews of the HIFU setups of the ex vivo experiment (a) and of the in vivo demonstration (b) in patient during a clinical uterine fibroid MR-HIFU treatment, on a sagittal and transverse T1-weighted planning scan. In both the ex vivo and in vivo setup, the imaging slice was placed in the near-field of the HIFU focus, which is the area along the HIFU beam path outside the target area. In (c), a schematic overview is shown of the scan and sonication sequence during the in vivo demonstration.

IN VIVO DEMONSTRATION

To demonstrate the use of the method in vivo, interleaved in a clinical routine, MGE MRT scans were acquired in a patient before and after sonications during a clinical uterine fibroid MR-HIFU treatment using a clinical MR-HIFU system (Sonalleve, Philips Healthcare, Vantaa, Finland) integrated into a clinical 1.5T MR scanner (Achieva, Philips Healthcare, Best, The Netherlands). The treatment was approved by the Institutional Review Board with a waiver of consent and written informed consent was obtained from the patient for using the acquired data for scientific purposes. The patient was positioned such that the uterus was directly above the HIFU window. A gel pad was placed between the patient's skin and the HIFU window (Figure 2b) and degassed water was used to couple the gel pad to the skin.

The built-in two-channel RF receiver coil inside the HIFU window was used together with a three-channel HIFU pelvis receiver coil positioned on the patient's back. Coronal MGE MRT imaging slices were positioned at the muscle-fat interface using T1-weighted anatomical images. For these MGE MRT scans, the following parameter settings were used: number of echoes = 32, TE_0 = 1.4 ms, ΔTE = 1.3 ms, FA = 20°, TR = 52.5 ms, slice thickness = 8 mm, acquired in-plane pixel size = 2×2 mm^2, FOV = 350×350 mm^2, reconstruction matrix = 192×192, resulting in a scan time of 9.5s.

HIFU sonications were performed with 8-mm volumetric cells (114) and powers were chosen by the clinician. Figure 2c shows a chronological overview of the image acquisitions, HIFU sonications and cooling periods. The therapy was preceded by an MGE MRT scan and two test sonications (100W and 110W, both 16s), followed by 90s of cooling. Subsequently, MGE MRT scans were acquired before and after the first two therapeutic sonications of the therapy (200W 39s and 240W 30s) with 2min cooling in between. Finally, after 3min cooling, the last MGE MRT scan was acquired.

RESULTS

EX VIVO WATER BATH EXPERIMENT

R_2^* MEASUREMENTS IN WATER AND FAT

The mean $R_{2,w}^*$* and $R_{2,f}^*$ values over the ROI, measured close to body temperature at (35.6±0.2)°C, were: $R_{2,w}^* = 29.1\ s^{-1}$ and $R_{2,f}^* = 31.3\ s^{-1}$. These values were used in the data processing for all experiments.

PERFORMANCE ASSESSMENT OF MGE MRT AT MUSCLE-FAT INTERFACE

Multi-GE images were acquired during the water bath experiment at the following temperatures, as measured by the temperature probes (mean±standard deviation): (42.8±0.4)°C, (40.4±0.5)°C, (39.2±0.5)°C and (37.4±0.4)°C. The temperature changes measured by the probes were thus: (-2.4±0.6)°C, (-3.6±0.6)°C and (-5.4±0.6)°C. The time between the MR acquisitions were 30 minutes, 15 minutes and 30 minutes.

The reconstructed relative temperature maps show homogeneous temperature distributions and cool down (Fig.3a). In the corresponding reconstructed absolute temperature maps (Fig.3b) spatial heterogeneities can be observed which were cancelled out in the relative temperature maps, indicating that they were systematic errors. The voids outside the sample were induced by the catheters through which the probes were inserted. In Figure 3c, the mean and SD (error bars) of the calculated relative temperatures in the ROI (Figure 3a, pink square) are plotted against the mean probe temperature changes and show good correspondence. The mean calculated relative temperature in the ROI were (mean±standard deviation): (-2.5±0.9)°C, (-3.3±0.9)°C, and (-5.1±1.1)°C and the mean absolute error was 0.3°C. In Figure 3d, the mean and SD (error bars) of the calculated absolute temperatures in the ROI are plotted against the mean probe temperatures and shows that the temperatures were consistently overestimated. The mean calculated temperatures in the ROI were (mean±standard deviation): (45.4±1.3)°C, (42.9±1.8)°C, (42.0±1.7)°C and (40.3±1.4)°C and the mean absolute error was 2.7°C.

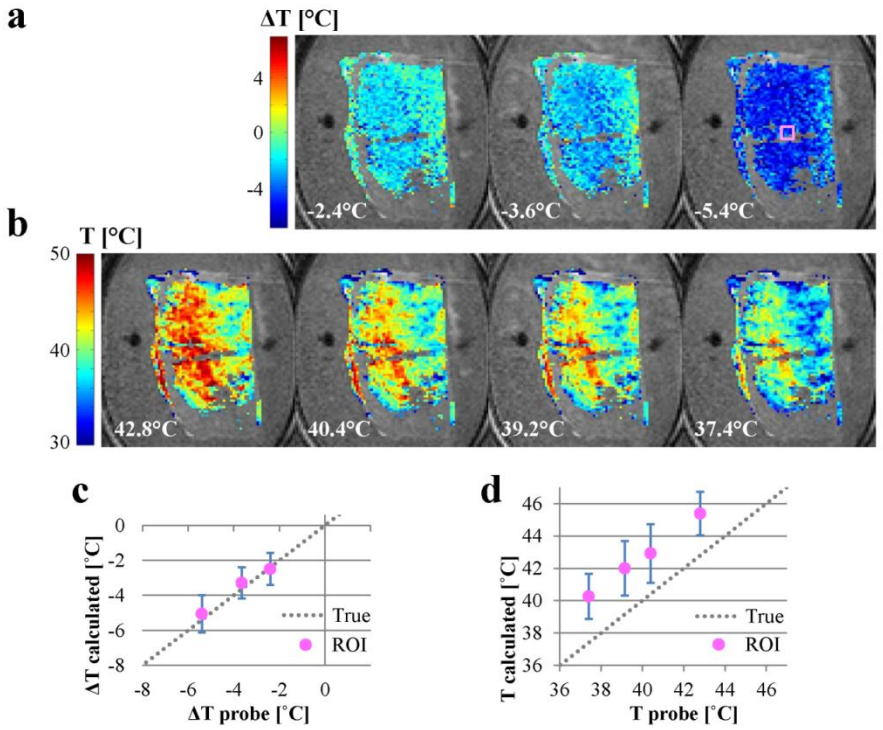

Figure 3. Results of the ex vivo water bath experiment (illustrated FOV = 200×200 mm^2): (a) reconstructed relative temperature maps; (b) reconstructed absolute temperature maps; (c) the mean calculated ROI relative temperatures plotted against the mean probe temperature changes; (d) the mean calculated ROI absolute temperatures plotted against the mean probe temperatures. The measured probe temperatures (or temperature changes) are shown in the bottom-left of each (relative) temperature map. The pink square in (a) indicates the ROI location and the voids outside the sample were induced by the catheters through which the probes were inserted. The error bars in the plots indicate the SD in the ROI.

EX VIVO HIFU EXPERIMENT

MONITORING OF HIFU HEATING

Figure 4a shows the reconstructed relative temperature maps before, during and after HIFU; Figure 4b shows the corresponding reconstructed absolute temperature maps. Similar to the water bath experiment results, the spatial inhomogeneities observed in the absolute temperature maps were cancelled out in the relative temperature maps. The heat accumulation caused by the

consecutive sonications can be clearly seen, especially in the first three sonications at the same location. The heated area of the fifth sonication partially overlaps with the previously heated area and higher temperatures can be observed (fifth row, in the middle of the sample). Furthermore, cooling is visible in all post-HIFU (relative) temperature maps.

MAGNETIC FIELD DRIFT MEASUREMENT

The measured magnetic field drift during the ex vivo HIFU experiment is shown in Figure 5 in ppm and in equivalent temperature error, as calculated with subtraction-based PRFS MRT. The results showed that the field drift over the duration of the experiment (about 17 minutes) resulted in an equivalent temperature error of 64°C, with a rate of approximately 4°C per minute. Such errors were not observed in the (relative) temperature maps of this experiment (Figure 4), indicating that the MGE MRT temperature calculations were not affected by the field drift.

COOLING CONSTANT MAPPING

The reconstructed cooling time constant (τ) map is shown in Figure 6a. The locations of the four VOIs are indicated in the map and their temperature time-evolutions are plotted in Figure 6b, together with their fitted curves. The plots show that equation [4] could be fitted well to the cool down phase of the data and the different heating patterns can be seen: VOI 2 and VOI 4 were sonicated once, VOI 3 twice and VOI 1 three times. Interestingly, the temperature-time curve of VOI 2 shows a slight increase before it was directly heated by sonication, indicating indirect heating via conduction. VOI 2 was located nearby the area heated by the first three sonications and it can be observed in the relative temperature maps (Fig 6b) that the heating spreads to a larger area than was directly sonicated, including VOI 2. Also note that the temperature increase start and end time points of VOI 3 correspond with those of VOI 2 and VOI 4. The mean τ value was largest in ROI 1 (256s), which was heated three times, followed by the mean τ value of ROI 3 (249s), which was heated twice. Of the ROIs that were heated once, ROI 2 was located close to a previously heated area and its mean τ value was larger (224s) than of ROI 4 (172s).

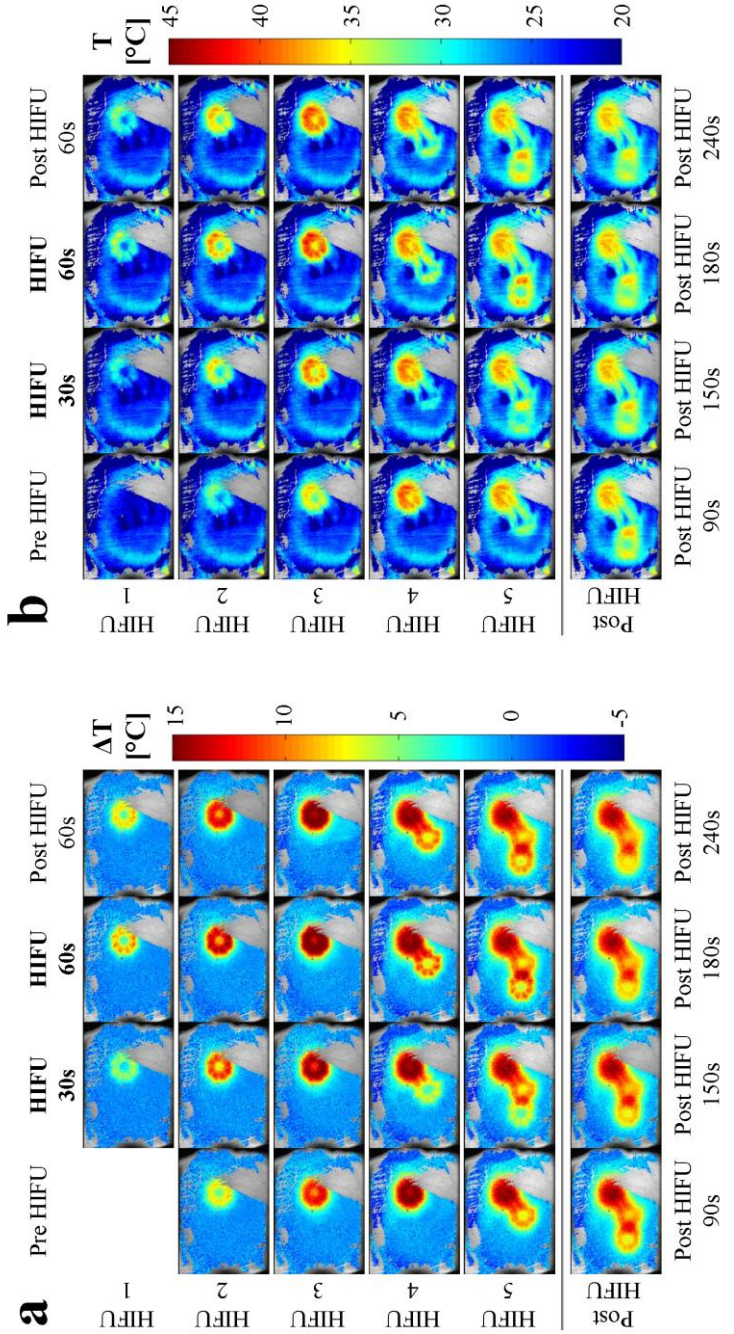

Figure 4. Reconstructed relative temperature maps **(a)** and absolute temperature maps **(b)** of the ex vivo HIFU experiment (illustrated FOV = 250×180 mm^2); the rows represent consecutive sonications (all with 80W for 60s) and the columns represent time points in the dynamic series. The data of the last row was acquired after HIFU sonication end point, with the same time points in the dynamic series as the other rows.

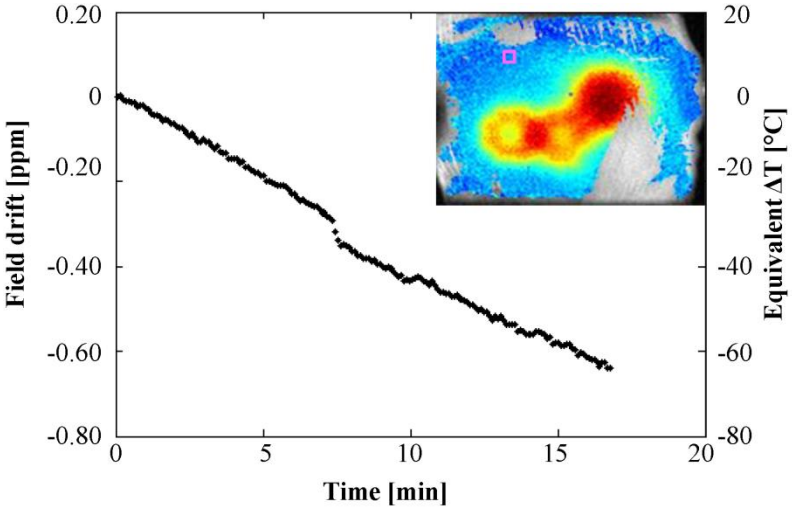

Figure 5. The field drift during the ex vivo HIFU experiment. The ROI used for the field drift measurements was selected away from the heated regions and is indicated with a pink square in the inset temperature map (after last sonication, post HIFU 90s).

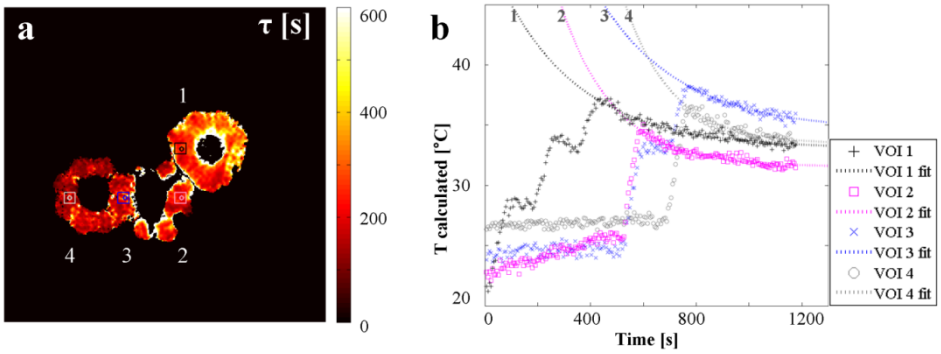

Figure 6. In (a), the reconstructed cooling constant (τ) map is shown with the VOIs (circles) and corresponding ROIs (squares) for the calculation of the mean τ values. The calculated temperature time-evolutions of the VOIs are plotted in (b) together with their fitted curves: the numbers (1-4) correspond to the VOI numbers, indicated in (a).

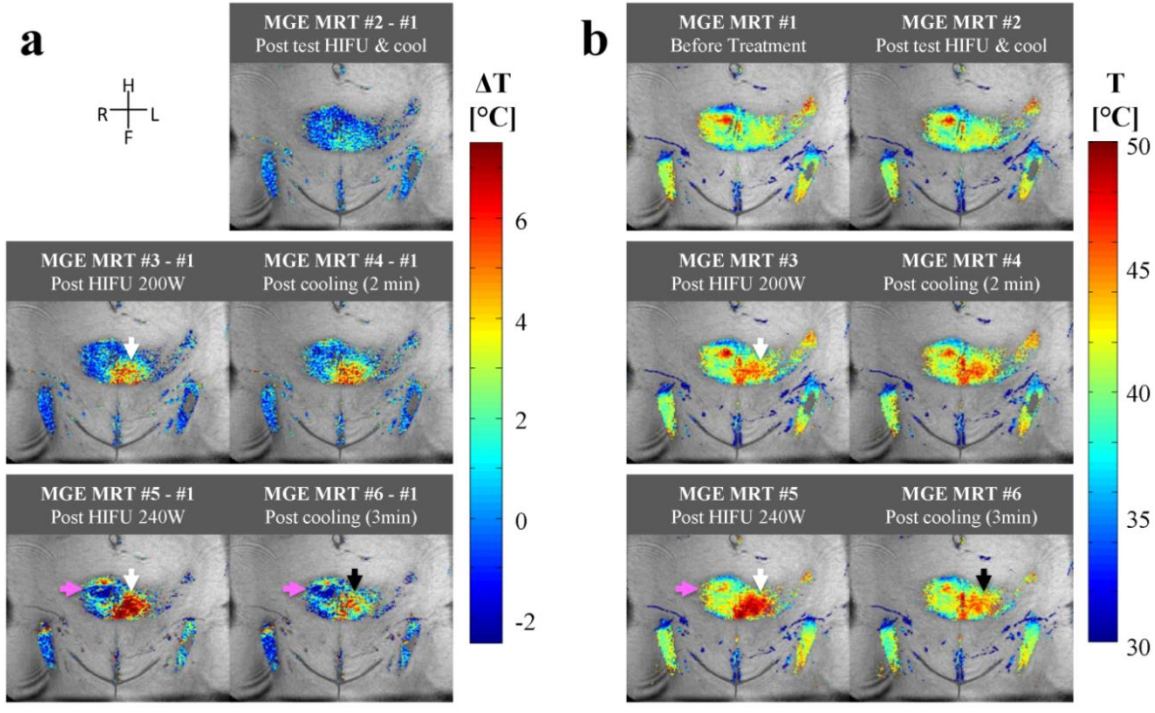

Figure 7. Reconstructed relative temperature maps (a) and absolute temperature maps (b) of the in vivo data acquired in a patient during a clinical uterine fibroid MR-HIFU treatment (illustrated FOV = 350×300 mm^2). The numbers preceding the descriptions above each map correspond to the MGE MRT scan numbers in Figure 2c. The white arrows point out temperature increase, the black arrows point out temperature decrease. The pink arrows point out misregistration errors due to slight patient motion between MGE MRT scans 4 and 5.

IN VIVO DEMONSTRATION

Relative temperature maps calculated from in vivo data acquired in a patient during a clinical uterine fibroid treatment are shown in Figure 7a and the corresponding reconstructed absolute temperature maps in Figure 7b. The first absolute temperature map (Fig.7b), acquired before treatment, shows spatial heterogeneities unlikely representing actual temperature distributions. These heterogeneities were consistently present in the subsequent temperature maps and were cancelled out in the relative temperature maps (Fig.7a). Temperature increase after HIFU sonication (white arrows) and temperature decrease after cooling (black arrows) can be observed clearly in the relative maps, where the observer is not distracted by the spatial heterogeneities such as those seen in the absolute maps.

Between MGE MRT scans 4 and 5 slight patient motion was observed. The artificial high temperature spot in the top-left of temperature maps 1 to 4 was less pronounced in absolute temperature maps 5 and 6, resulting in erroneous relative temperatures (pink arrows).

DISCUSSION

The relative temperature maps of the ex vivo controlled water bath experiment were homogeneous and the relative temperature measurements in the ROI showed good correspondence with the mean probe temperature changes (mean absolute error 0.3°C, mean SD 1.0°C). Systematic errors occurred in the absolute temperature calculations and caused spatial heterogeneities in those maps, but did not occur in the relative temperature maps. This was also reflected in the observed offset in the temperature plot of the ROI (Figure 3a), which was absent in the relative temperature plot.

The systematic errors in the absolute temperature measurements are most likely due to the magnetic susceptibility distribution of water and fat (28,113), which affects the local magnetic field. Baron, et al. (113) showed that the influence of the magnetic susceptibility on the chemical shift depends on the water-fat distribution in relation to the main magnetic field. The calibration of $\Delta\delta_{wf}(T_{ref})$ in equation [1] may therefore not be correct everywhere, depending on the (local) water-fat distribution, and systematic

errors will occur in the absolute temperature measurements. These systematic errors are cancelled out in the relative temperature measurements, as these are reconstructed by subtracting individual absolute temperature maps. In addition, the proposed geometry in this study was based on the adjacent flat layers of muscle and fat in the abdominal wall and has the advantage of having a fixed orientation with respect to the main magnetic field. This is especially true for the MR-HIFU setup for the application on abdominal organs, where subjects are positioned with the near-field region (pre-focal beam path region) on a flat gel pad. We have shown ex vivo that using MGE MRT in this specific geometry, relative temperatures could be calculated with high accuracy (0.3°C).

The results of the ex vivo HIFU experiment showed that MGE MRT enables capturing subsequent heating by consecutive sonications. Similar to the ex vivo water bath experiment, the spatial heterogeneities observed in the temperature maps due to susceptibility effects were cancelled out in the relative temperature maps. The thermal built-up could be seen clearly in the temperature maps and even clearer in the relative temperature maps. As the relative temperature maps are reconstructed using individual scans started at different time points, it allows the interleaved use of relative MGE MRT for excellent monitoring of heating. The experimental setup was chosen such that it resembles the in vivo near-field case, where the HIFU focus is positioned in deep tissue and the imaging slice is placed in the near-field area of the HIFU focus.

The interleaved use of MGE MRT was demonstrated in vivo, where the scan was positioned in the near-field area of the HIFU focus and acquired between the scans of the clinical protocol. Heating in the near-field region upon HIFU sonication and subsequent cooling could be observed. Similar to the ex vivo experiments, the spatial heterogeneities observed in the temperature maps were cancelled out in the relative temperature maps. Slight patient motion occurred between MGE MRT scans 4 and 5. The region with artificially high temperatures in the temperature maps preceding the motion was less pronounced after motion. This resulted in errors in the relative temperature measurements and may be attributed to misregistration between subtracted temperature images.

The major advantage of MGE MRT over subtraction-based PRFS MRT is its insensitivity to field drift. The measured magnetic field drift over the ex vivo HIFU experiment showed a dramatic equivalent temperature error rate of 4°C per minute. The equivalent temperature error over the duration of the experiment of 64°C was similar to the 70°C reported by Sprinkhuizen, et al. (29) during their experiment at 3.0T. Since these errors were not observed in the reconstructed relative and absolute temperature maps, this demonstrates the usability of MGE MRT over prolonged periods of time without being affected by field drift.

Fat-referenced subtraction-based PRFS MRT has been proposed for field drift correction, by making use of the negligible temperature dependency of the chemical shift of fat (94,116-119). In these techniques, fat is used to correct for non-temperature dependent changes in the phase of the complex MR signal. Although they may correct for field drift, these fat-referenced methods are still based on phase difference maps and subsequent phase maps are often subtracted to avoid phase wrapping (116). Alternatively, phase unwrapping algorithms could be considered (120-122). Contrastingly, phase wrapping is not an issue for MGE MRT as the frequency difference between water and fat is used for temperature calculations rather than the phase. Also, relative MGE MRT temperature maps are reconstructed by subtractions of individually reconstructed absolute temperature maps. It therefore allows subtractions of any arbitrary combination of absolute MGE MRT temperature maps.

Referenceless or self-referenced PRFS MRT (123,124) circumvents the need to correct field drift by estimating the baseline phase from each temperature map itself. The phase outside the expected heated region is used to estimate the background phase of the inner expected heated region, for example using polynomial approximations. However, this method is based on the assumption that only a small and well-localized region is affected by the thermal treatment, which does not apply for near-field heating as the intersection of the HIFU cone with the near-field region covers a large area (104,105). Additionally, the size of the heated area in the near-field may increase even more when consecutive sonications at different locations are performed to cover the target volume, potentially limiting the robustness of the estimation of the baseline phase.

Cooling time constants τ were estimated from the MGE MRT temperature measurements in the ex vivo HIFU experiment using a mono-exponential fit, which fitted well to the data (Fig.6b). Interestingly, the differences in the mean τ values between the four ROIs could be well explained by the sonication pattern: the lowest value was found in the ROI that was sonicated once and was not close to a previously heated area; the highest value was found in the ROI that was sonicated three times. In this study, the cooling time constants were estimated from temporal densely sampled temperature points. In practice, temperature measurements could be done every few minutes instead, to estimate the cooling time constant or how much the region has cooled since any previous scan. Because (relative) temperature maps are field drift insensitive and reconstructed from individual scans, MGE MRT provides the opportunity to acquire knowledge about the cooling with interleaved scans. In the current clinical MR-HIFU workflow, long cooling time periods are taken between sonications. This is to make sure that all tissue has cooled down to the baseline temperature, because otherwise temperatures will be underestimated at previously heated regions with the clinically used subtraction-based PRFS MRT. This would potentially lead to undesired overheating. With knowledge of the cooling rate, better estimations can be made for the required waiting time between sonications. The treatment time efficiency could then be enhanced by making a compromise between the prevention of overheating and the reduction of the treatment duration.

MGE MRT was shown to be a promising tool for monitoring heating in the near-field. This method has, however, some limitations. Most importantly, the difference in the magnetic volume susceptibility of water and fat causes systematic errors in the temperature measurements, because of the locally induced magnetic field variations. But by subtracting individual MGE MRT temperature maps, relative MGE MRT temperature maps can be reconstructed where these systematic errors are cancelled out. While relative MGE MRT measures temperature changes, like subtraction-based PRFS MRT, it still has the advantage of being field drift-corrected and the flexibility of using individually reconstructed temperature maps. All relative temperature maps in this study were reconstructed by the subtraction of the firstly acquired MGE MRT temperature map to show the capturing of the

cumulative heating. However, any arbitrary combination of MGE MRT temperature maps could be subtracted from each other to see the temperature changes between those time points. Another limitation is that, depending on the application, not all voxels in the field of view may satisfy the condition that both muscle and fat contribute to the MR signal. Also, the temperature dependence of the susceptibility of fat may induce minor additional errors (125).

CONCLUSION

We have shown MGE MRT can be used for monitoring the MR-HIFU heating in the near-field, by placing the imaging slice at the interface of the abdominal muscle and fat layers. While the derived absolute temperature maps were shown to be affected by susceptibility effects, the relative temperature maps provide excellent visualization of the heating without interference of field drift. Because the (relative) temperature maps are reconstructed from individually acquired scans, MGE MRT can be used interleaved. Cooling time constants could be estimated from the temperature measurements, which may be a useful tool for treatment monitoring.

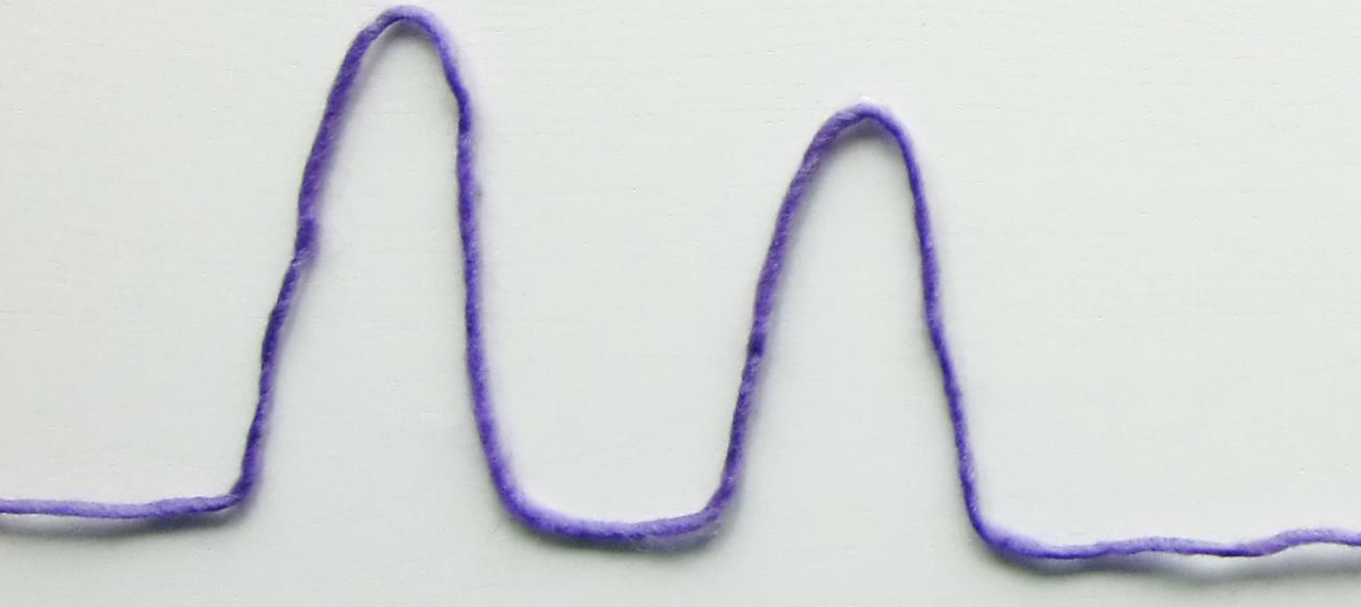

"LOGIC WILL GET YOU FROM A TO B,

IMAGINATION WILL TAKE YOU EVERYWHERE"

– ALBERT EINSTEIN

Chapter 4

Short- and long-time MR signal behavior of homogeneously distributed water and fat

- implications for fat-referenced MR thermometry

Submitted for publication

INTRODUCTION

The magnetic field experienced by local spins is influenced by static magnetic field inhomogeneities generated by spatial variations in magnetic susceptibility. In MR image acquisitions, sub-voxel susceptibility variations will induce spin dephasing and signal loss in an MR imaging voxel (126). Spin dephasing is induced by two basic phenomena: the dispersion of local nuclear frequencies and nuclear diffusion. When spin dephasing induced by local nuclear frequency differences occurs faster than spin dephasing due to diffusion, the system is in the so-called static dephasing regime. For this regime, Yablonskiy and Haacke (127) created a theoretical framework based on random distributions of perturbing spheres and cylinders in water. Their analytical derivation predicted that the resulting MR signal decay of water would first show quadratic exponential behavior, followed by shifted mono-exponential behavior with an oscillating part. Their theory was validated with numerical simulations and experiments of various systems of perturbers embedded in water, notably tissue in the presence of a paramagnetic MR contrast medium (128), paramagnetic deoxyhemoglobin in the blood (129), trabecular bone and bone marrow (130) and super paramagnetic iron oxide labeled cells (131). In these systems, the perturbers were considered as point objects and any signal from the perturbers was ignored.

Water-fat emulsions, such as mayonnaise, are macroscopically homogenous systems of water with microscopically randomly distributed spherical fat droplets and are often used as a water-fat phantom in MR experiments (107,132-134). In such water-fat emulsions, fat can be considered a collection of perturbing objects embedded in water. In this pertuber-medium system, the signal behavior of both water and fat are of importance and thus the signal of both the pertuber and the medium should be considered. In these systems, water and fat are exposed to the same static magnetic field and the field inhomogeneities are induced by the magnetic susceptibility differences between water and fat. It is likely that the susceptibility effects on the local nuclear frequencies are similar for water and fat. Since the water signal shows different exponential behavior in two regimes as a result of spatial variations in magnetic susceptibility, it is likely that this will also be the case for fat.

It has been proposed to use fat as a reference to water in MR thermometry (MRT), to calculate absolute temperatures from the measured frequency difference between water and fat. This can be done by either fitting two Lorentzian peaks in the frequency domain (28) or, equivalently, by fitting two mono-exponential functions with a frequency difference in the time-domain (29). Errors in the order of 10°C were observed in tissues with a macroscopically inhomogeneous distribution of water and fat (28,135). Recently, the susceptibility difference between fat and water has been reported to influence fat-referenced MRT in heterogeneously distributed water and fat (113). Even in mayonnaise, a macroscopically homogeneous mixture of water and fat, temperature errors of 2°C were reported (28). With numerical simulations of randomly distributed fat spheres embedded in water, Baron, et al. (113) demonstrated that the time-domain fitting errors increased with increasing sub-voxel fat fraction. This finding implies that the sub-voxel water-fat distribution influences the accuracy of the frequency difference measurements, extracted from the fitting of two mono-exponentials to the time-signal. The water signal has different exponential behavior on the short- and long-time scales, and the same may hold for fat. If the signal sampling covers both regimes, the time-signal may not be simply described with mono-exponentials. Therefore, fitting two mono-exponentials to such time-signal may thus induce errors. To investigate this further, it is necessary to first characterize the fat signal and define the time scales of the two regimes.

In this study, we explored the signal behavior of macroscopically homogeneously distributed water and fat, where fat was considered a collection of perturbing objects in a water medium. We have not yet succeeded in finding an analytical description for the signal of the perturber in the static dephasing regime, similar to that of Yablonskiy and Haacke. Instead, we explored the signal behavior of water and fat arising from a three-dimensional random distribution of fat spheres in water using numerical simulations. The simulated complex water time-signals were compared with the theoretical MR signal description by Yablonskiy and Haacke (127). Subsequently, we investigated whether the simulated complex fat time-signal can be described similarly. To explore the implications on fat-referenced MRT, the simulated signals were sampled in different time ranges.

The sampled signals were then fitted in the time-domain to find the susceptibility-induced error in the extracted frequency difference and in the corresponding temperature (29).

THEORY

WATER SIGNAL IN THE PRESENCE OF RANDOMLY DISTRIBUTED SMALL PERTURBERS

Yablonskiy and Haacke (127) described the theoretical MR signal behavior of magnetically inhomogeneous tissue for a two-component model, comprising randomly distributed spherical objects (perturbers) with a different magnetic susceptibility than water, embedded in a water medium. To characterize the field induced by a spherical perturber, Yablonskiy and Haacke (127) defined the characteristic frequency $\delta\omega$ in [rad s^{-1}]:

$$\delta\omega = \frac{1}{3}\,\gamma(\chi - \chi_0)B_0 \qquad [1],$$

where γ is the gyromagnetic ratio in [rad s^{-1} T^{-1}], χ is the susceptibility of the perturbers, χ_0 is the susceptibility of the medium and $B_0 = \left|\overrightarrow{B_0}\right|$ is the field strength in [T] of the main magnetic field $\overrightarrow{B_0}$ in which the system is located. At the j^{th} observation point, the external frequency ω_{ij} induced by the i^{th} spherical perturber with characteristic frequency $\delta\omega$, radius a_i, located at $\overrightarrow{r_{ij}}$, has the form:

$$\omega_{ij} = \delta\omega \cdot \left(\frac{a_i}{r_{ij}}\right)^3 \left(3\cos^2\theta_{ij} - 1\right) \qquad [2],$$

where distance $r_{ij} = \left|\overrightarrow{r_{ij}}\right|$ and θ_{ij} is the angle between $\overrightarrow{r_{ij}}$ and $\overrightarrow{B_0}$. The induced dispersion in nuclear frequencies leads to MR signal decay in the time-domain. Yablonskiy and Haacke (127) found that for spherical perturbers, the water signal behavior was separated in two time scales. In the short-time scale, the signal obeys a quadratic exponential decay; in the long-time scale, the signal decay may be characterized as shifted mono-exponential with an oscillating part (127):

$$for\ t \le \tau:\ \bar{S}(t) = \rho \cdot (1-\zeta) \cdot \exp(-0.4 \cdot \zeta \cdot (\delta\omega \cdot t)^2) \qquad [3a],$$

$$for\ t \ge \tau:\ \bar{S}(t) = \rho \cdot (1-\zeta) \cdot \exp(-R2' \cdot |t - t_s|) \cdot \exp(-i \cdot \Delta\omega \cdot t) \qquad [3b].$$

Here, ρ is a coefficient depending on parameters as spin density, flip angle, hardware sensitivity, etc. and $\zeta = v/V$ is the relative volume fraction occupied

by the pertubers, where *v* is the total volume occupied by the perturbers and *V* is the total volume of the system; that is the medium and the perturbers. In equation [3b], $t_s \approx (C \cdot \delta\omega)^{-1}$ is the time shift in [s], $R2' = \zeta / t_s$ is the relaxation rate of the susceptibility-induced signal decay in [s^{-1}] and $\Delta\omega \approx -C' \cdot \zeta \cdot \delta\omega$ is the frequency offset in [rad/s]. In their analytical derivation, Yablonskiy and Haacke (127) have approximated the real and imaginary parts of the integral over the observation points with their asymptotic forms. This resulted in the factor 0.4 in equation [3a] and in the constants $C = 2\pi/(3\sqrt{3})$ and $C' = 2/\sqrt{3}\ln\left((\sqrt{3}+1)/(\sqrt{3}-1)\right)$. Finally, Yablonskiy and Haacke (127) found that the water signal was separated in the short and the long-time scale at $\tau_w = 1.5/\delta\omega$.

In their analytical derivation, Yablonskiy and Haacke made several assumptions. First, the standard statistical assumption was made that the number of perturbers in the volume of interest is >> 1. Second, the low perturber concentration limit, ζ << 1, should be satisfied. Third, the static dephasing regime is assumed, which is when spin dephasing resulting from local differences in nuclear frequencies occurs faster than spin dephasing due to diffusion. Last, the global magnetic field inside the medium was assumed to be homogeneous.

WATER AND FAT SIGNAL FOR A RANDOM DISTRIBUTION OF FAT SPHERES IN WATER

Water-fat systems can be considered a system of perturbing fat objects embedded in water. An important aspect of this specific system is that the signal of the perturber, fat, cannot be ignored. The origins of the signals of water and fat are complementary: fat signals arise from the perturbing objects and water signals arise from the whole system excluding the objects. Since water and fat have a different chemical shift and thus different resonance frequencies, the influence of susceptibility-induced field shifts on the two resonances can be considered separately.

In a system of randomly distributed spherical fat objects embedded in water, e.g. water-fat emulsions, the behavior of the complex water time-signal can be described analytically by equation [3] if the assumptions above apply. With a difference of 1.26 ppm in susceptibility between water and fat (85,136), the characteristic frequency $\delta\omega_w$ of the water will be about 168.5 rad/s at 1.5 T (Eq.[1]) and thus $\tau_w \approx$ 8.9 ms and $t_{s,w} \approx$ 4.9 ms. The observed

fat signal originates from observation points located in fat spheres. The nearest observation points in fat of which the measured signal is affected by a perturbing fat sphere, are those located in the nearest fat sphere. Owing to this geometrical restriction, the effective field as experienced by fat will be different from that of water. The implications for the observed fat signal are investigated in this study using numerical simulations.

METHODS

To investigate the resonance frequency distributions and the resulting time-domain MR signals of water and fat in macroscopically homogenous sub-voxel water-fat distributions, numerical simulations were performed in MATLAB (2013b, Mathworks, Natick, MA).

NUMERICAL MODEL

A three-dimensional numerical phantom was created of a water-fat distribution, placed in a static magnetic field B_0. The medium was defined as a water sphere with radius R so that the magnetic field inside the medium was homogeneous. The perturbers were equally sized spherical fat objects with radius a. The relative fat volume fraction ζ was defined, from which the (rounded) number of fat objects M was calculated. All objects were assigned random locations and were entirely inside the water sphere, where no overlap exists between objects. A cubic volume of interest (VOI), representing an MR imaging voxel, was defined entirely inside the water sphere and positioned concentrically with the water sphere. In the VOI, N observation points were assigned to random positions, without overlap. Figure 1 shows a schematic representation of the numerical phantom.

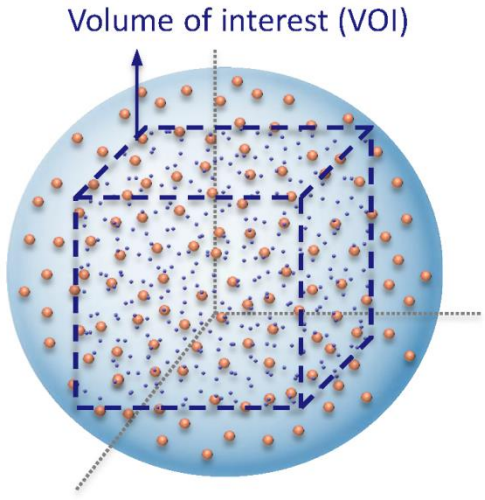

Figure 1. A schematic representation is shown of the numerical phantom used for the simulations: spherical fat objects (orange) at random positions in a spherical water medium (blue). Observation points (purple) were randomly distributed in a cubic volume of interest (VOI; purple dashed lines).

At the j^{th} observation point, the field shift $\delta B_{z,ij}$ induced by the i^{th} object was calculated as follows (137):

$$for\ r_{ij} < a\text{:}\ \ \delta B_{z,ij}(r_{ij},\theta_{ij}) = \frac{1}{3}\chi_0 B_0 \qquad \text{[4a]},$$

$$for\ r_{ij} > a\text{:}\ \ \delta B_{z,ij}(r_{ij},\theta_{ij}) = \frac{1}{3}\chi_0 B_0 + \frac{1}{3}(\chi-\chi_0)\, B_0 \frac{a^3}{{r_{ij}}^3}\left(3\cos^2\theta_{ij}-1\right) \qquad \text{[4b]},$$

where $r_{ij} = \left|\overrightarrow{r_{ij}}\right|$ is the distance between the center of the i^{th} object and the j^{th} observation point, θ_{ij} is the angle between $\overrightarrow{r_{ij}}$ and $\overrightarrow{B_0}$, χ_0 is the magnetic susceptibility of the medium, χ is the magnetic susceptibility of the objects and B_0 is the main magnetic field strength.

We define the set W, representing the set of water observation points, and the set F, representing the set of fat observation points. Observation points located inside a fat object belong to the set F; observation points located outside all fat objects belong to the set W. The total number of water observation points is defined as n_w, the total number of fat observation points is defined as n_f, hence $n_w + n_f = N$. The effective fat volume fraction in the VOI was then defined as $\zeta_{VOI} = n_f/N$; note that $\zeta_{VOI} \neq \zeta$. The frequency ω_j in the rotating frame, on-resonance with water at γB_0, at the j^{th} observation point depends on the total field shift induced by all objects and was defined as follows:

$$for\ j \in W\text{:}\quad \omega_j = \gamma \sum_{i=1}^{M} \delta B_{z,ij} \qquad \text{[5a]},$$

$$for\ j \in F\text{:}\quad \omega_j = \gamma \sum_{i=1}^{M} \delta B_{z,ij} + \gamma\, \Delta\delta_{wf} B_0 \qquad \text{[5b]},$$

where $\Delta\delta_{wf}$ is the chemical shift difference between water and fat. The distribution of observed frequencies $f_j = \omega_j/(2\pi)$ in [Hz] was used for analysis. The normalized complex time-signal of water $S_w(t)$, of fat $S_f(t)$ and of water and fat $S(t)$ were calculated as follows:

$$S_w(t) = \frac{1}{N}\sum_{j\in W}^{n_w} e^{-i\,\omega_j\, t} \qquad \text{[6a]},$$

$$S_f(t) = \frac{1}{N}\sum_{j\in F}^{n_f} e^{-i\,\omega_j\, t} \qquad \text{[6b]},$$

$$S(t) = S_w + S_f \qquad \text{[6c]}.$$

NUMERICAL SIMULATIONS

To simulate the water and fat signals of a sub-voxel water-fat distribution, the numerical model was used with N = 10^6 observation points at B_0 = 1.5 T. For the magnetic susceptibility of the medium, χ_0 = 0 was used; for the magnetic susceptibility of the objects, the difference between water and fat was used: χ = χ_{fat} -χ_{water} = 1.26 ppm (85,136). The commonly used chemical shift difference between water and fat of $\Delta\delta_{wf}$ = δ_f - δ_w = -3.4 ppm (108,109) at 37°C was used, corresponding with a frequency difference of -217 Hz at 1.5 T.

The cubic observation VOI was defined to be smaller than the spherical medium: the lengths of the cube edges were equal to the radius of the water sphere R. The size of the objects was chosen such that the volume of one object is 0.01% of the VOI and simulations were performed for four fat volume fractions: ζ = 0.05, 0.10, 0.15 and 0.20. In their derivation, Yablonskiy and Haacke (127) assumed that the system was a homogeneous distribution. To investigate the influence of microscopic heterogeneities, the simulations were repeated ten times where the objects and observation points were reassigned random positions for each repetition. For signal characterization, the averaged signal of the repeated simulations was used.

Each observed frequency distribution was sampled with 2048 equally spaced points and a spectral bandwidth of 1 kHz. To characterize the peak dispersion of both water and fat, the full width at half maximum (FWHM) of the observed peaks were calculated. The complex time-signal was sampled in the time range of 0 to 256 ms, using 256 time points with a sampling time of 1 ms. The complex time-signals were used for comparison with the theoretical signal description (127). For the magnitude, the whole time range was considered for the analysis; for the phase, the time-evolution was considered for the analysis up to the time point at which the magnitude signal was less than 1% of the initial total signal of water and fat.

CHARACTERIZATION OF THE COMPLEX TIME-SIGNAL OF FAT

Similarly to water, the complex time-signal of fat was expected to show quadratic exponential behavior (Eq. [3a]) at the short-time scale, 0 ms to τ_f,

and shifted mono-exponential behavior (Eq. [3b]) at the long-time scale, τ_f to 256 ms.

To find τ_f, Eq.[3a] and Eq.[3b] were fitted to the magnitude of the fat signal in the corresponding time scales for a range of separation time points τ. For the fit of Eq.[3], $\delta\omega$, t_s and $R2'$ were used as fit parameters. For each τ, the residual sum of squares (RSS) was determined for the fits in the two time scales and summed. The τ range used was 10 ms to 246 ms, so that at least 10 data points were available per fit. The τ at which the summed RSS value was smallest was then defined as τ_f. The values found for the fit parameters $\delta\omega$, t_s and $R2'$ resulting from the fit procedure using τ_f where then defined as the effective characteristic frequency $\delta\omega_f$, the time shift $t_{s,f}$ and is the relaxation rate of the susceptibility-induced fat signal decay $R2'_f$.

The phase evolution of the fat signal was fitted with the following linear approximation:

$$for\ t \leq \tau_f: \quad \varphi(t) = -\left(\Delta\omega_{f,short} \cdot t\right) \qquad [7a],$$

$$for\ t \geq \tau_f: \quad \varphi(t) = -\left(\Delta\omega_{f,long} \cdot \left(t - t_{s,f}\right)\right) \qquad [7b],$$

where $\Delta\omega_{f,short}$ and $\Delta\omega_{f,long}$ are the frequency offsets in the short and long-time scale respectively. An iterative non-linear least-squares method was used for all fitting procedures, which were performed in Matlab (2013b, Mathworks, Natick, MA).

IMPLICATIONS FOR FAT-REFERENCED MRT

Using the average of the τ_f values found for all ζ used, $\bar{\tau_f}$, three time ranges can be defined: short-short regime = $[0, \tau_w]$ where both water and fat are in their short time scale; long-short regime = $[\tau_w, \bar{\tau_f}]$ where water is in its short time scale and fat in its long-time scale; long-long regime = $[\bar{\tau_f}, \infty)$ where both water and fat are in their long-time scale.

The implications of sampling in these time ranges were investigated for the fat-referenced multi-gradient echo-based (MGE) MRT method (29). With this method, temperatures in aqueous tissue can be calculated from the frequency difference between water and fat. The frequency difference can be

found by fitting two mono-exponentials with a frequency difference (29) to the magnitude time-signal acquired with an MGE MR sequence. To simulate such an acquisition, the magnitude of the simulated complex time-signal was sampled at 32 echo times with an echo spacing ΔTE of 1 ms. For signal sampling without delay, TE_0 = 1 ms was used and the corresponding last echo time TE_{last} = 32 ms. For delayed sampling, TE_0 = 5 to 60 ms with increments of 5 ms was used, with TE_{last} ranging from 36 ms to 91 ms. The resulting simulated MGE signals were fitted, using an iterative non-linear least-squares method (Matlab 2013b, Mathworks, Natick, MA). This was done for all repeated simulations. The errors in the extracted frequency difference (Δf) and the corresponding temperature were compared for the different sampling delays.

RESULTS

Numerical simulations were performed for fat volume fractions ζ = 0.05, 0.10, 0.15, and 0.20, which resulted in M = 2127, 4253, 6380, and 8507 fat objects. The average (±standard deviation) fat volume fractions in the VOI were ζ_{VOI} = 0.054 (±0.001), 0.107 (±0.002), 0.160 (±0.002), and 0.211 (±0.002).

OBSERVED FREQUENCY DISTRIBUTION

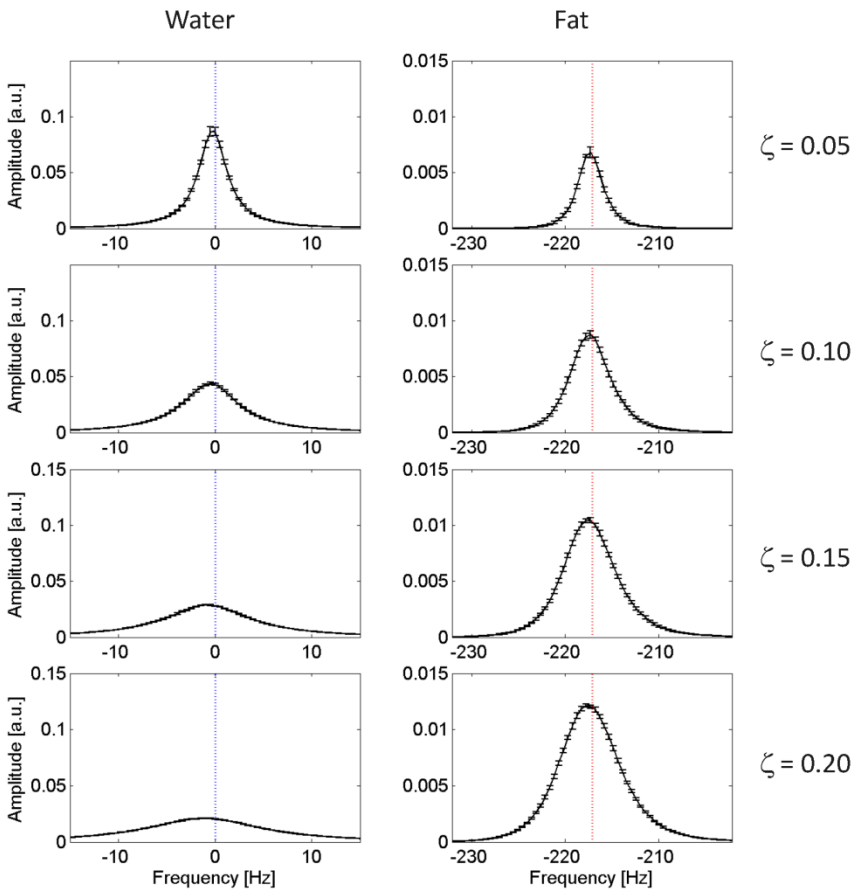

Figure 2. Observed frequency distributions of water and fat for all ζ values used in the simulations (rows). The error bars indicate the standard deviation over the repeated simulations; the vertical lines indicate the frequencies of water and fat without field shift effects.

The observed frequency distributions of the simulations are shown in Figure 2. The dispersion of the observed frequencies increased with increasing volume fraction and was stronger for water. This can be seen more clearly from the full width at half maximum (FWHM) values of the observed frequency distributions, plotted in Figure 3.

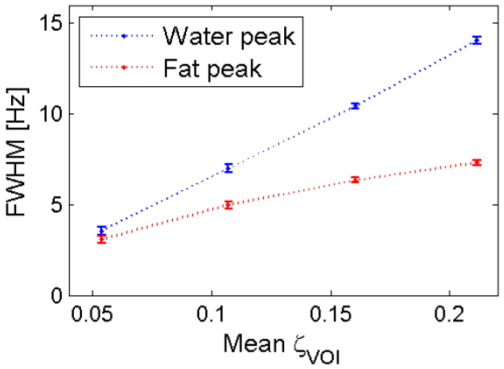

Figure 3. Full width at half maximum (FWHM) values of the observed frequency distributions of water and fat; the error bars indicate the standard deviation over the repeated simulations.

COMPLEX TIME-SIGNAL

The magnitude time-signals are plotted in Figure 4. The water magnitude signals correspond with the theoretical signal decay curves described by Yablonskiy and Haacke (127) and faster signal decay can be observed for larger ζ. Similarly, a short- and a long-time scale regime were observed in the behavior of fat magnitude signals. The error bars show only little variation in the magnitude signal between the repeated simulations. In the phase signal, the variations between the repeated simulations increased with increasing time for both water and fat (Fig.5). The water phase evolutions started from the time shift $t_{s,w}$ = 4.9 ms on for all ζ values. For ζ = 0.05 and ζ = 0.10, the water phase evolutions showed good correspondence with the theoretical curve up to about 130 ms, after which non-linear behavior was observed. For ζ = 0.15 and ζ = 0.20, the phase evolutions showed non-linear behavior from the time shift $t_{s,w}$ = 4.9 ms on. For fat, the phase evolutions started from t = 0 on for all ζ values.

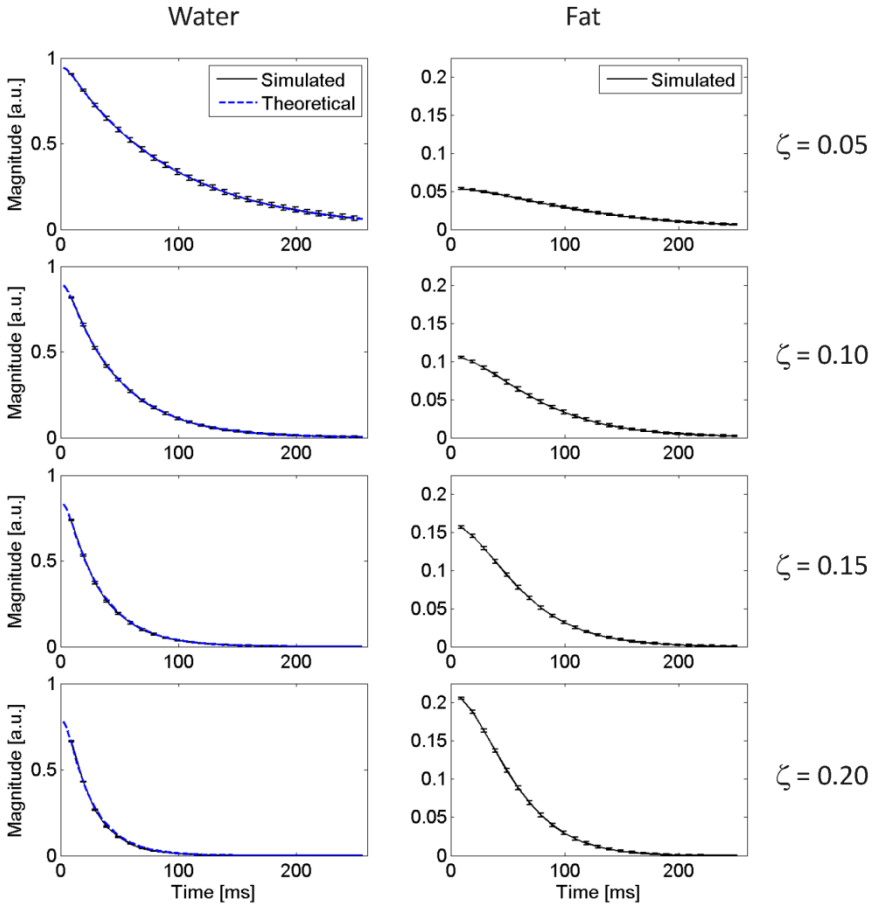

Figure 4. Magnitude time-signals of water and fat, plotted for all ζ values used in the simulations (rows). The error bars indicate the standard deviation over the repeated simulations. For water, the corresponding theoretical curves as described by Yablonskiy and Haacke are also plotted (blue dashed line).

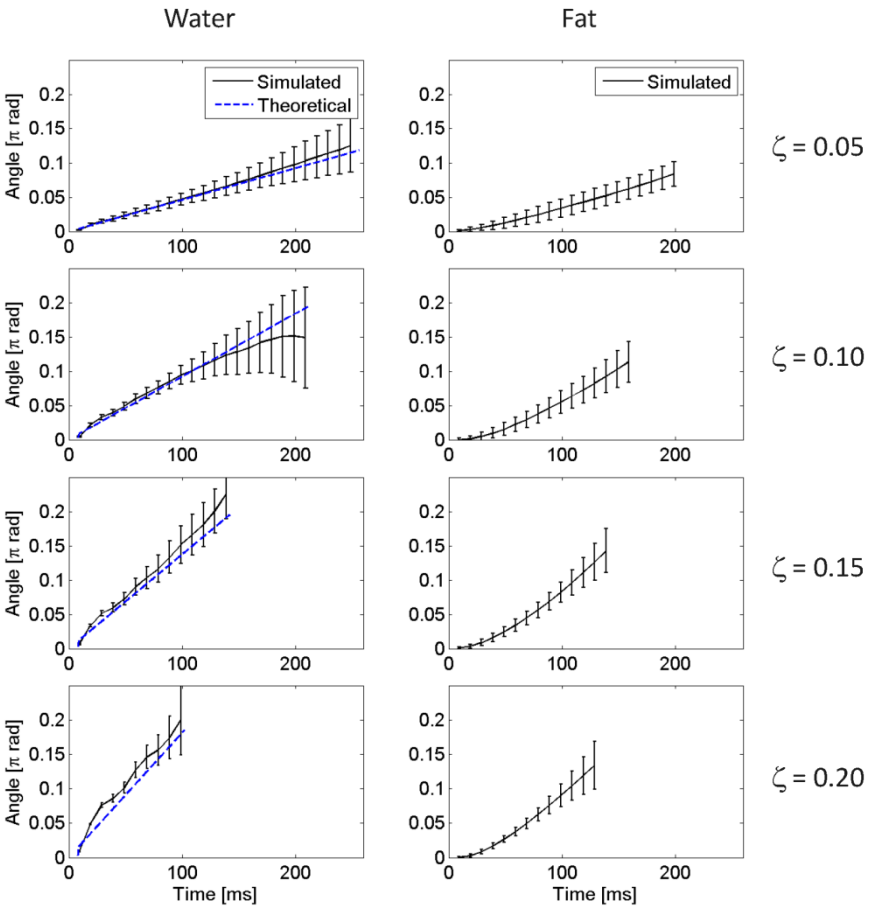

Figure 5. Phase-evolutions of the water and fat signals, plotted for all ζ values used in the simulations (rows). The error bars indicate the standard deviation over the repeated simulations. For water, the corresponding theoretical curves as described by Yablonskiy and Haacke are also plotted (blue dashed line). For ζ = 0.05, 0.10, 0.15, and 0.20, the argument time-evolutions are plotted up to 255, 210, 141, and 101 ms respectively for water and 202, 163, 144, and 133 ms respectively for fat.

CHARACTERIZATION OF THE COMPLEX TIME-SIGNAL OF FAT

The RSS of the fits of Eq.[3a] and Eq.[3b] to the magnitude fat signals are plotted for the range of τ in Figure 6a; the summed RSS of both fits is also plotted. The τ values at which the summed RSS values were at their minimum are indicated by vertical dashed gray lines and were defined as τ_f. The values found for τ_f decreased with increasing ζ. The average $\overline{\tau_f}$ (±standard deviation) was 54.8 (±8.1) ms, a factor 6 larger than τ_w = 8.9 ms (Table 1).

The results of the fit of Eq.[3a] to the simulated magnitude fat signals for $t \leq \tau_f$ and of Eq.[3b] to the magnitude fat signals for $t \geq \tau_f$ are shown in Figure 6b. The plots show that the simulated magnitude fat signals follow a quadratic exponential function up to τ_f, and from τ_f on a shifted mono-exponential function. The results of the fit of Eq.[7a] to the phase evolutions for $t \leq \tau_f$ and of Eq.[7b] to the phase evolutions for $t \geq \tau_f$ are shown in Figure 6c. The plots show that the phase evolution in both the short- and long-time scales can be approximated, but not perfectly, by linear functions.
All parameter values resulting from the fitting procedures are summarized in Table 1. With increasing ζ, the effective characteristic frequency $\delta\omega_f$ and the time shift $t_{s,f}$ decreased, while the relaxation rate of the signal decay $R2'_f$ and the frequency offsets $\Delta\omega_{f,short}$ and $\Delta\omega_{f,long}$ increased. The average $\delta\omega_f$ over all ζ, $\overline{\delta\omega_f}$ (±standard deviation), was 60.6 (±1.7) rad/s; a factor 3 smaller than $\delta\omega_w$. The average $t_{s,f}$ over all ζ, $\overline{t_{s,f}}$ (±standard deviation), was 30.4 (±3.9) ms; a factor 6 larger than $t_{s,w}$.

IMPLICATIONS FOR FAT-REFERENCED MRT

By taking $\overline{\tau_f}$ as the estimated separation time point between the two regimes for fat, the estimated time ranges for the combined water and fat signals were: short-short regime = [0,8.9] ms, long-short regime = [8.9,55] ms and long-long regime = [55,256] ms.

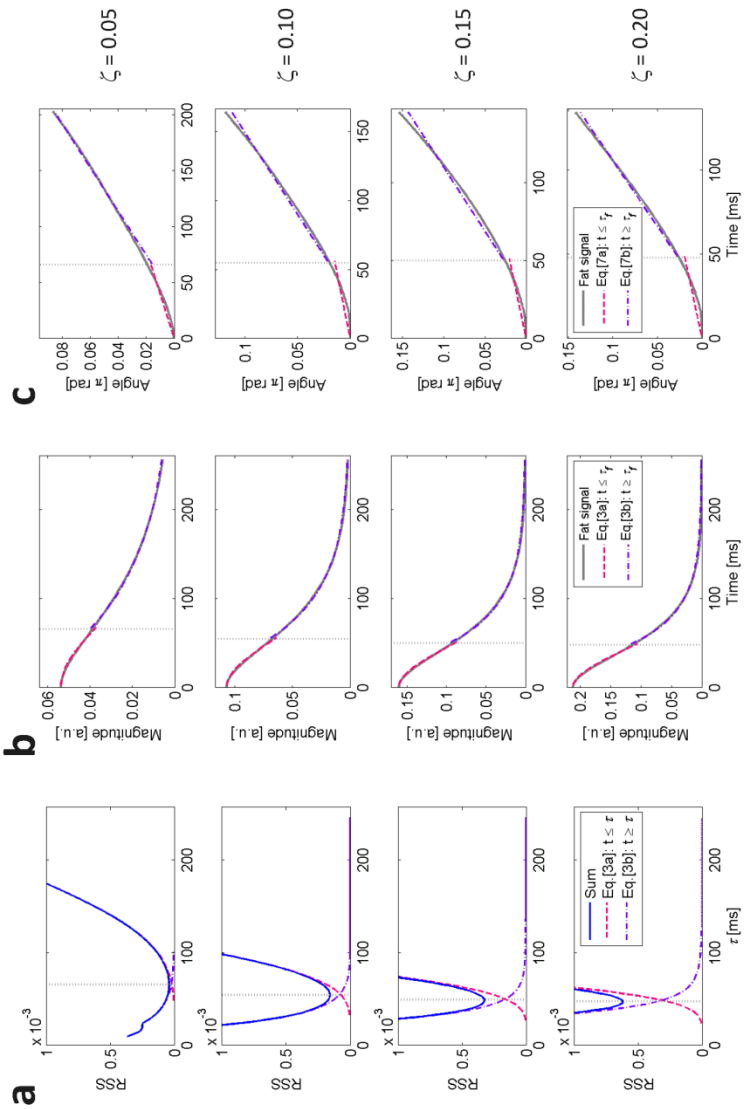

Figure 6. In (a), the residual sum of squares (RSS) of the fits in two regimes separated by τ are plotted for a range of τ, for all ζ values used in the simulations (rows). The summed RSS is plotted in blue; the time points at which the summed RSS is at its minimum are indicated by vertical dashed gray lines and were defined as τ_f. The fit to the fat signals from 0 ms to τ_f and to the fat signals from τ_f to 256 ms are shown in (b) for the magnitude and for the argument in (c), where vertical dashed gray lines indicate τ_f.

Figure 7 shows the errors in the Δf extracted using the MGE MRT method and the corresponding temperature errors. The plots all show the same behavior: the error first decreased to a local minimum, then increased slightly, followed by a decrease. The variations between the repeated simulations were larger for larger ζ and increased with increasing TE_0. For TE_0 = 1 ms, without delayed sampling, the average (± standard deviation) temperature errors found for ζ = 0.05, 0.10, 0.15, and 0.20 were 1.8 (±0.1)°C, 2.3 (±0.1)°C, 2.7 (±0.2)°C, and 3.3 (±0.1)°C. The smallest average (± standard deviation) temperature errors found in the local minima were -0.01 (±0.15)°C, 0.18 (±0.14)°C, 0.23 (±0.21)°C, and 0.29 (±0.25)°C for ζ = 0.05, 0.10, 0.15, and 0.20, respectively. These minimum errors were found for TE_0 values of 15 ms, 20 ms, 25 ms, and 25 ms; the corresponding TE_{last} were 47 ms, 52 ms, 57 ms, and 57 ms. These sampling time ranges were almost completely within the long-short regime.

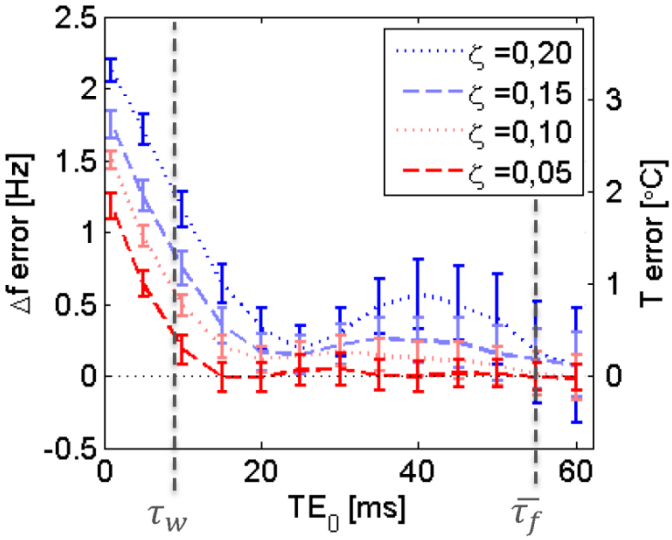

Figure 7. The errors in the frequency difference (Δf) extracted using the MGE MRT method are plotted for a range of echo times (TE0). The additional y-axis on the right-side of the plot indicates the corresponding temperature errors. The vertical lines indicate τ_w and $\bar{\tau}_f$, the error bars indicate the standard deviation over the repeated simulations.

DISCUSSION

The MR signal behavior of both water and fat was investigated for a sub-voxel, macroscopically homogeneous system of perturbing fat spheres embedded in water. Yablonskiy and Haacke (127) have analytically described the signal behavior of such systems of randomly distributed perturbers in a medium. Different from those systems, in the water-fat system studied in this work both the medium and the perturbers gave MR signal. And since water and fat have different resonance frequencies, the susceptibility-induced field shift effects could be considered separately for each resonance.

From the numerical simulations, we found dispersed water and peaks in the observed frequency distribution. For the range of fat volume fractions ζ used in this study, larger ζ induced more inhomogeneities in the magnetic field and thus the nuclear frequencies were more dispersed. From the FWHM measurements, it could be seen that the fat peak was less dispersed than the water peak. This suggests that fat was less affected by the local susceptibility-induced field shifts. This is due to the geometrical restrictions of the fat observation points, which are all located inside the spherical fat objects in the water sphere.

The simulated water magnitude signal showed good correspondence with the theoretical curve, describing different behavior in the short-time scale and long-time scale. The average fat magnitude signal showed quadratic exponential behavior in the short-time scale and shifted mono-exponential behavior in the long-time scale. The time point separating the two regimes of the fat signal behavior, τ_f, was determined by minimizing the summed RSS of the short- and long-time scale fits. We found that τ_f was not fixed but decreased with increasing ζ and that $\overline{\tau_f}$ was a factor 6 larger than τ_w. The short- and long-time scales for fat were defined accordingly and the magnitude signal could be well-fitted with Eq.[3a] for the short- and Eq.[3b] for the long-time scale. The parameter $\delta\omega_f$ could be interpreted as the characteristic frequency of the induced magnetic field by a fat sphere at a certain distance. The empirical values found by fitting include the effects of the underlying geometric restriction; observation points in other fat spheres are less likely to be as close to the field-inducing fat sphere as observation points in water. The average over all ζ used in this study, $\overline{\delta\omega_f}$, was a factor 3

smaller than $\delta\omega_w$. This implies that the fat signal experiences weaker field shift effects than the water signal. The susceptibility-induced relaxation rate of the fat signal decay $R2'_f$ increased with ζ and was lower than that of water, which also implies weaker field shift effects for fat. The time shift $t_{s,f}$ for fat decreased with increasing ζ and $\overline{t_{s,f}}$ was a factor 6 larger than the time shift $t_{s,w}$ for water; the same factor as for the separation values $\overline{\tau_f}$ and τ_w.

While only little variation in the magnitude signal was observed between the repeated simulations, large variations were observed in the phase evolution. This indicates that the microscopic heterogeneity, that is, the geometrical arrangement of the fat spheres in water, influences the phase of both the water and the fat signals. The linear approximation of the phase evolution described by Yablonskiy and Haacke (127) was based on the assumption of a small perturber concentration limit, ζ << 1. The fractions ζ = 0.15 and 0.20 do not satisfy this limit and may therefore not be described by the linear approximation. The fat phase evolution in both the short- and long-time scales could be approximated but not perfectly described by the linear functions described in Eq.[7]. This suggests that, different from water, the complex fat time-signal had an oscillating part for both regimes.

We estimated the time ranges in which both the water and the fat signal were in either the short-time or the long-time scale. We showed that sampling the signal in both time scales influences the performance of the fat-referenced MGE-based MRT method (29). The largest errors were found for signals sampled with no or little delay, where the sampling time range covers both the short-short regime and the long-short regime. For $TE_0 \geq \overline{\tau_f}$, the signals would be completely sampled in the long-long regime. In this regime, both the water signal and the fat signal show mono-exponential behavior, which implies that theoretically the error should decrease. However, the later echoes will be sampled at even longer echo times and very little signal will be left, which impedes the extraction of reliable frequency differences. Unexpectedly, a local minimum in the errors was observed around TE_0 = 20 ms, where the signal was almost completely sampled in long-short regime. Even though the fat signal is in the short-time scale, following a quadratic exponential, the errors were minimal (1.5 HZ; 0.2°C). The errors increase for smaller TE_0 within the long-short regime, which can be explained by the fact that a quadratic exponential deviates the most

from a mono-exponential in the early time points (Fig.6b). For TE_0 > 20 ms, the fat signal will be partly in the short-time scale and partly in the long-time scale, which explains the increasing error with TE_0. These observations show that the two regime signal behavior of water and fat influences the accuracy of fat-referenced MGE MRT. Sampling the signal such that both water and fat are either in the short or in the long regime could reduce the errors. These errors are induced by spatial variations in magnetic susceptibility, caused by the spatial water-fat distribution, and are therefore systematic. These errors can be cancelled out when calculating relative temperature changes from the absolute temperatures measured with MGE MRT (135), making the relative MGE MRT insensitive to these susceptibility effects.

The numerical simulations performed in this study were based on randomly distributed fat spheres in a water medium; a theoretical approximation of water-fat emulsions, such as mayonnaise. The typical size of fat droplets in mayonnaise ranges from 1-100 μm (138), which is much larger than the diffusion boundary radius of 10 nm (128). Therefore, the system may be expected to be in the static dephasing regime. Although fat droplets in water-fat emulsions have variable sizes, the numerical simulations in this study were performed for a fixed object size. Yablonskiy and Haacke (127) showed that their theoretical approximation of the water signal behavior applies for variable object radii and we expect the same for the fat signal behavior.

By performing numerical simulations, the effects on the signal behavior purely by susceptibility-induced field shifts could be investigated. The fat signal could be well characterized using the theoretical description of Yablonskiy and Haacke (127), showing short- and long-time scale behavior. In practice, this susceptibility-induced short- and long-time scale signal decay will occur in addition to the signal decay induced by the intrinsic relaxation rate. This may even further complicate fat-referenced MRT methods that assume mono-exponentials or its equivalent, Lorentzian peaks, in the frequency domain (28,29). Our findings encourage further research on the susceptibility-induced effects on water and fat signals, in macroscopically homogeneous and heterogeneous water-fat distributions.

CONCLUSION

We have shown with numerical simulations of randomly distributed fat spheres embedded in water, that both the water signal and the fat signal of such a macroscopically homogeneous water-fat system show combined quadratic exponential and shifted mono-exponential behaviors. Because of geometrical restrictions, the fat signal is less affected by the susceptibility-induced field shifts, whence the estimated separation time point of the two regimes is much later than for water ($\overline{\tau_f}$ = 55 ms versus τ_w = 8.9 ms). We have demonstrated that the systematic errors in the MGE MRT method due to the field effects can be reduced from 2°C to 0.2°C, by delaying the signal sampling so that both the water signal and the fat signal are either in the short or in the long regime.

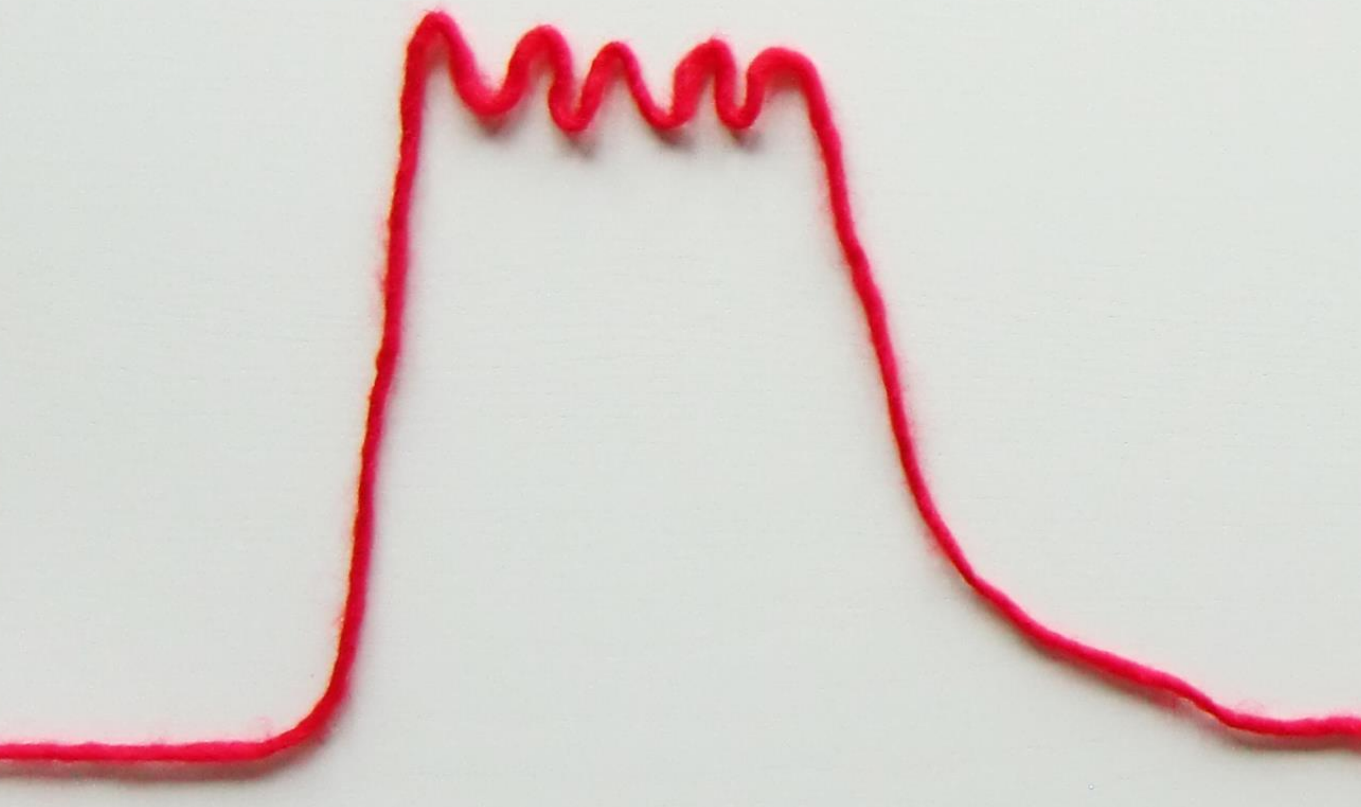

"If an experiment works, something has gone wrong"

– *Murphy's Law*

Chapter 5

DCE-MRI and IVIM-MRI of rabbit VX2 tumors treated with MR-HIFU induced hyperthermia

Submitted for publication in a revised version

INTRODUCTION

Information about tumor physiology is valuable since it is an important determinant of treatment outcomes (139,140). Physiological responses of tumors to hyperthermia have been extensively investigated in rodent models using invasive measurement methods (17,18,141-145). Tumors are more sensitive to heating and stasis of the blood flow occurs at lower hyperthermic temperatures as compared with normal tissue (17,18). Changes in regional blood flow and permeability after hyperthermia were reported to show both inter- and intra-tumoral variations (18,145). The underlying mechanisms are complex and depend on several factors, e.g. the chemical microenvironment and tumor architecture (18), which makes it difficult to predict tumor responses to hyperthermia. Noninvasive methods to map physiological changes would therefore be useful for investigating tumor responses to hyperthermia (146,147).

Dynamic contrast-enhanced (DCE) magnetic resonance imaging (MRI) is a method widely used to map perfusion and permeability parameters (148,149). Dynamic T_1-weighted scans are acquired before, during and after the injection of a paramagnetic contrast agent bolus. Concentration-time curves are derived from the dynamic T_1 maps and perfusion parameters can be extracted by fitting a physiological model, such as the Tofts model (150,151). Many studies have reported on the potential of DCE-MRI as a prediction tool for treatment response of tumors to radiotherapy (152,153), neo-adjuvant chemotherapy (154-156) and neo-adjuvant chemoradiation (157-159).

Intra-voxel incoherent motion (IVIM) MRI is a method that allows measurements of perfusion-related parameters from diffusion-weighted MR data. The non-Brownian motion of blood flowing through pseudo randomly organized capillary networks is considered as incoherent motion. This generates a "pseudo diffusion" effect and contributes to the diffusion-weighted MR signal. By using a bi-exponential description of the MR signal, parameters related to the vascularity can be extracted (160). Although these parameters should be interpreted carefully (161,162), the vascular contribution to measured IVIM parameters has recently been verified in healthy volunteers (163). Recent studies showed promising results using IVIM

for the characterization of various diseases of different organs, for example cirrhotic liver (164), pancreatic carcinoma (165), locally advanced breast cancer (166), salivary gland tumors (167), brain pathologies (168) and renal tumors (169).

In this study we investigated the potential of DCE- and IVIM-MRI to detect changes induced by hyperthermia in rabbits with Vx2 tumors, using the Extended Tofts DCE-MRI model and a Bayesian approach for IVIM analysis. To this end, a clinical MR-guided high intensity focused ultrasound (MR-HIFU) system was used, which allows of noninvasive local hyperthermia in small animals (47,91,170-172).

MATERIALS AND METHODS

ANIMAL HANDLING AND VX2 TUMORS

All experiments were approved by the University Animal Experiments Committee and were performed in agreement with The Netherlands Experiments on Animals Act (1977) and the European Convention guidelines (86/609/EC). Five female New Zealand White rabbits (2.5–3.5 kg, Charles River, France) were housed in pairs and were provided with food and *ad libitum* water. Vx2 tumor pieces were retrieved from donor rabbits and implanted intramuscularly in the left hind limb. The tumors grew to a volume of 10 cm^3 in about 3 weeks, after which the imaging experiment was performed.

The rabbits were initially anaesthetized with a subcutaneous injection of dexmedetomidine (0.125 mg/kg, Dexdomitor, Jansen Pharmaceutica N.V., Beerse, The Netherlands) and ketamine (15 mg/kg, Narketan 10, Vétoquinol S.A., Lure Cedex, France). The tumor-bearing hind limb was shaved, depilated and covered with ultrasound gel for acoustic coupling. To prevent undesired leg movement during HIFU exposure, a sciatic nerve block was performed (bupivacaine 2 mg/kg). Then, a fluoroptic temperature probe (Luxtron, Santa Clara, CA) was placed in the muscle tissue adjacent to the tumor to allow measurements of the baseline temperature as is used for the relative MR thermometry.

A catheter (Abbocath®-T I.V. Catheter 22 g × 1.25'', Hospira Inc., Lake Forest, IL) was placed in the marginal ear vein and was connected to a Luer-

lock 3-way valve, providing two inputs. One input was used for the intravenous maintenance anesthesia (one third of the initial dose per hour), which was provided using a pressure pump system up to 5 hours after initiation of anesthesia. The other input was available for intravenous injection of the MR contrast agent gadobutrol (GadoVist, 0.1 mmol/kg, Gadovist, Bayer Pharma). After the experiment, the rabbits were terminated with an overdose of sodium pentobarbital injected intravenously.

EXPERIMENTAL SET-UP

A clinical MR-HIFU therapy system was used (Sonalleve V2, Philips Healthcare, Vantaa, Finland) integrated into a clinical 1.5T MRI scanner (Achieva, Philips Healthcare, Best, The Netherlands). An in-house developed animal holder as previously described by Wijlemans, et al. (173) was used, which consisted of an open polymethylmethacrylate tank with an acoustic window in the bottom. A schematic overview of the setup is shown in Figure 1a. The tank was filled with heated water up to the tumor-bearing leg, to enable acoustic coupling and to achieve a baseline temperature similar to human body temperature (37°C). A heating blanket was placed on top of the rabbit keep the baseline temperature stable.

MR-HIFU INDUCED MILD HYPERTHERMIA

Mild hyperthermia (40°C to 42°C) was induced locally in all five rabbits using the clinical MR-HIFU therapy system described earlier. Sonications were performed with 60W acoustic power at an operating frequency of 1.2 MHz and the acoustical energy was delivered along concentric circular sub-trajectories of 4-mm and 8-mm diameter by electronically steering the focus, the so-called HIFU cell (84). Mild hyperthermia was achieved by the binary feedback-loop described by Partanen, et al. (5), which uses the temperature measurements provided by the MR thermometry. After initial heating to mild hyperthermic temperatures, hyperthermia was maintained by re-sonicating the sub-trajectories using a binary feedback-loop. In this study, the binary feedback-loop was slightly adapted: re-sonication was done with 80% of the initial acoustical power instead of 50%.

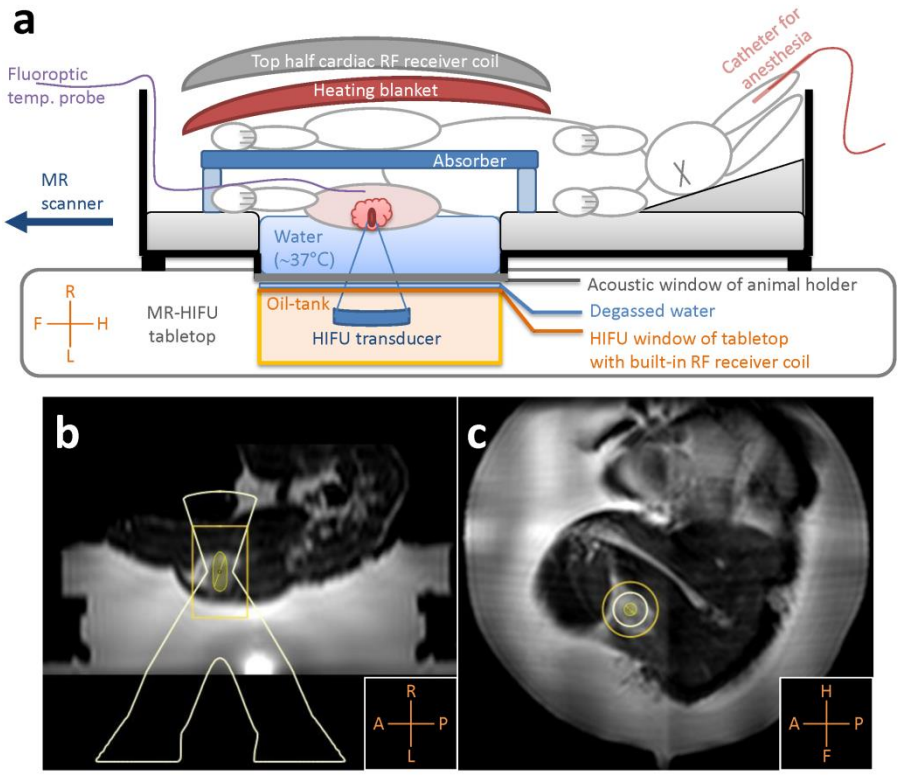

Figure 1. A schematic overview of the experimental setup is shown in (a). The animal holder was placed with its acoustic window above the HIFU window; degassed water was used for acoustic coupling. The shaved tumor bearing leg was positioned above the acoustic window and a fluoroptic temperature probe was inserted in the tumor bearing leg, in the far-field of the HIFU beam. The tank was filled with warm water (~37°C) up to the tumor bearing leg and an absorber was placed between the legs. On top of the rabbit, a heating blanket and the top half of a cardiac RF receiver coil was placed. In (b) and (c), examples of the treatment planning are shown on reconstructed sagittal and coronal images of the T_2-weighted 3D turbo spin-echo acquisition.

The hyperthermia protocol consisted of three hyperthermia blocks of 10 minutes, separated by periods of cooling. Each subsequent hyperthermia sonication started when the temperature, measured by the fluoroptic temperature probe, had decreased to the baseline temperature measured prior to heating. A hyperthermia block was considered unsuccessful and redone after cool down when the duration of the hyperthermia block was less than half of the intended duration, for example due to automatic abortion by the system upon detection of large motion.

The measured hyperthermic temperatures by MR thermometry were expressed by the measures T_{10}, T_{50}, T_{90}, which indicate the temperatures exceeded by 10%, 50% and 90% of the target region, respectively. These values were calculated over manually selected circular regions of interest (ROI) with a diameter of 10 mm at the heated area in each slice, slightly larger than the HIFU cell size. Temporal mean values were calculated for the entire hyperthermia duration, i.e. the time period between the start and end of the hyperthermia maintenance phase of the feedback algorithm of each block, for the sagittal slice and the central coronal slice.

MR IMAGING

A four-channel RF receiver coil integrated into the MR-HIFU tabletop was used, together with a flat sixteen-channel array coil, which was placed on top of the heating blanket (Figure 1a).

To plan the position of the HIFU focus, an anatomical T_2-weighted 3D turbo spin-echo sequence was used with the following scan parameter settings: echo time (TE) = 254 ms, repetition time (TR) = 1000 ms, flip angle (FA) = 90°, voxel size = 2×2×2 mm^3, field of view (FOV) = 250×250×126 mm^3, number of signal averages (NSA) = 2. Figure 1b and 1c show examples of treatment planning on reconstructed sagittal and coronal images.

The MR thermometry scan used a multi-slice gradient-echo planar imaging (EPI) pulse sequence with binomial water-selective RF excitation. One stack of 3 coronal slices and 1 sagittal slice were acquired, and a saturation slab was used to suppress signal from the water tank. The scan parameter settings were: TE = 20 ms, TR = 44 ms, FA = 20°, pixel size = 2.5×2.5 mm^2, slice thickness = 7 mm, FOV = 250×250 mm^2, NSA = 2, EPI factor = 11, dynamic scan duration = 3.9 s. Temperatures changes were

calculated on the fly using the proton resonance frequency shift method (25,26) and added to the baseline temperature measured with the fluoroptic probe in order to reconstruct temperature images.

The baseline T_1 map, required for DCE-MRI analyses, was obtained from variable flip angle (VFA) images acquired prior to contrast agent injection. The DCE-MR images and VFA images were acquired before and after hyperthermia. The DCE-MR images were acquired with a 3D spoiled gradient-echo dynamic key-hole sequence, using the last scan for the high spatial frequency data: TE = 1.4 ms, TR = 5 ms, FA = 15°, voxel size = 1.2×1.5×2 mm^3, FOV = 300×150×40 mm^2, NSA = 2, keyhole percentage = 25%, keyhole measurements = 2, dynamic reference scan duration = 13.1 s, dynamic keyhole scan duration = 3.3 s, total scan duration = 5 min, 47 s. For the VFA images, the DCE-MRI scan sequence was used without the dynamic settings and FA = 5°, 10° and 15°. MR contrast agent was injected between 15 s and 20 s after starting the dynamic DCE scan. The DCE-MRI scan was acquired on average 10 minutes (range: 6.5 to 17.5 minutes) after the end of hyperthermia.

For IVIM-MRI, multi-slice diffusion-weighted single-shot spin-echo EPI images were acquired with 10 b-values, before and after hyperthermia. The scan parameter settings were: TE = 67 ms, TR = 2500 ms, FA = 90°, pixel size = 2×2 mm^2, slice thickness = 3 mm, FOV = 140 x 179 mm^2, number of slices = 12, NSA = 6, b = 800, 600, 400, 200, 150, 100, 75, 50, 25, 0 s/mm^2. A frequency selective adiabatic inversion pulse was used for fat suppression, with a delay time of 90 ms. The IVIM-MRI scan was acquired on average 35 minutes (range: 26 to 43 minutes) after the end of hyperthermia.

TUMOR VOIS

For all datasets a 3D tumor volume of interest (VOI) was selected by manual delineation of the tumor region in each slice. The tumor VOIs were used to make overlay masks of the parameter maps over the magnitude images and for the comparison of the parameters before and after hyperthermia. In the DCE datasets, the delineation was performed after the bolus passage at the 20^{th} dynamic; in the IVIM datasets, the delineation was performed at b = 0 s/mm^2.

DCE DATA ANALYSIS

The DCE-MRI analysis was performed in Matlab (2013b, Mathworks, Natick, MA). First dynamic 3D concentration maps were reconstructed from the DCE data, using the T_1 baseline maps obtained from the VFA data (174). Second, arterial input functions (AIFs) were measured in the feeding artery of rabbit 5 in both the pre- and post-hyperthermia data. These representative concentration-time curves were parametrized using a gamma variate function (175). The blood plasma volume fraction v_p has been reported to be a crucial parameter for the assessment of tumor physiological response to hyperthermia and thus should be included in the analysis (146,147). Therefore, the Extended Tofts DCE model (150,176) was used:

$$C(t) = K^{trans} \int_0^t C_p(\tau)\, e^{k_{ep}(t-\tau)} d\tau + v_p C_p(t) \qquad [1],$$

where K^{trans} is the volume transfer constant between blood plasma and the extracellular extravascular space (EES), k_{ep} is the rate constant between EES and the blood plasma and $C_p(\tau)$ is the concentration-time curve in the arterial blood plasma, or the AIF. Eq.[1] was fitted voxel-wise to the dynamic concentration maps using an iterative nonlinear least-squares fit procedure, where the parametrized pre- and post-hyperthermia AIFs were used for the analysis of the pre- and post-hyperthermia data respectively. Maps were reconstructed of K^{trans}, k_{ep} and v_p.

IVIM DATA ANALYSIS

The IVIM-MRI analysis was performed using the data driven Bayesian modeling method described by Orton, et al. (177), which has no user-defined parameters and is therefore robust and reproducible (177). The method was implemented in Mathematica (7.0, Wolfram Research Inc., Champaign, IL) and the following bi-exponential model was used:

$$S(b) = S_0\left(f_p\, e^{-b \cdot D_p} + \left(1 - f_p\right) e^{-b \cdot D_t}\right) \qquad [2],$$

where D_t is the true diffusion, f_p is the perfusion fraction and D_p is the pseudo diffusion, induced by the vascular components. The Bayesian modeling method makes Gaussian approximations of the IVIM parameter

histograms, resulting from least-squares fitting of Eq.[2]. These approximations are used as prior distributions to push outlier estimates with high uncertainty towards the center of the histogram (177). To fill the prior distribution appropriately, the muscle surrounding the tumor was included and any water from the tank was excluded. Maps were reconstructed of D_t, f_p and D_p.

DETECTION OF CHANGES AFTER HYPERTHERMIA

While the mean of a VOI is an often used metric for the comparison of parameter values, histograms are less arbitrary and capture heterogeneity (140,146,169,178). Histograms were made for each DCE and IVIM parameter, with ranges of 0 to 5 for K^{trans} $[\mathrm{min}^{-1}]$ and k_{ep} $[\mathrm{min}^{-1}]$, 0 to 1 for v_p [fraction] and f_p [fraction], 0 to 3 for D_t $[10^{-3}\mathrm{mm}^2/\mathrm{s}]$, and 0 to 30 for D_p $[10^{-3}\mathrm{mm}^2/\mathrm{s}]$. All data were distributed in 100 bins and the bin heights were expressed in percentage of the tumor VOI volume.

For quantitative comparison, we determined the median values of all values inside the mentioned ranges (excluding the outliers). The parameter distributions were expected to be non-normal owing to tumor heterogeneity, and the pre- and post-hyperthermia data were unpaired since the tumor VOIs were delineated individually. Therefore, to test if pre- and post-hyperthermia median values were significantly different, the Mann Whitney U test was used. Statistical tests were performed in Matlab (2013b, Mathworks, Natick, MA) and a p-value of less than 0.001 was considered indicative of a statistically significant difference.

Two-dimensional cross-correlation histograms provide insight in the inter-relationships between parameters (166) and were made for the following combinations: $v_p \times K^{trans}$, $k_{ep} \times K^{trans}$, $v_p \times k_{ep}$, $f_p \times D_t$, $D_p \times D_t$ and $f_p \times D_p$. The same number of bins and ranges were used as for the individual parameter histograms and the intensities were expressed in percentage of the tumor VOI volume.

To ensure that observed changes in parameter values were induced by hyperthermia, data reproducibility was tested. The IVIM scan of rabbit 1 after hyperthermia was repeated and the results were compared. Since the DCE scans require the use of a contrast agent, a similar reproducibility test was deemed not feasible for DCE-MRI.

RESULTS

The T2w MR images acquired during the planning phase showed that all rabbits had one tumor except for rabbit 4, which had three small contiguous tumors. Rabbit 2 had a large necrotic core in the tumor and died during the last few minutes of the hyperthermia treatment.

MR-HIFU INDUCED MILD HYPERTHERMIA

Three 10-minute blocks of mild hyperthermia (40°C to 42°C) were successfully achieved in all five rabbits using MR-HIFU. Figures 2a and 2b show examples of magnitude and temperature images of the MR thermometry sequence; examples of the temporal profiles of T_{10}, T_{50} and T_{90} of the corresponding ROIs (circles) are shown in Figure 2c. The mean values of T_{10}, T_{50} and T_{90} over the entire hyperthermia duration are shown in Table 1 and plotted in Figure 2d for each rabbit. All T_{50}values were within the desired hyperthermic temperature range of 40°C to 42°C. In the coronal slice of rabbit 3, the mean T_{10} was higher than 42°C and the mean T_{50} was higher than the other rabbits.

REPRODUCIBILITY

In Figure 3, the results of the repeated IVIM scans of rabbit 1, acquired post hyperthermia, are shown. The parameter maps of the central slice through the tumor (Fig.3a) look similar, as well as the individual parameter histograms (Fig.3b) and the cross-correlation histograms (Fig.3c), except for some minor differences in D_t. Table 1 shows that the median D_t values showed a small but statistically significant difference of 0.14×10^{-3}mm^2/s ($p<0.001$), while no significant difference was found between the median f_p ($p=0.14$) and D_p values ($p=0.09$).

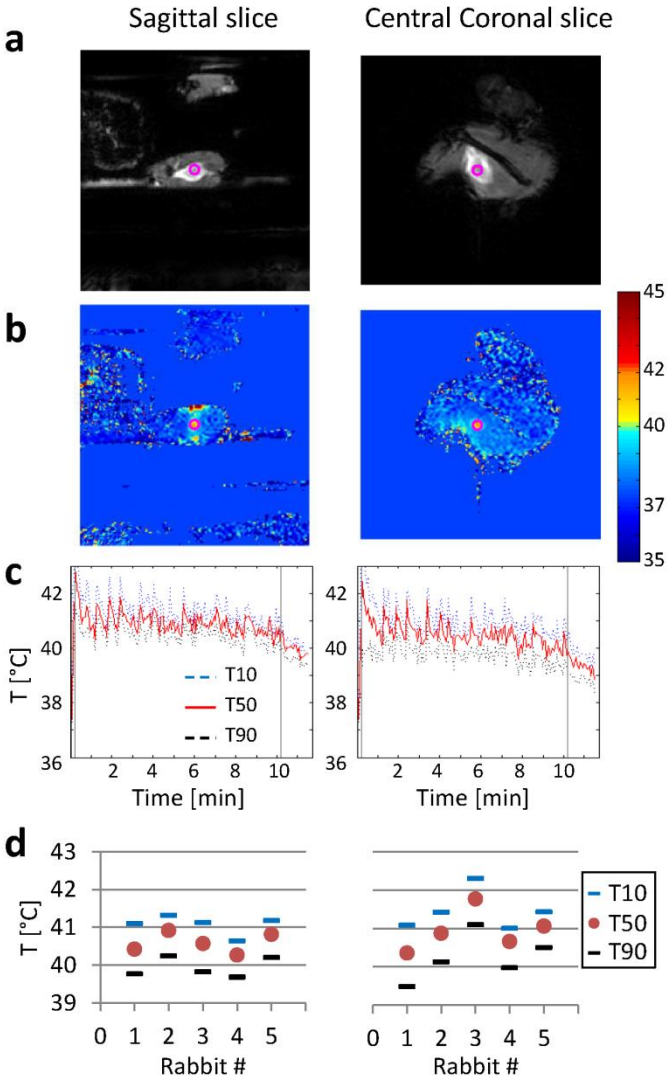

Figure 2. Examples of magnitude images (a) and temperature images (b) of the MR thermometry sequence and T_{10}, T_{50} and T_{90} profiles over time (c) (rabbit 2, first hyperthermia block). In (c), the vertical lines indicate the start and end of the hyperthermia maintenance phase of the feedback algorithm. The ROIs used for the T_{10}, T_{50} and T_{90} calculation are indicated by the pink circles in the images in (a) and (b). In (d), the temporal mean values of T_{10}, T_{50} and T_{90} over the entire hyperthermia duration are shown per rabbit.

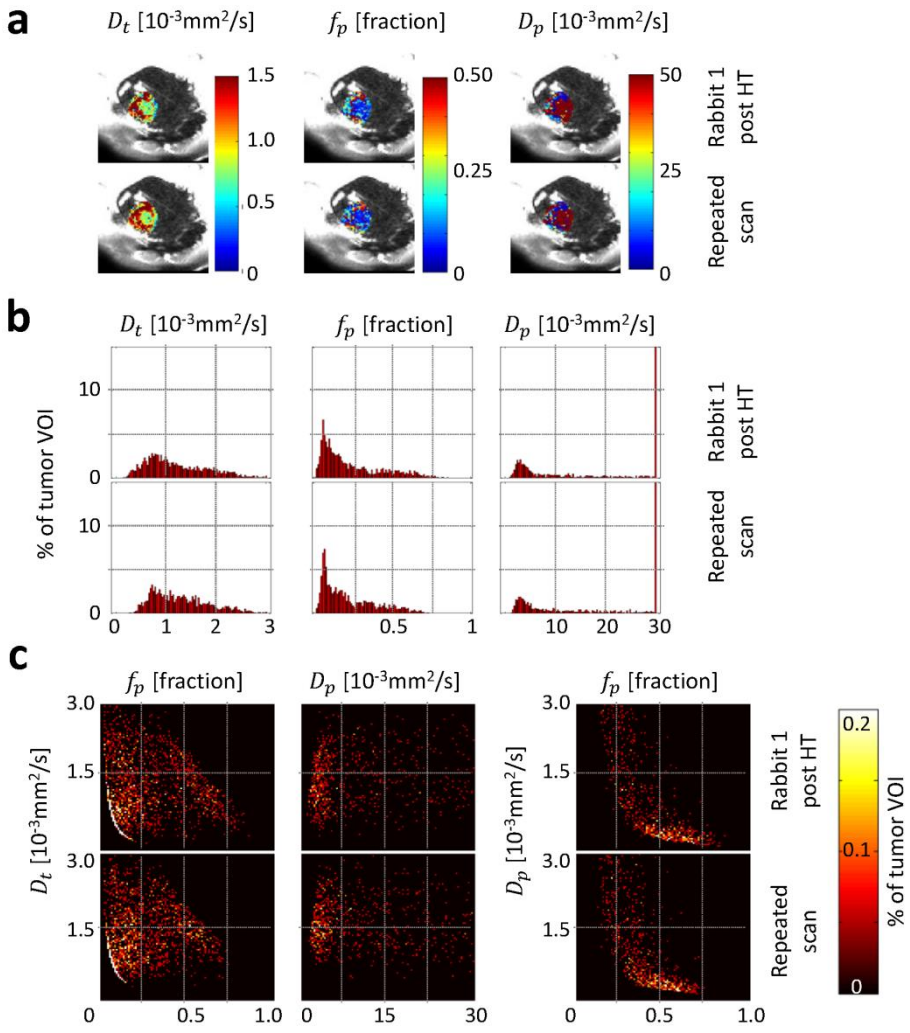

Figure 3. Results of the repeated IVIM scans acquired in rabbit 1 after hyperthermia. The parameter maps of the central slice through the tumor are shown in (a), the individual parameter histograms in (b) and the two-dimensional cross-correlation histograms in (c). The parameter maps in frame (a) were masked using the tumor VOI and are shown as an overlay over the corresponding magnitude image (b = 0 s/mm^2).

Table 1. Temporal mean and standard deviation (SD) of T_{50}, T_{90} and T_{10}, averaged over the three hyperthermia blocks

Rabbit	Central coronal slice			Sagittal slice		
	T_{50} (°C)	T_{90} (°C)	T_{10} (°C)	T_{50} (°C)	T_{90} (°C)	T_{10} (°C)
1	40.4	39.5	41.1	40.4	39.8	41.1
2	40.9	40.1	41.4	40.9	40.2	41.3
3	41.8	41.1	42.3	40.6	39.8	41.1
4	40.7	40.0	41.0	40.3	39.7	40.6
5	41.1	40.5	41.4	40.8	40.2	41.2
Mean (SD)	40.9 (0.5)	40.2 (0.6)	41.4 (0.5)	40.6 (0.3)	39.9 (0.3)	41.1 (0.3)

DCE AND IVIM PARAMETER MAPS

The DCE and IVIM parameter maps of the central slice through each tumor are displayed in Figure 4. Variations in the parameter maps can be observed between the rabbits, both before and after hyperthermia. Rabbit 2 died during treatment; the corresponding data were excluded from the analysis. The signal-to-noise ratio of the pre-hyperthermia IVIM data acquired in rabbit 5 was very low. We therefore decided to refrain from including IVIM data from this animal in any comparisons. Decreased values can be observed in the post-hyperthermia v_p map of rabbit 3 (v_p<0.02) and in all post-hyperthermia DCE maps of rabbit 4 (v_p<0.02, K^{trans}<0.4, k_{ep}<0.4, Fig.4a).

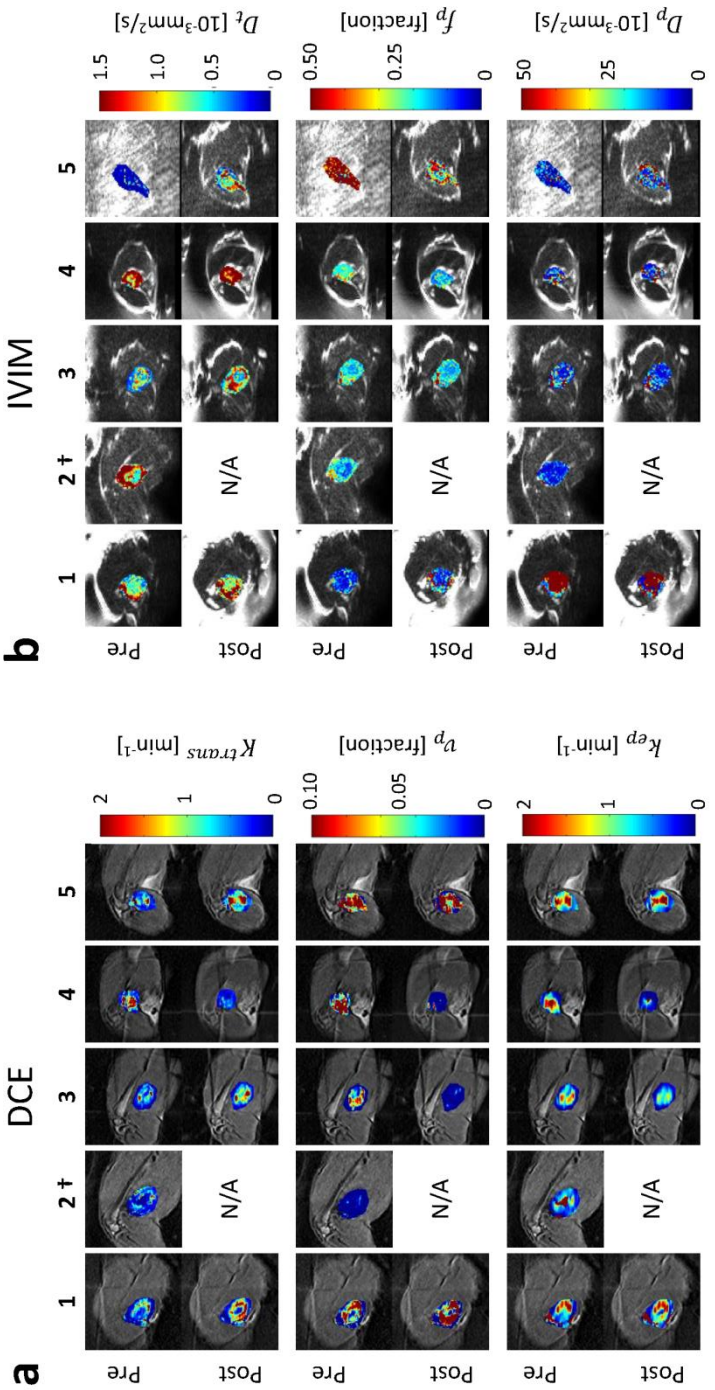

Figure 4. Pre- and post-hyperthermia DCE **(a)** and IVIM **(b)** parameter maps of the central slices through the tumor for all rabbits (1-5). The parameter maps were masked using the tumor VOIs and are shown as an overlay over the corresponding magnitude image (20th dynamic for DCE and b = 0 s/mm^2 for IVIM). Rabbit 2 (†) died during the treatment.

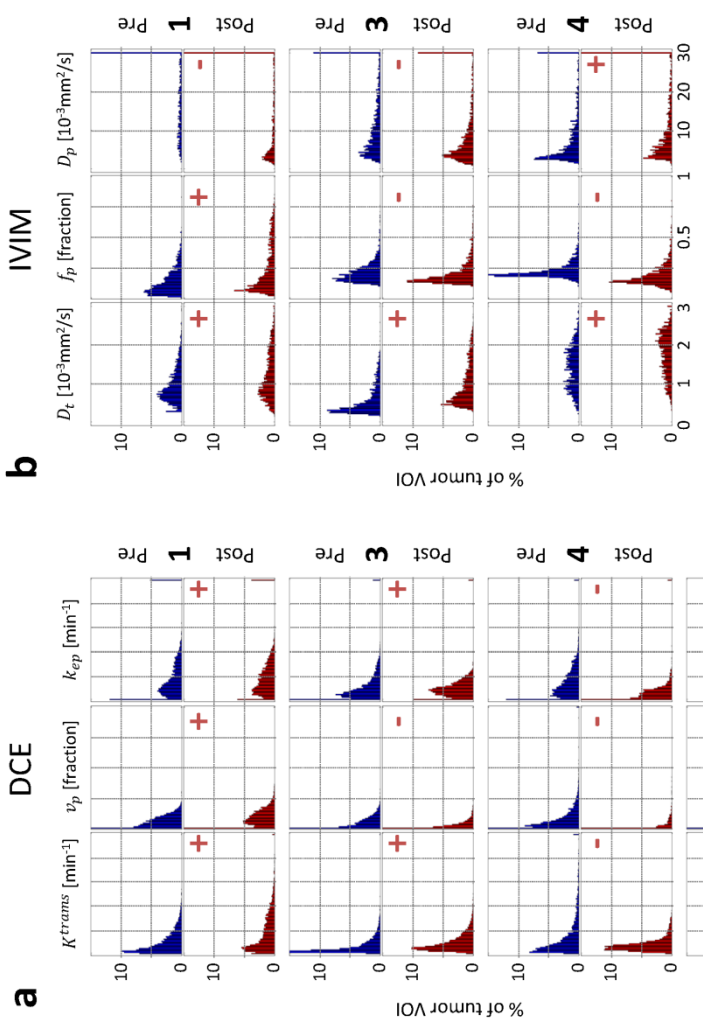

Figure 5. Histograms of the pre- and post-hyperthermia DCE parameters (a) and of the IVIM parameters (b) in the tumor VOI of the rabbits included in the analysis. Median changes are indicated at the top-right of each post-hyperthermia histogram: (+) increase, (-) decrease.

HISTOGRAMS AND MEDIAN VALUES

Pre- and post-hyperthermia histograms of the DCE parameters in the tumor VOIs are shown in Figure 5a. Variations in the pre-hyperthermia histograms can be observed between the rabbits, in particular the k_{ep} histograms. Table 2 shows the comparisons of pre- and post-hyperthermia median values of the DCE parameters and the corresponding *p*-values. All changes after hyperthermia in the histograms and median values were found to be significant (*p<0.001*), except for the k_{ep} values of rabbit 3 (*p=0.006*). The changes are most obvious in rabbit 4, where all three DCE parameter histograms, as well as the median values, shifted towards lower values. For all other rabbits, the K^{trans} histograms and the median K^{trans} values shifted towards higher values. The median v_p increased in rabbits 1 and 5, and decreased in rabbits 3 and 4. In the k_{ep} histograms of rabbits 3 and 4, clear shape changes can be observed. The median k_{ep} increased in rabbit 1 and decreased in rabbits 4 and 5. In rabbit 3, the bulk shift in the k_{ep} distribution towards lower values changed the skewness (Fig.5a). This resulted in an increase in the median k_{ep} (Table 2), which does not reflect the observed changes in the histogram (*p=0.006*).

Pre- and post-hyperthermia histograms of the IVIM parameters in the tumor VOIs are shown in Figure 5b. It is notable that all pre-hyperthermia histograms look different in shape. Table 3 shows the comparisons of the pre- and post-hyperthermia median values of the IVIM parameters and the corresponding *p*-values; all changes after hyperthermia were found to be significant (*p<0.001*). All D_t histograms shifted towards higher values after hyperthermia. In the histograms and median values of f_p an increase was found in rabbit 1 and a decrease in rabbits 3 and 4. The pre-hyperthermia D_p histogram of rabbit 1 shows an even distribution covering a wide range and the median value was much larger than all other median D_p values (Table 3). The median D_p value decreased in rabbit 3 and increased in rabbit 4.

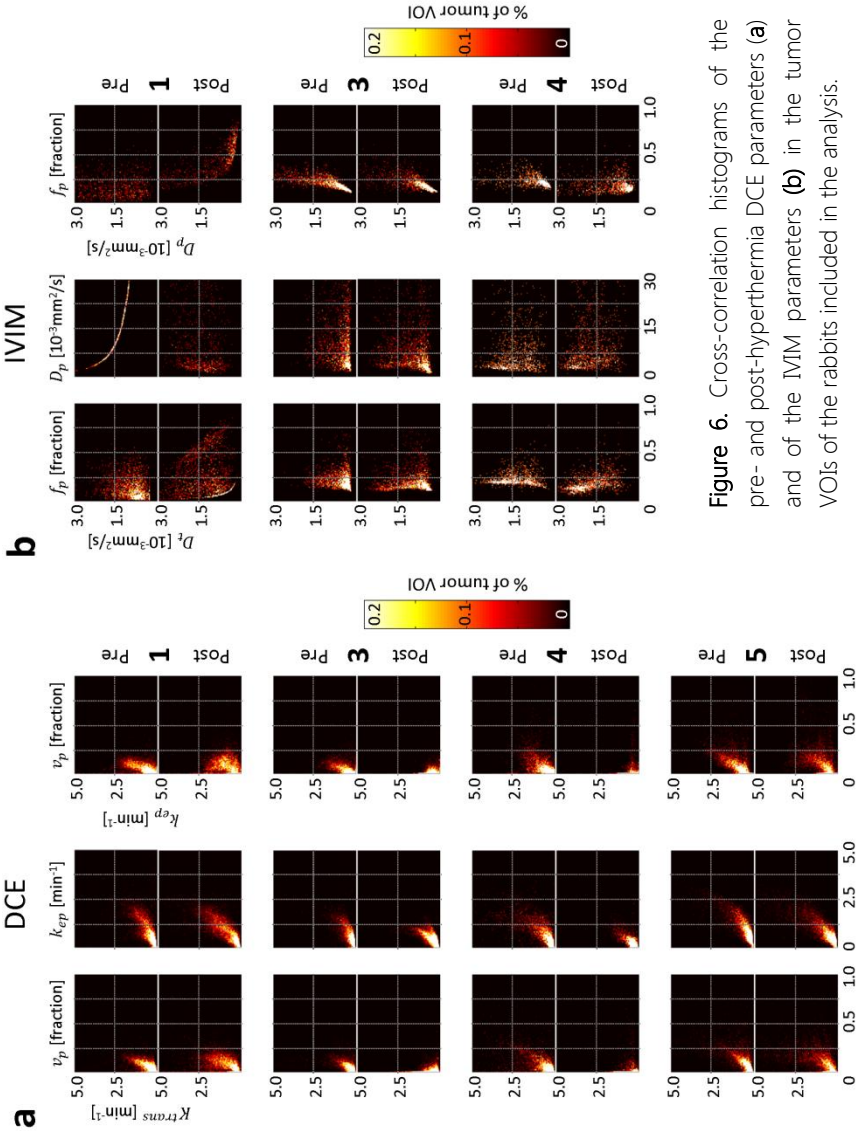

Figure 6. Cross-correlation histograms of the pre- and post-hyperthermia DCE parameters (a) and of the IVIM parameters (b) in the tumor VOIs of the rabbits included in the analysis.

CROSS-CORRELATION HISTOGRAMS

The two-dimensional cross-correlation histograms of the DCE parameters in the tumor VOIs are displayed in Figure 6a. The shapes of the different pre-hyperthermia cross-correlation histograms are comparable for rabbits 1, 3 and 5; for rabbit 4 the shapes are less elongated and more diffuse. After hyperthermia, the cross-correlation histograms of rabbits 1 and 5 become more diffuse, while those of rabbits 3 and 4 become more compact, particularly the $v_p \times K^{trans}$ and $v_p \times k_{ep}$ histograms.

The cross-correlation histograms of the IVIM parameters in the tumor VOIs are displayed in Figure 6b. In rabbit 1, the pre-hyperthermia $D_p \times D_t$ histogram shows a strong correlation between the parameters for all voxels, which indicate systematic errors in the parameter estimation. Similarly, the post-hyperthermia $f_p \times D_t$ histogram of rabbit 1 shows a strong correlation between the parameters for a large portion of the voxels. The cross-correlation histograms of rabbits 3 and 4 have similar shapes, but differ in their distributions: in rabbit 4 there were more voxels with low f_p values in combination with high D_t values.

DISCUSSION

DCE-MRI and IVIM-MRI data were acquired before and after MR-HIFU induced hyperthermia in rabbits with Vx2 tumors. The pre-hyperthermia DCE and IVIM parameter maps and histograms revealed variations between the rabbits. This implies that the group was heterogeneous in terms of DCE and IVIM parameter distributions. This heterogeneity was also observed in five other rabbits that did not receive the hyperthermia treatment and were therefore not included in this study (data not shown). The post-hyperthermia data were acquired within one hour after hyperthermia. Although the duration of the physiological effects after applying hyperthermia is a controversial aspect (179), several studies have shown that changes in regional blood flow and permeability persisted and could be detected up to a few hours after hyperthermia (142,144,145). The changes in the DCE and IVIM parameter after hyperthermia varied between the rabbits and are discussed below.

All changes in the DCE histograms and median values after hyperthermia were found to be statistically significantly different ($p<0.001$), except for the median k_{ep} in rabbit 3 ($p=0.006$).

In rabbit 4, all DCE parameter values in the tumor VOI decreased to very low values after hyperthermia, as could be clearly seen in the parameter maps as well as in the histograms. These changes differed substantially from the changes found in the other rabbits. Rabbit 4 had three contiguous small tumors instead of a single tumor. This difference in pre-hyperthermic condition may have led to a different physiological response in this rabbit from that in the other rabbits.

In the other rabbits (rabbits 1, 3 and 5), an increase in K^{trans} was observed after hyperthermia. The median k_{ep} values of rabbits 1 and 3 increased and decreased in rabbits 4 and 5. The changes in the median K^{trans} and k_{ep} values were in the order of 0.2 min^{-1}, where extreme outliers were excluded to have a realistic representation of the parameter value distribution. Hijnen, et al. (170) showed K^{trans} changes of about 0.1 min^{-1} after hyperthermia in tumor-bearing mice in the non-necrotic tumor areas, which is in the same order of magnitude as the changes observed in this study. In the whole tumor, changes in the mean K^{trans} and k_{ep} values were smaller (0.017 min^{-1} and 0.022 min^{-1}). Discrepancies between the results may be explained by the different tumor and animal models. In addition, a different model was used for the DCE analysis, standard Tofts (180) versus Extended Tofts (150), resulting in a discrepancy in the permeability and flow contributions in K^{trans} (181).

In v_p, an increase was observed in rabbits 1 and 5 and a decrease in rabbit 3. Interestingly, hyperthermic temperatures measured in the coronal slice of rabbit 3 were higher than in the other rabbits: the mean T_{50} was close to 42°C and the mean T_{10} was higher than 42°C. Since v_p represents the blood plasma volume fraction in a voxel, it is strongly related to the size of the vessels. It is well known that tumor capillaries are hastily formed and lack the ability to actively dilate. However, tumor capillaries may passively dilate upon hyperthermia, as a result of increased blood flow in adjacent tissue or of increased cardiac output (18), which may explain the increase in v_p observed in rabbits 1 and 5. At moderate hyperthermic temperatures (>42°C)

reduced tumor vessel diameters have been reported in Vx2 tumors in rabbit ear chambers (17), which may explain the observed v_p decrease in rabbit 3. Dudar and Jain (17) suggested the reduction of tumor vessel diameters may be attributed to swelling of the endothelial cells and tissue parenchyma, induced by a decreased pH in tumors during hyperthermia. The k_{ep} histogram shapes of rabbits 3 and 4 clearly changed after hyperthermia to a more compact distribution. It is notable that these are the same rabbits that showed a decrease in v_p. This potential relation can be seen more clearly in the $v_p \times k_{ep}$ histograms of these rabbits.

For the IVIM analysis, the reproducibility was tested by comparing a repeated IVIM scan. No significant differences were found between the f_p and D_p histograms and median values (*p=0.14* and *p=0.09*). The changes in D_t were significantly different (*p<0.001)*, but the difference of 0.14×10^{-3}mm^2/s between the median values was relatively small compared to the median values (13% and 12%).

The pre-hyperthermia IVIM data of rabbit 5 had a low signal-to-noise ratio, possibly due to motion during the acquisition, hence a reliable comparison with the post-hyperthermia data was not possible. In the other rabbits, all changes in the IVIM histograms and median values after hyperthermia were found to be statistically significantly different (*p<0.001*).

A clear increase in D_t after hyperthermia could be seen in rabbits 1, 3 and 4. The changes in the median values were factors of 1.7, 2.6 and 3.0 times larger than the difference found in the reproducibility test. This indicates that the observed changes in D_t are likely to be induced by hyperthermia. In f_p, an increase was observed in rabbit 1 and a decrease in rabbits 3 and 4, similarly to the changes observed in v_p. While the interpretations of f_p and v_p are different, signal fraction and volume fraction respectively, the parameters are strongly related to each other as they both reflect the intra-voxel fraction of the vascular component.

The f_p values in rabbit 1 are much lower than in the other rabbits, which indicates an overall small contribution of vascular components to the signal. The cross-correlation histograms of these data revealed a strong correlation between D_t and D_p, suggesting systematic errors in the parameter estimation. The low f_p values are likely the reason for the systematic D_p

estimation errors, inasmuch D_p cannot be estimated accurately when f_p is too low (182,183).

While the results show that changes in DCE and IVIM parameters after MR-HIFU induced hyperthermia could be detected, the changes were found to be variable between the rabbits. The group appeared to be heterogeneous in terms of DCE and IVIM parameter distributions and it is likely that such a start condition would result in a heterogeneous outcome. In future research, stratification of starting conditions would be desirable, which requires a larger number of subjects.

CONCLUSION

In this study we have shown that DCE and IVIM parameters maps and (cross-correlation) histograms could be constructed to detect changes after MR-HIFU induced hyperthermia in rabbit Vx2 tumors. Perfusion parameter histograms provided insight into changes of the parameter distributions and showed that changes in most of the median values were statistically significant ($p<0.001$). However, the detected changes were variable between the rabbits. The results suggest that DCE- and IVIM-MRI may be promising tools to assess tumor physiology responses to hyperthermia. Further research in a larger number of subjects is necessary to assess their value for treatment response monitoring.

"The difference between stupidity and genius

is that genius has its limits"

– Albert Einstein

Chapter 6

General discussion

In this thesis, research on MRI-based methods for the evaluation of thermal effects induced by MR-HIFU was presented and discussed. The described studies were performed within the context of the CTMM project "HIFU-CHEM". The purpose of the HIFU-CHEM project was to develop and test an MR-HIFU technology platform specifically for local drug delivery using thermosensitive liposomes. The primary clinical objective was to treat painful bone metastases. In this chapter, the implications of the studies are discussed and some future perspectives are outlined.

EVALUATION OF THE DIRECT HEATING PROCESS

The MRT method most commonly used for monitoring clinical MR-HIFU treatments is the proton resonance frequency shift-based (PRFS) MRT. In **CHAPTER 2**, the performance of the PRFS MRT method for monitoring clinical palliative treatments of painful bone metastases was assessed. The most important finding was that the temperature accuracy was limited because of artifacts in the MRT images. The most dominant artifacts originated from the patients' respiration, which had an influence on the treatment monitoring in almost all cases. Even at anatomical locations away from the lungs, these respiration-induced artifacts were observed to affect the MRT images. In addition, the image quality was found to be variable between the different lesion types and depended on the amount of cortical bone present.

The PRFS MRT used for monitoring in these treatments suffices for heat localization but not for accurate temperature measurements. In order to retrieve reliable temperatures, it is necessary to correct for respiration effects. This could be done with for example the multi-baseline method (93,95). With this method, a set of baseline images for PRFS MRT are acquired over the whole respiratory cycle before treatment. During treatment, the corresponding baseline phase map is selected according to the respiratory state for each temperature image. Although the total treatment time may increase because of the acquisition of the set of baseline images, this will provide a practical and feasible solution to the respiration effects. An alternative is the self-reference or referenceless MRT method (123,124). This

method uses the extrapolated phase of a region selected in the surrounding unheated tissue, outside the expected heated region, to serve as baseline for the heated region of interest. The elegance of this method is that both the baseline phase and the phase of the heated region, of which the temperature is to be calculated, originate from the same image. However, this method may be limited when there is no clearly defined region where the heating is expected, or when the surrounding tissue available to serve as reference is limited. The choice of the method to correct respiration effects will depend on the specific needs.

Since PRFS MRT only allows temperature measurements in aqueous tissue, its use is limited when treating bone metastases. Osteolytic lesions are aqueous and may allow temperature measurements. However, osteoblastic lesions are composed of cortical bone, lacking signal for most MR sequences due to the very short transverse relaxation time (83). Osteoblastic lesions give no or little signal in PRFS MRT images, impeding temperature measurements. Mixed lesions are partially composed of cortical bone and give only limited signal in PRFS MRT images, impeding reliable temperature measurements. Since bone lesions are located in bone structures, the lesions are surrounded by bone marrow and bone cortex. In the cortex there is a lack of MR signal and in bone marrow the possibility of using PRFS MRT is limited due to the presence of fat.

Efforts have been made to investigate the use of ultra-short echo MRI techniques to measure the temperature in cortical bone. An ultra-short echo technique with variable flip angle has been proposed to measure the temperature dependent longitudinal relaxation time T1 (184). Although promising, its major limitation is the total scan duration of 8 minutes. Another MR thermometry sequence proposed for the use in cortical bone is a dual-echo acquisition, of which one echo is ultra-short (97). Temperatures were calculated from the change in magnitude and a linear calibration value, measured during a separate cooling experiment. Although this method has an acceptable scan duration (7 s), the magnitude changes and temperature changes measured were not quantitatively consistent across the bone samples. In addition, for both methods small ex vivo bone samples were used, allowing the use of small surface coils. In clinical practice, larger coils are needed to cover the targeted anatomy, resulting in lower SNR than in

those experiments. MRT methods have been proposed to measure the temperature in bone marrow. Using gradient-echo MR sequences, with the analysis in either time domain (29,185) or frequency domain (186), temperatures can be calculated from the frequency difference between the water and fat components in bone marrow. These methods would be complementary to the other methods in terms of tissue type.

For the application of MR-HIFU in abdominal organs such as the liver, the near-field region, located in the pre-focal beam path, is at risk of undesired heating and the temperature there should be monitored. The results presented in **CHAPTER 3** show that the multi-gradient echo (MGE) MRT method can be used to monitor the near-field area of abdominal organs. Temperatures were measured in the muscle layer in the ventral abdominal wall, using signal from the adjacent fat layer as a reference. By subtracting absolute MGE temperature maps, relative temperature maps were reconstructed. Relative MGE MRT enabled capturing subsequent heating by consecutive sonications with MR-HIFU without being affected by field drift. Using this method, the relative temperature changes may be measured interleaved between scans of a clinical protocol, making it a potentially valuable treatment monitoring tool. It can be used complementary with the recently proposed T2-based method (31), which measures the temperature in the fat layer of the ventral abdominal wall. The absolute MGE MRT temperature maps showed systematic errors, which were cancelled out in the relative temperature maps. The magnetic susceptibility distribution of water and fat was most likely the source of these systematic errors (113).

The effect of the susceptibility distribution of water and fat on MGE MRT was further investigated in **CHAPTER 4**. The water and fat signals of macroscopically homogeneous water-fat system were analyzed using numerical simulations. By doing this, the behavior of the simulated signals could be compared to the theoretical behavior, which was derived by Yablonskiy and Haacke (127) for point perturbers in a water medium. In the case of macroscopically homogeneous water-fat systems, such as emulsions, fat can be considered as spherical perturbers in a water medium. The numerical simulation results were presented in CHAPTER 4 and showed that both the water signal and the fat signal show a combined short- and long-

time behavior, corresponding to the theoretical description of Yablonskiy and Haacke (127). Accordingly, three ranges were defined where both the water and fat signals are either in the short or in the long regime. By sampling the signal in one of those three ranges, by delaying the start of the signal sampling, the systematic errors in the MGE MRT method due to the field effects were reduced. Although this theoretical finding should be verified by experiments, it may provide handles to a practical solution to reduce the errors in the absolute temperatures measured using MGE MRT. Further research is necessary to investigate the implications for macroscopically heterogeneous water-fat systems, such as those described in Chapter 3.

EVALUATION OF INDIRECT PHYSIOLOGICAL EFFECTS

Mild hyperthermia (40°C to 45°C) induces physiological effects without direct damage to the tissue (4,5). Dynamic contrast enhanced (DCE)-MRI and intravoxel incoherent motion (IVIM)-MRI both allow the mapping of parameters related to the physiology, such as the permeability and the blood volume fraction. While DCE-MRI has been used more widely than IVIM-MRI, IVIM-MRI has the advantage that no contrast agents are involved. The potential of DCE-MRI and IVIM-MRI to detect MR-HIFU hyperthermia-induced changes was investigated in a pre-clinical setting in **CHAPTER 5**.

The exact interpretation of the DCE parameter values remains challenging. It is unclear how to interpret the parameters when there is a mismatch between the actual physiological process underlying the MR signal and the DCE model, describing the process, used for the analysis (181). This is especially true for heterogeneous tumors, where the physiological processes of poorly vascularized and of well-vascularized parts are different. Since we are interested in the effects of hyperthermia om perfusion, the Extended Tofts-Kety model (150) is the most suitable model as it includes the blood volume fraction v_p (147). By using this model consistently before and after hyperthermia, changes in the parameter values can provide insight in the induced effects on the physiology. The most interesting IVIM parameter for detecting mild hyperthermia effects is the blood signal fraction f_p.

Interestingly, the changes in f_p were similar to the changes in v_p, confirming the shared characteristic of representing the intravoxel blood fraction. The advantage of IVIM over DCE is that no contrast agents are required and may thus be used repeatedly.

The changes in the DCE and IVIM parameters were variable between the rabbits. This was mostly owing to the heterogeneity in the group before hyperthermia, in terms of tumor growth and DCE and IVIM parameter distributions. The rabbit with three contiguous small tumors, instead of a single tumor, showed different changes in the parameter values as compared to the other rabbits. It is likely that differences in lesions will also lead to differences in their response to mild hyperthermia. Another observation is that the blood volume fraction v_p showed an increasing trend, except for the rabbit where higher temperatures were reached. We have shown that changes in DCE and IVIM parameters could be measured and plausible explanations exist for the observations made. One other study reported on changes in the DCE parameters before and after hyperthermia, using the standard Tofts model (170,180). Their results and the results of this study showed discrepancies, owing to the difference in the used DCE models. In both studies there have been voxels of which the physiological processes underlying the MR signal are not well-described by the used model. Ideally, the best representative model would be considered voxel-wise and applied accordingly. This would require an sophisticated classification step, where the best representative model would be assigned for each voxel. The challenge is then to define a good trade-off between how well a model describes the signal and the stability (187).

FUTURE PERSPECTIVES

Bringing the MR-HIFU technology closer towards clinical oncological applications requires the development of more robust and reliable MR thermometry methods. This holds for both the application of thermal ablation treatments and mild hyperthermia for local drug delivery. Respiration strongly influences the quality of the currently used MRT for clinical treatment of painful bone metastases. The respiration effects will be more dominant in anatomical locations closer to the lungs. Therefore, correction methods are necessary for abdominal applications such as the liver, kidney and pancreas.

Additional challenges for these organs are the near-field, which is at risk of overheating, and the presence of the ribs. Ribs have high absorption coefficients and will thus heat up easily when exposed to the ultrasound waves. Intercostal sonication methods have been proposed to avoid exposure of the ribs (98). However, recently it has been shown that intercostal sonications are associated with increased risk of near-field overheating (188). This emphasizes the need for monitoring the near-field. The use of another transducer design may provide the opportunity to deposit energy at the focus more effectively, reducing the near-field exposure (189).

BIBLIOGRAPHY

1. Wyld L, Audisio RA, Poston GJ. The evolution of cancer surgery and future perspectives. Nat Rev Clin Oncol 2015;12:115-124.
2. Wust P, Hildebrandt B, Sreenivasa G, Rau B, Gellermann J, Riess H, Felix R, Schlag PM. Hyperthermia in combined treatment of cancer. Lancet Oncol 2002;3:487-497.
3. Hurwitz M, Stauffer P. Hyperthermia, radiation and chemotherapy: the role of heat in multidisciplinary cancer care. Semin Oncol 2014;41:714-729.
4. Falk MH, Issels RD. Hyperthermia in oncology. Int J Hyperthermia 2001;17:1-18.
5. Partanen A, Yarmolenko PS, Viitala A, Appanaboyina S, Haemmerich D, Ranjan A, Jacobs G, Woods D, Enholm J, Wood BJ, Dreher MR. Mild hyperthermia with magnetic resonance-guided high-intensity focused ultrasound for applications in drug delivery. Int J Hyperthermia 2012;28:320-336.
6. Overgaard J, Gonzalez Gonzalez D, Hulshof MC, Arcangeli G, Dahl O, Mella O, Bentzen SM. Randomised trial of hyperthermia as adjuvant to radiotherapy for recurrent or metastatic malignant melanoma. European Society for Hyperthermic Oncology. Lancet 1995;345:540-543.
7. Vujaskovic Z, Song CW. Physiological mechanisms underlying heat-induced radiosensitization. Int J Hyperthermia 2004;20:163-174.
8. Grull H, Langereis S. Hyperthermia-triggered drug delivery from temperature-sensitive liposomes using MRI-guided high intensity focused ultrasound. J Control Release 2012;161:317-327.
9. McDaniel JR, Dewhirst MW, Chilkoti A. Actively targeting solid tumours with thermoresponsive drug delivery systems that respond to mild hyperthermia. Int J Hyperthermia 2013;29:501-510.
10. Diederich CJ. Thermal ablation and high-temperature thermal therapy: overview of technology and clinical implementation. Int J Hyperthermia 2005;21:745-753.
11. Sapareto SA, Dewey WC. Thermal dose determination in cancer therapy. Int J Radiat Oncol Biol Phys 1984;10:787-800.

12. ter Haar G. Ultrasound focal beam surgery. Ultrasound Med Biol 1995;21:1089-1100.
13. Stafford RJ, Fuentes D, Elliott AA, Weinberg JS, Ahrar K. Laser-induced thermal therapy for tumor ablation. Crit Rev Biomed Eng 2010;38:79-100.
14. De Filippo M, Bozzetti F, Martora R, Zagaria R, Ferretti S, Macarini L, Brunese L, Rotondo A, Rossi C. Radiofrequency thermal ablation of renal tumors. Radiol Med 2014;119:499-511.
15. Tempany CM, McDannold NJ, Hynynen K, Jolesz FA. Focused ultrasound surgery in oncology: overview and principles. Radiology 2011;259:39-56.
16. ter Haar G. Therapeutic ultrasound. Eur J Ultrasound 1999;9:3-9.
17. Dudar TE, Jain RK. Differential response of normal and tumor microcirculation to hyperthermia. Cancer Res 1984;44:605-612.
18. Song CW. Effect of local hyperthermia on blood flow and microenvironment: a review. Cancer Res 1984;44:4721s-4730s.
19. Taylor DG, Bore CF. A review of the magnetic resonance response of biological tissue and its applicability to the diagnosis of cancer by NMR radiology. J Comput Tomogr 1981;5:122-133.
20. Rieke V, Butts Pauly K. MR thermometry. J Magn Reson Imaging 2008;27:376-390.
21. Hynynen K, Freund WR, Cline HE, Chung AH, Watkins RD, Vetro JP, Jolesz FA. A clinical, noninvasive, MR imaging-monitored ultrasound surgery method. Radiographics 1996;16:185-195.
22. Jolesz FA. MRI-guided focused ultrasound surgery. Annu Rev Med 2009;60:417-430.
23. Kim Y-s. Advances in MR image-guided high-intensity focused ultrasound therapy. International Journal of Hyperthermia 2015;31:225-232.
24. Hectors SJ, Jacobs I, Moonen CT, Strijkers GJ, Nicolay K. MRI methods for the evaluation of high intensity focused ultrasound tumor treatment: Current status and future needs. Magn Reson Med 2015.
25. Ishihara Y, Calderon A, Watanabe H, Okamoto K, Suzuki Y, Kuroda K, Suzuki Y. A precise and fast temperature mapping using water proton chemical shift. Magn Reson Med 1995;34:814-823.
26. De Poorter J. Noninvasive MRI thermometry with the proton resonance frequency method: study of susceptibility effects. Magn Reson Med 1995;34:359-367.

27. Chen J, Daniel BL, Pauly KB. Investigation of proton density for measuring tissue temperature. J Magn Reson Imaging 2006;23:430-434.
28. McDannold N, Barnes AS, Rybicki FJ, Oshio K, Chen NK, Hynynen K, Mulkern RV. Temperature mapping considerations in the breast with line scan echo planar spectroscopic imaging. Magn Reson Med 2007;58:1117-1123.
29. Sprinkhuizen SM, Bakker CJ, Bartels LW. Absolute MR thermometry using time-domain analysis of multi-gradient-echo magnitude images. Magn Reson Med 2010;64:239-248.
30. Todd N, Diakite M, Payne A, Parker DL. In vivo evaluation of multi-echo hybrid PRF/T1 approach for temperature monitoring during breast MR-guided focused ultrasound surgery treatments. Magn Reson Med 2014;72:793-799.
31. Baron P, Ries M, Deckers R, de Greef M, Tanttu J, Kohler M, Viergever MA, Moonen CT, Bartels LW. In vivo T2 -based MR thermometry in adipose tissue layers for high-intensity focused ultrasound near-field monitoring. Magn Reson Med 2014;72:1057-1064.
32. Muller N, Reiter RC. Temperature Dependence of Chemical Shifts of Protons in Hydrogen Bonds. The Journal of Chemical Physics 1965;42:3265-3269.
33. Hindman JC. Proton Resonance Shift of Water in the Gas and Liquid States. The Journal of Chemical Physics 1966;44:4582-4592.
34. Kuroda K. Non-invasive MR thermography using the water proton chemical shift. Int J Hyperthermia 2005;21:547-560.
35. Jolesz FA, McDannold N. Current status and future potential of MRI-guided focused ultrasound surgery. J Magn Reson Imaging 2008;27:391-399.
36. Wood BJ, Ramkaransingh JR, Fojo T, Walther MM, Libutti SK. Percutaneous tumor ablation with radiofrequency. Cancer 2002;94:443-451.
37. Quinn SD, Gedroyc WM. Thermal ablative treatment of uterine fibroids. Int J Hyperthermia 2015;31:272-279.
38. Rodrigues DB, Stauffer PR, Vrba D, Hurwitz MD. Focused ultrasound for treatment of bone tumours. International Journal of Hyperthermia 2015;31:260-271.
39. Merckel LG, Bartels LW, Kohler MO, van den Bongard HJ, Deckers R, Mali WP, Binkert CA, Moonen CT, Gilhuijs KG, van den Bosch MA. MR-guided high-intensity focused ultrasound ablation of breast

cancer with a dedicated breast platform. Cardiovasc Intervent Radiol 2013;36:292-301.
40. Wijlemans JW, de Greef M, Schubert G, Bartels LW, Moonen CT, van den Bosch MA, Ries M. A Clinically Feasible Treatment Protocol for Magnetic Resonance-Guided High-Intensity Focused Ultrasound Ablation in the Liver. Invest Radiol 2014.
41. Anzidei M, Marincola BC, Bezzi M, Brachetti G, Nudo F, Cortesi E, Berloco P, Catalano C, Napoli A. Magnetic resonance-guided high-intensity focused ultrasound treatment of locally advanced pancreatic adenocarcinoma: preliminary experience for pain palliation and local tumor control. Invest Radiol 2014;49:759-765.
42. Siddiqui K, Chopra R, Vedula S, Sugar L, Haider M, Boyes A, Musquera M, Bronskill M, Klotz L. MRI-guided transurethral ultrasound therapy of the prostate gland using real-time thermal mapping: initial studies. Urology 2010;76:1506-1511.
43. Ghanouni P, Pauly KB, Elias WJ, Henderson J, Sheehan J, Monteith S, Wintermark M. Transcranial MRI-Guided Focused Ultrasound: A Review of the Technologic and Neurologic Applications. AJR Am J Roentgenol 2015;205:150-159.
44. Vimeux FC, De Zwart JA, Palussiere J, Fawaz R, Delalande C, Canioni P, Grenier N, Moonen CT. Real-time control of focused ultrasound heating based on rapid MR thermometry. Invest Radiol 1999;34:190-193.
45. Vanne A, Hynynen K. MRI feedback temperature control for focused ultrasound surgery. Phys Med Biol 2003;48:31-43.
46. Staruch RM, Ganguly M, Tannock IF, Hynynen K, Chopra R. Enhanced drug delivery in rabbit VX2 tumours using thermosensitive liposomes and MRI-controlled focused ultrasound hyperthermia. Int J Hyperthermia 2012;28:776-787.
47. de Smet M, Hijnen NM, Langereis S, Elevelt A, Heijman E, Dubois L, Lambin P, Grull H. Magnetic resonance guided high-intensity focused ultrasound mediated hyperthermia improves the intratumoral distribution of temperature-sensitive liposomal doxorubicin. Invest Radiol 2013;48:395-405.
48. Huisman M, Lam MK, Bartels LW, Nijenhuis RJ, Moonen CT, Knuttel FM, Verkooijen HM, van Vulpen M, van den Bosch MA. Feasibility of volumetric MRI-guided high intensity focused ultrasound (MR-HIFU) for painful bone metastases. J Ther Ultrasound 2014;2:16.
49. Zhang L, Zhu H, Jin C, Zhou K, Li K, Su H, Chen W, Bai J, Wang Z. High-intensity focused ultrasound (HIFU): effective and safe therapy

for hepatocellular carcinoma adjacent to major hepatic veins. Eur Radiol 2009;19:437-445.
50. Zhu H, Zhou K, Zhang L, Jin C, Peng S, Yang W, Li K, Su H, Chen W, Bai J, Wu F, Wang Z. High intensity focused ultrasound (HIFU) therapy for local treatment of hepatocellular carcinoma: role of partial rib resection. Eur J Radiol 2009;72:160-166.
51. Jung SE, Cho SH, Jang JH, Han JY. High-intensity focused ultrasound ablation in hepatic and pancreatic cancer: complications. Abdom Imaging 2011;36:185-195.
52. Quesson B, Laurent C, Maclair G, de Senneville BD, Mougenot C, Ries M, Carteret T, Rullier A, Moonen CT. Real-time volumetric MRI thermometry of focused ultrasound ablation in vivo: a feasibility study in pig liver and kidney. NMR Biomed 2011;24:145-153.
53. Li C, Zhang W, Fan W, Huang J, Zhang F, Wu P. Noninvasive treatment of malignant bone tumors using high-intensity focused ultrasound. Cancer 2010;116:3934-3942.
54. Wu F, Chen WZ, Bai J, Zou JZ, Wang ZL, Zhu H, Wang ZB. Pathological changes in human malignant carcinoma treated with high-intensity focused ultrasound. Ultrasound Med Biol 2001;27:1099-1106.
55. Orgera G, Monfardini L, Della Vigna P, Zhang L, Bonomo G, Arnone P, Padrenostro M, Orsi F. High-intensity focused ultrasound (HIFU) in patients with solid malignancies: evaluation of feasibility, local tumour response and clinical results. Radiol Med 2011;116:734-748.
56. Chen W, Zhu H, Zhang L, Li K, Su H, Jin C, Zhou K, Bai J, Wu F, Wang Z. Primary bone malignancy: effective treatment with high-intensity focused ultrasound ablation. Radiology 2010;255:967-978.
57. Leslie T, Ritchie R, Illing R, Ter Haar G, Phillips R, Middleton M, Bch B, Wu F, Cranston D. High-intensity focused ultrasound treatment of liver tumours: post-treatment MRI correlates well with intra-operative estimates of treatment volume. Br J Radiol 2012;85:1363-1370.
58. Kennedy JE, Wu F, ter Haar GR, Gleeson FV, Phillips RR, Middleton MR, Cranston D. High-intensity focused ultrasound for the treatment of liver tumours. Ultrasonics 2004;42:931-935.
59. Wu F, Wang ZB, Chen WZ, Zou JZ, Bai J, Zhu H, Li KQ, Jin CB, Xie FL, Su HB. Advanced hepatocellular carcinoma: treatment with high-intensity focused ultrasound ablation combined with transcatheter arterial embolization. Radiology 2005;235:659-667.

60. Xu G, Luo G, He L, Li J, Shan H, Zhang R, Li Y, Gao X, Lin S, Wang G. Follow-up of high-intensity focused ultrasound treatment for patients with hepatocellular carcinoma. Ultrasound Med Biol 2011;37:1993-1999.
61. Illing RO, Kennedy JE, Wu F, ter Haar GR, Protheroe AS, Friend PJ, Gleeson FV, Cranston DW, Phillips RR, Middleton MR. The safety and feasibility of extracorporeal high-intensity focused ultrasound (HIFU) for the treatment of liver and kidney tumours in a Western population. Br J Cancer 2005;93:890-895.
62. Zhang Y, Zhao J, Guo D, Zhong W, Ran L. Evaluation of short-term response of high intensity focused ultrasound ablation for primary hepatic carcinoma: utility of contrast-enhanced MRI and diffusion-weighted imaging. Eur J Radiol 2011;79:347-352.
63. Napoli A, Anzidei M, Ciolina F, Marotta E, Cavallo Marincola B, Brachetti G, Di Mare L, Cartocci G, Boni F, Noce V, Bertaccini L, Catalano C. MR-guided high-intensity focused ultrasound: current status of an emerging technology. Cardiovasc Intervent Radiol 2013;36:1190-1203.
64. Wu F, Wang ZB, Zhu H, Chen WZ, Zou JZ, Bai J, Li KQ, Jin CB, Xie FL, Su HB. Feasibility of US-guided high-intensity focused ultrasound treatment in patients with advanced pancreatic cancer: initial experience. Radiology 2005;236:1034-1040.
65. Ritchie RW, Leslie T, Phillips R, Wu F, Illing R, ter Haar G, Protheroe A, Cranston D. Extracorporeal high intensity focused ultrasound for renal tumours: a 3-year follow-up. BJU Int 2010;106:1004-1009.
66. Hynynen K, Pomeroy O, Smith DN, Huber PE, McDannold NJ, Kettenbach J, Baum J, Singer S, Jolesz FA. MR imaging-guided focused ultrasound surgery of fibroadenomas in the breast: a feasibility study. Radiology 2001;219:176-185.
67. Gianfelice D, Khiat A, Amara M, Belblidia A, Boulanger Y. MR imaging-guided focused US ablation of breast cancer: histopathologic assessment of effectiveness-- initial experience. Radiology 2003;227:849-855.
68. Zippel DB, Papa MZ. The use of MR imaging guided focused ultrasound in breast cancer patients; a preliminary phase one study and review. Breast Cancer 2005;12:32-38.
69. Furusawa H, Namba K, Nakahara H, Tanaka C, Yasuda Y, Hirabara E, Imahariyama M, Komaki K. The evolving non-surgical ablation of breast cancer: MR guided focused ultrasound (MRgFUS). Breast Cancer 2007;14:55-58.

70. Tempany CM, Stewart EA, McDannold N, Quade BJ, Jolesz FA, Hynynen K. MR imaging-guided focused ultrasound surgery of uterine leiomyomas: a feasibility study. Radiology 2003;226:897-905.
71. Hindley J, Gedroyc WM, Regan L, Stewart E, Tempany C, Hynyen K, McDannold N, Inbar Y, Itzchak Y, Rabinovici J, Kim HS, Geschwind JF, Hesley G, Gostout B, Ehrenstein T, Hengst S, Sklair-Levy M, Shushan A, Jolesz F. MRI guidance of focused ultrasound therapy of uterine fibroids: early results. AJR Am J Roentgenol 2004;183:1713-1719.
72. Funaki K, Fukunishi H, Sawada K. Clinical outcomes of magnetic resonance-guided focused ultrasound surgery for uterine myomas: 24-month follow-up. Ultrasound Obstet Gynecol 2009;34:584-589.
73. Ikink ME, Voogt MJ, Verkooijen HM, Lohle PN, Schweitzer KJ, Franx A, Mali WP, Bartels LW, van den Bosch MA. Mid-term clinical efficacy of a volumetric magnetic resonance-guided high-intensity focused ultrasound technique for treatment of symptomatic uterine fibroids. Eur Radiol 2013;23:3054-3061.
74. Catane R, Beck A, Inbar Y, Rabin T, Shabshin N, Hengst S, Pfeffer RM, Hanannel A, Dogadkin O, Liberman B, Kopelman D. MR-guided focused ultrasound surgery (MRgFUS) for the palliation of pain in patients with bone metastases--preliminary clinical experience. Ann Oncol 2007;18:163-167.
75. Gianfelice D, Gupta C, Kucharczyk W, Bret P, Havill D, Clemons M. Palliative treatment of painful bone metastases with MR imaging--guided focused ultrasound. Radiology 2008;249:355-363.
76. Liberman B, Gianfelice D, Inbar Y, Beck A, Rabin T, Shabshin N, Chander G, Hengst S, Pfeffer R, Chechick A, Hanannel A, Dogadkin O, Catane R. Pain palliation in patients with bone metastases using MR-guided focused ultrasound surgery: a multicenter study. Ann Surg Oncol 2009;16:140-146.
77. Napoli A, Anzidei M, Marincola BC, Brachetti G, Ciolina F, Cartocci G, Marsecano C, Zaccagna F, Marchetti L, Cortesi E, Catalano C. Primary pain palliation and local tumor control in bone metastases treated with magnetic resonance-guided focused ultrasound. Invest Radiol 2013;48:351-358.
78. Hurwitz MD, Ghanouni P, Kanaev SV, Iozeffi D, Gianfelice D, Fennessy FM, Kuten A, Meyer JE, LeBlang SD, Roberts A, Choi J, Larner JM, Napoli A, Turkevich VG, Inbar Y, Tempany CM, Pfeffer RM. Magnetic resonance-guided focused ultrasound for patients with painful bone metastases: phase III trial results. J Natl Cancer Inst 2014;106.

79. Hynynen K, DeYoung D. Temperature elevation at muscle-bone interface during scanned, focused ultrasound hyperthermia. Int J Hyperthermia 1988;4:267-279.
80. Lutz S, Berk L, Chang E, Chow E, Hahn C, Hoskin P, Howell D, Konski A, Kachnic L, Lo S, Sahgal A, Silverman L, von Gunten C, Mendel E, Vassil A, Bruner DW, Hartsell W. Palliative radiotherapy for bone metastases: an ASTRO evidence-based guideline. Int J Radiat Oncol Biol Phys 2011;79:965-976.
81. Huisman M, van den Bosch MA, Wijlemans JW, van Vulpen M, van der Linden YM, Verkooijen HM. Effectiveness of reirradiation for painful bone metastases: a systematic review and meta-analysis. Int J Radiat Oncol Biol Phys 2012;84:8-14.
82. Mansfield P. Imaging by nuclear magnetic resonance. Journal of Physics E: Scientific Instruments 1988;21:18.
83. Du J, Hamilton G, Takahashi A, Bydder M, Chung CB. Ultrashort echo time spectroscopic imaging (UTESI) of cortical bone. Magn Reson Med 2007;58:1001-1009.
84. Kohler MO, Mougenot C, Quesson B, Enholm J, Le Bail B, Laurent C, Moonen CT, Ehnholm GJ. Volumetric HIFU ablation under 3D guidance of rapid MRI thermometry. Med Phys 2009;36:3521-3535.
85. Schenck JF. The role of magnetic susceptibility in magnetic resonance imaging: MRI magnetic compatibility of the first and second kinds. Med Phys 1996;23:815-850.
86. Perman WH, Moran PR, Moran RA, Bernstein MA. Artifacts from pulsatile flow in MR imaging. J Comput Assist Tomogr 1986;10:473-483.
87. Peters NH, Bartels LW, Sprinkhuizen SM, Vincken KL, Bakker CJ. Do respiration and cardiac motion induce magnetic field fluctuations in the breast and are there implications for MR thermometry? J Magn Reson Imaging 2009;29:731-735.
88. Marieb EN, Koehn K. Human Anatomy and Physiology. San Francisco, CA 94111: Pearson Benjamin Cunnings; 2007.
89. Deckers R, Denis de Senneville B, Schubert G, Merckel LG, Vaessen HHB, van den Bosch MAAJ, Moonen CTW, Bartels LW. Evaluation of respiration-induced magnetic field disturbance correction of MR thermometry in volunteers and in patients for MR-HIFU ablation of breast cancer: the effects of conscious sedation. International Society of Magnetic Resonance in Medicine; 2014; Milan.

90. Schmitt A, Mougenot C, Chopra R. Spatiotemporal filtering of MR-temperature artifacts arising from bowel motion during transurethral MR-HIFU. Med Phys 2014;41:113302.
91. Staruch R, Chopra R, Hynynen K. Hyperthermia in bone generated with MR imaging-controlled focused ultrasound: control strategies and drug delivery. Radiology 2012;263:117-127.
92. Vinay R, KusumDevi V. Potential of targeted drug delivery system for the treatment of bone metastasis. Drug Deliv 2014:1-9.
93. Hey S, Maclair G, de Senneville BD, Lepetit-Coiffe M, Berber Y, Kohler MO, Quesson B, Moonen CT, Ries M. Online correction of respiratory-induced field disturbances for continuous MR-thermometry in the breast. Magn Reson Med 2009;61:1494-1499.
94. Wyatt CR, Soher BJ, MacFall JR. Correction of breathing-induced errors in magnetic resonance thermometry of hyperthermia using multiecho field fitting techniques. Med Phys 2010;37:6300-6309.
95. Vigen KK, Daniel BL, Pauly JM, Butts K. Triggered, navigated, multi-baseline method for proton resonance frequency temperature mapping with respiratory motion. Magn Reson Med 2003;50:1003-1010.
96. Han M, Scott SJ, Ozhinsky E, Salgaonkar V, Larson PEZ, Diederich CJ, Rieke V, Krug R. Imaging Temperature Changes in Cortical Bone Using Ultrashort Echo-Time MRI. International Society of Magnetic Resonance Imaging; 2014; Milan.
97. Ramsay E, Mougenot C, Kazem M, Laetsch TW, Chopra R. Temperature-dependent MR signals in cortical bone: Potential for monitoring temperature changes during high-intensity focused ultrasound treatment in bone. Magn Reson Med 2014.
98. Quesson B, Merle M, Kohler MO, Mougenot C, Roujol S, de Senneville BD, Moonen CT. A method for MRI guidance of intercostal high intensity focused ultrasound ablation in the liver. Med Phys 2010;37:2533-2540.
99. Salomir R, Petrusca L, Auboiroux V, Muller A, Vargas MI, Morel DR, Goget T, Breguet R, Terraz S, Hopple J, Montet X, Becker CD, Viallon M. Magnetic resonance-guided shielding of prefocal acoustic obstacles in focused ultrasound therapy: application to intercostal ablation in liver. Invest Radiol 2013;48:366-380.
100. Okada A, Murakami T, Mikami K, Onishi H, Tanigawa N, Marukawa T, Nakamura H. A case of hepatocellular carcinoma treated by MR-guided focused ultrasound ablation with respiratory gating. Magn Reson Med Sci 2006;5:167-171.

101. Anzidei M, Napoli A, Sandolo F, Marincola BC, Di Martino M, Berloco P, Bosco S, Bezzi M, Catalano C. Magnetic resonance-guided focused ultrasound ablation in abdominal moving organs: a feasibility study in selected cases of pancreatic and liver cancer. Cardiovasc Intervent Radiol 2014;37:1611-1617.
102. Chen L, ter Haar G, Hill CR, Dworkin M, Carnochan P, Young H, Bensted JP. Effect of blood perfusion on the ablation of liver parenchyma with high-intensity focused ultrasound. Phys Med Biol 1993;38:1661-1673.
103. Jiang F, He M, Liu YJ, Wang ZB, Zhang L, Bai J. High intensity focused ultrasound ablation of goat liver in vivo: Pathologic changes of portal vein and the "heat-sink" effect. Ultrasonics 2013;53:77-83.
104. Mougenot C, Kohler MO, Enholm J, Quesson B, Moonen C. Quantification of near-field heating during volumetric MR-HIFU ablation. Med Phys 2011;38:272-282.
105. Payne A, Vyas U, Todd N, de Bever J, Christensen DA, Parker DL. The effect of electronically steering a phased array ultrasound transducer on near-field tissue heating. Med Phys 2011;38:4971-4981.
106. Kuroda K, Mulkern RV, Oshio K, Panych LP, Nakai T, Moriya T, Okuda S, Hynynen K, Jolesz FA. Temperature mapping using the water proton chemical shift: self-referenced method with echo-planar spectroscopic imaging. Magn Reson Med 2000;43:220-225.
107. Taylor BA, Hwang KP, Elliott AM, Shetty A, Hazle JD, Stafford RJ. Dynamic chemical shift imaging for image-guided thermal therapy: analysis of feasibility and potential. Med Phys 2008;35:793-803.
108. Schick F, Eismann B, Jung WI, Bongers H, Bunse M, Lutz O. Comparison of localized proton NMR signals of skeletal muscle and fat tissue in vivo: two lipid compartments in muscle tissue. Magn Reson Med 1993;29:158-167.
109. Brix G, Heiland S, Bellemann ME, Koch T, Lorenz WJ. MR imaging of fat-containing tissues: valuation of two quantitative imaging techniques in comparison with localized proton spectroscopy. Magn Reson Imaging 1993;11:977-991.
110. Yoshioka Y, Oikawa H, Ehara S, Inoue T, Ogawa A, Kanbara Y, Kubokawa M. Noninvasive measurement of temperature and fractional dissociation of imidazole in human lower leg muscles using 1H-nuclear magnetic resonance spectroscopy. J Appl Physiol (1985) 2005;98:282-287.

111. Ren J, Dimitrov I, Sherry AD, Malloy CR. Composition of adipose tissue and marrow fat in humans by 1H NMR at 7 Tesla. J Lipid Res 2008;49:2055-2062.
112. McDannold N. Quantitative MRI-based temperature mapping based on the proton resonant frequency shift: review of validation studies. Int J Hyperthermia 2005;21:533-546.
113. Baron P, Deckers R, Bouwman JG, Bakker CJ, de Greef M, Viergever MA, Moonen CT, Bartels LW. Influence of water and fat heterogeneity on fat-referenced MR thermometry. Magn Reson Med 2015.
114. Enholm JK, Kohler MO, Quesson B, Mougenot C, Moonen CT, Sokka SD. Improved volumetric MR-HIFU ablation by robust binary feedback control. IEEE Trans Biomed Eng 2010;57:103-113.
115. Mougenot C, Quesson B, de Senneville BD, de Oliveira PL, Sprinkhuizen S, Palussiere J, Grenier N, Moonen CT. Three-dimensional spatial and temporal temperature control with MR thermometry-guided focused ultrasound (MRgHIFU). Magn Reson Med 2009;61:603-614.
116. Kuroda K, Oshio K, Chung AH, Hynynen K, Jolesz FA. Temperature mapping using the water proton chemical shift: a chemical shift selective phase mapping method. Magn Reson Med 1997;38:845-851.
117. Shmatukha AV, Harvey PR, Bakker CJ. Correction of proton resonance frequency shift temperature maps for magnetic field disturbances using fat signal. J Magn Reson Imaging 2007;25:579-587.
118. Soher BJ, Wyatt C, Reeder SB, MacFall JR. Noninvasive temperature mapping with MRI using chemical shift water-fat separation. Magn Reson Med 2010;63:1238-1246.
119. Hofstetter LW, Yeo DT, Dixon WT, Kempf JG, Davis CE, Foo TK. Fat-referenced MR thermometry in the breast and prostate using IDEAL. J Magn Reson Imaging 2012;36:722-732.
120. Jenkinson M. Fast, automated, N-dimensional phase-unwrapping algorithm. Magn Reson Med 2003;49:193-197.
121. Zou C, Shen H, He M, Tie C, Chung YC, Liu X. A fast referenceless PRFS-based MR thermometry by phase finite difference. Phys Med Biol 2013;58:5735-5751.
122. Maier F, Fuentes D, Weinberg JS, Hazle JD, Stafford RJ. Robust phase unwrapping for MR temperature imaging using a magnitude-sorted

list, multi-clustering algorithm. Magn Reson Med 2015;73:1662-1668.
123. Rieke V, Vigen KK, Sommer G, Daniel BL, Pauly JM, Butts K. Referenceless PRF shift thermometry. Magn Reson Med 2004;51:1223-1231.
124. Kuroda K, Kokuryo D, Kumamoto E, Suzuki K, Matsuoka Y, Keserci B. Optimization of self-reference thermometry using complex field estimation. Magn Reson Med 2006;56:835-843.
125. Sprinkhuizen SM, Bakker CJ, Ippel JH, Boelens R, Viergever MA, Bartels LW. Temperature dependence of the magnetic volume susceptibility of human breast fat tissue: an NMR study. MAGMA 2012;25:33-39.
126. Hahn EL. Spin Echoes. Physical Review 1950;80:580-594.
127. Yablonskiy DA, Haacke EM. Theory of NMR signal behavior in magnetically inhomogeneous tissues: the static dephasing regime. Magn Reson Med 1994;32:749-763.
128. Muller RN, Gillis P, Moiny F, Roch A. Transverse relaxivity of particulate MRI contrast media: from theories to experiments. Magn Reson Med 1991;22:178-182; discussion 195-176.
129. Ogawa S, Menon RS, Tank DW, Kim SG, Merkle H, Ellermann JM, Ugurbil K. Functional brain mapping by blood oxygenation level-dependent contrast magnetic resonance imaging. A comparison of signal characteristics with a biophysical model. Biophys J 1993;64:803-812.
130. Majumdar S. Quantitative study of the susceptibility difference between trabecular bone and bone marrow: computer simulations. Magn Reson Med 1991;22:101-110.
131. Pintaske J, Muller-Bierl B, Schick F. Effect of spatial distribution of magnetic dipoles on Lamor frequency distribution and MR Signal decay--a numerical approach under static dephasing conditions. MAGMA 2006;19:46-53.
132. McDannold N, Hynynen K, Oshio K, Mulkern RV. Temperature monitoring with line scan echo planar spectroscopic imaging. Med Phys 2001;28:346-355.
133. Tang H, Wu EX, Kennan R, Liu H, Williams DS. Interleaved water and fat imaging and applications to lipid quantitation using the gradient reversal technique. J Magn Reson Imaging 2007;26:1064-1070.
134. Le Y, Dale B, Akisik F, Koons K, Lin C. Improved T , contrast concentration, and pharmacokinetic parameter quantification in the

presence of fat with two-point dixon for dynamic contrast-enhanced magnetic resonance imaging. Magn Reson Med 2015.
135. Lam MK, de Greef M, Bouwman JG, Moonen CTW, Viergever MA, Bartels LW. Multi-gradient echo MR thermometry for monitoring of the near-field area during MR-guided high intensity focused ultrasound heating. Phys Med Biol 2015;60:7729.
136. Hopkins JA, Wehrli FW. Magnetic susceptibility measurement of insoluble solids by NMR: magnetic susceptibility of bone. Magn Reson Med 1997;37:494-500.
137. Haacke EM, Brown RW, Thompson MR, Venkatesan R. Magnetic Resonance Imaging: Physical Principles and Sequence Design: John Wiley & Sons Inc.; 1999.
138. Di Mattia C, Balestra F, Sacchetti G, Neri L, Mastrocola D, Pittia P. Physical and structural properties of extra-virgin olive oil based mayonnaise. LWT - Food Science and Technology 2015;62:764-770.
139. Jain RK. Haemodynamic and transport barriers to the treatment of solid tumours. Int J Radiat Biol 1991;60:85-100.
140. Li SP, Padhani AR. Tumor response assessments with diffusion and perfusion MRI. J Magn Reson Imaging 2012;35:745-763.
141. Gerlowski LE, Jain RK. Effect of hyperthermia on microvascular permeability to macromolecules in normal and tumor tissues. Int J Microcirc Clin Exp 1985;4:363-372.
142. Matsuda H, Sugimachi K, Kuwano H, Mori M. Hyperthermia, tissue microcirculation, and temporarily increased thermosensitivity in VX2 carcinoma in rabbit liver. Cancer Res 1989;49:2777-2782.
143. Gnant MF, Noll LA, Terrill RE, Wu PC, Berger AC, Nguyen HQ, Lans TE, Flynn BM, Libutti SK, Bartlett DL, Alexander HR, Jr. Isolated hepatic perfusion for lapine liver metastases: impact of hyperthermia on permeability of tumor neovasculature. Surgery 1999;126:890-899.
144. Kong G, Braun RD, Dewhirst MW. Characterization of the effect of hyperthermia on nanoparticle extravasation from tumor vasculature. Cancer Res 2001;61:3027-3032.
145. Li L, ten Hagen TLM, Bolkestein M, Gasselhuber A, Yatvin J, van Rhoon GC, Eggermont AMM, Haemmerich D, Koning GA. Improved intratumoral nanoparticle extravasation and penetration by mild hyperthermia. Journal of Controlled Release 2013;167:130-137.
146. Craciunescu OI, Thrall DE, Vujaskovic Z, Dewhirst MW. Magnetic resonance imaging: a potential tool in assessing the addition of hyperthermia to neoadjuvant therapy in patients with locally advanced breast cancer. Int J Hyperthermia 2010;26:625-637.

147. Ludemann L, Wust P, Gellermann J. Perfusion measurement using DCE-MRI: implications for hyperthermia. Int J Hyperthermia 2008;24:91-96.
148. Tofts PS, Berkowitz B, Schnall MD. Quantitative analysis of dynamic Gd-DTPA enhancement in breast tumors using a permeability model. Magn Reson Med 1995;33:564-568.
149. Sourbron SP, Buckley DL. Tracer kinetic modelling in MRI: estimating perfusion and capillary permeability. Phys Med Biol 2012;57:R1-33.
150. Tofts PS. Modeling tracer kinetics in dynamic Gd-DTPA MR imaging. J Magn Reson Imaging 1997;7:91-101.
151. Tofts PS, Brix G, Buckley DL, Evelhoch JL, Henderson E, Knopp MV, Larsson HB, Lee TY, Mayr NA, Parker GJ, Port RE, Taylor J, Weisskoff RM. Estimating kinetic parameters from dynamic contrast-enhanced T(1)-weighted MRI of a diffusable tracer: standardized quantities and symbols. J Magn Reson Imaging 1999;10:223-232.
152. Zahra MA, Hollingsworth KG, Sala E, Lomas DJ, Tan LT. Dynamic contrast-enhanced MRI as a predictor of tumour response to radiotherapy. Lancet Oncol 2007;8:63-74.
153. Larsen VA, Simonsen HJ, Law I, Larsson HB, Hansen AE. Evaluation of dynamic contrast-enhanced T1-weighted perfusion MRI in the differentiation of tumor recurrence from radiation necrosis. Neuroradiology 2013;55:361-369.
154. Li SP, Makris A, Beresford MJ, Taylor NJ, Ah-See ML, Stirling JJ, d'Arcy JA, Collins DJ, Kozarski R, Padhani AR. Use of dynamic contrast-enhanced MR imaging to predict survival in patients with primary breast cancer undergoing neoadjuvant chemotherapy. Radiology 2011;260:68-78.
155. Cho N, Im SA, Park IA, Lee KH, Li M, Han W, Noh DY, Moon WK. Breast cancer: early prediction of response to neoadjuvant chemotherapy using parametric response maps for MR imaging. Radiology 2014;272:385-396.
156. Li X, Arlinghaus LR, Ayers GD, Chakravarthy AB, Abramson RG, Abramson VG, Atuegwu N, Farley J, Mayer IA, Kelley MC, Meszoely IM, Means-Powell J, Grau AM, Sanders M, Bhave SR, Yankeelov TE. DCE-MRI analysis methods for predicting the response of breast cancer to neoadjuvant chemotherapy: pilot study findings. Magn Reson Med 2014;71:1592-1602.
157. Intven M, Reerink O, Philippens ME. Dynamic contrast enhanced MR imaging for rectal cancer response assessment after neo-adjuvant chemoradiation. J Magn Reson Imaging 2014.

158. Zheng D, Chen Y, Liu X, Chen Y, Xu L, Ren W, Chen W, Chan Q. Early response to chemoradiotherapy for nasopharyngeal carcinoma treatment: Value of dynamic contrast-enhanced 3.0 T MRI. J Magn Reson Imaging 2014.
159. Park JJ, Kim CK, Park SY, Simonetti AW, Kim E, Park BK, Huh SJ. Assessment of early response to concurrent chemoradiotherapy in cervical cancer: value of diffusion-weighted and dynamic contrast-enhanced MR imaging. Magn Reson Imaging 2014;32:993-1000.
160. Le Bihan D, Breton E, Lallemand D, Aubin ML, Vignaud J, Laval-Jeantet M. Separation of diffusion and perfusion in intravoxel incoherent motion MR imaging. Radiology 1988;168:497-505.
161. Henkelman RM. Does IVIM measure classical perfusion? Magn Reson Med 1990;16:470-475.
162. Le Bihan D, Turner R. The capillary network: a link between IVIM and classical perfusion. Magn Reson Med 1992;27:171-178.
163. Lemke A, Laun FB, Simon D, Stieltjes B, Schad LR. An in vivo verification of the intravoxel incoherent motion effect in diffusion-weighted imaging of the abdomen. Magn Reson Med 2010;64:1580-1585.
164. Luciani A, Vignaud A, Cavet M, Nhieu JT, Mallat A, Ruel L, Laurent A, Deux JF, Brugieres P, Rahmouni A. Liver cirrhosis: intravoxel incoherent motion MR imaging--pilot study. Radiology 2008;249:891-899.
165. Lemke A, Laun FB, Klauss M, Re TJ, Simon D, Delorme S, Schad LR, Stieltjes B. Differentiation of pancreas carcinoma from healthy pancreatic tissue using multiple b-values: comparison of apparent diffusion coefficient and intravoxel incoherent motion derived parameters. Invest Radiol 2009;44:769-775.
166. Sigmund EE, Cho GY, Kim S, Finn M, Moccaldi M, Jensen JH, Sodickson DK, Goldberg JD, Formenti S, Moy L. Intravoxel incoherent motion imaging of tumor microenvironment in locally advanced breast cancer. Magn Reson Med 2011;65:1437-1447.
167. Sumi M, Van Cauteren M, Sumi T, Obara M, Ichikawa Y, Nakamura T. Salivary gland tumors: use of intravoxel incoherent motion MR imaging for assessment of diffusion and perfusion for the differentiation of benign from malignant tumors. Radiology 2012;263:770-777.
168. Federau C, O'Brien K, Meuli R, Hagmann P, Maeder P. Measuring brain perfusion with intravoxel incoherent motion (IVIM): initial clinical experience. J Magn Reson Imaging 2014;39:624-632.

169. Gaing B, Sigmund EE, Huang WC, Babb JS, Parikh NS, Stoffel D, Chandarana H. Subtype differentiation of renal tumors using voxel-based histogram analysis of intravoxel incoherent motion parameters. Invest Radiol 2015;50:144-152.
170. Hijnen NM, Heijman E, Kohler MO, Ylihautala M, Ehnholm GJ, Simonetti AW, Grull H. Tumour hyperthermia and ablation in rats using a clinical MR-HIFU system equipped with a dedicated small animal set-up. Int J Hyperthermia 2012;28:141-155.
171. Ranjan A, Jacobs GC, Woods DL, Negussie AH, Partanen A, Yarmolenko PS, Gacchina CE, Sharma KV, Frenkel V, Wood BJ, Dreher MR. Image-guided drug delivery with magnetic resonance guided high intensity focused ultrasound and temperature sensitive liposomes in a rabbit Vx2 tumor model. J Control Release 2012;158:487-494.
172. Staruch RM, Hynynen K, Chopra R. Hyperthermia-mediated doxorubicin release from thermosensitive liposomes using MR-HIFU: Therapeutic effect in rabbit Vx2 tumours. Int J Hyperthermia 2015;31:118-133.
173. Wijlemans JW, Deckers R, van den Bosch MA, Seinstra BA, van Stralen M, van Diest PJ, Moonen CT, Bartels LW. Evolution of the ablation region after magnetic resonance-guided high-intensity focused ultrasound ablation in a Vx2 tumor model. Invest Radiol 2013;48:381-386.
174. Haacke EM, Filleti CL, Gattu R, Ciulla C, Al-Bashir A, Suryanarayanan K, Li M, Latif Z, DelProposto Z, Sehgal V, Li T, Torquato V, Kanaparti R, Jiang J, Neelavalli J. New algorithm for quantifying vascular changes in dynamic contrast-enhanced MRI independent of absolute T1 values. Magn Reson Med 2007;58:463-472.
175. Thompson HK, Jr., Starmer CF, Whalen RE, McIntosh HD. INDICATOR TRANSIT TIME CONSIDERED AS A GAMMA VARIATE. Circ Res 1964;14:502-515.
176. O'Neill BE, Vo HQ, Shao H, Karmonik C, Zhou X, Li KC. MRI-based prediction of pulsed high-intensity focused ultrasound effect on tissue transport in rabbit muscle. J Magn Reson Imaging 2013;38:1094-1102.
177. Orton MR, Collins DJ, Koh DM, Leach MO. Improved intravoxel incoherent motion analysis of diffusion weighted imaging by data driven Bayesian modeling. Magn Reson Med 2014;71:411-420.
178. Zhang YD, Wang Q, Wu CJ, Wang XN, Zhang J, Liu H, Liu XS, Shi HB. The histogram analysis of diffusion-weighted intravoxel incoherent

motion (IVIM) imaging for differentiating the gleason grade of prostate cancer. Eur Radiol 2015;25:994-1004.
179. Horsman MR. Tissue physiology and the response to heat. Int J Hyperthermia 2006;22:197-203.
180. Tofts PS, Kermode AG. Measurement of the blood-brain barrier permeability and leakage space using dynamic MR imaging. 1. Fundamental concepts. Magn Reson Med 1991;17:357-367.
181. Sourbron SP, Buckley DL. On the scope and interpretation of the Tofts models for DCE-MRI. Magn Reson Med 2011;66:735-745.
182. Pekar J, Moonen CTW, van Zijl PCM. On the precision of diffusion/perfusion imaging by gradient sensitization. Magnetic Resonance in Medicine 1992;23:122-129.
183. Lam MK, Bos C, Moonen CTW, Viergever MA, Bartels LW. Precision and accuracy of intravoxel incoherent motion (IVIM) MRI: Applicability in well-perfused tissues. International Society for Magnetic Resonance in Medicine; 2014; Milan. p 2576.
184. Han M, Rieke V, Scott SJ, Ozhinsky E, Salgaonkar VA, Jones PD, Larson PE, Diederich CJ, Krug R. Quantifying temperature-dependent T changes in cortical bone using ultrashort echo-time MRI. Magn Reson Med 2015.
185. Lam MK, De Greef M, Deckers R, Bartels LW. Feasibility of absolute MR thermometry in bone marrow for MR-guided HIFU of bone metastases. International Symposium for Therapeutic Ultrasound; 2012; Heidelberg.
186. Taylor BA, Elliott AM, Hwang KP, Shetty A, Hazle JD, Stafford RJ. Measurement of temperature dependent changes in bone marrow using a rapid chemical shift imaging technique. J Magn Reson Imaging 2011;33:1128-1135.
187. Ewing JR, Bagher-Ebadian H. Model selection in measures of vascular parameters using dynamic contrast-enhanced MRI: experimental and clinical applications. NMR Biomed 2013;26:1028-1041.
188. de Greef M, Schubert G, Wijlemans JW, Koskela J, Bartels LW, Moonen CT, Ries M. Intercostal high intensity focused ultrasound for liver ablation: The influence of beam shaping on sonication efficacy and near-field risks. Med Phys 2015;42:4685-4697.
189. Ramaekers P, Ries M, Moonen CTW, De Greef M. Improved intercostal HIFU ablation using a phased array transducer based on Fermat's spiral. Internation Symposium of Therapeutic Ultrasound; 2015; Utrecht.

NEDERLANDSE SAMENVATTING

In de oncologie zijn chirurgie, radiotherapie en chemotherapie momenteel de standaard behandelmethodes. Deze methodes worden vaak gecombineerd om de best mogelijke behandeling te geven. Thermische therapie wordt in sommige situaties gegeven als aanvulling. Milde hyperthermie (40°C tot 45°C) induceert fysiologische effecten, zonder directe weefselschade, die gunstig kunnen zijn voor de effectiviteit van radiotherapie en chemotherapie. Ook kan lokale milde hyperthermie worden gebruikt om lokale chemotherapie te bewerkstelligen, met behulp van thermosensitieve liposomen die een chemotherapeuticum bevatten welke vrij komen bij milde hyperthermie. Bij thermische ablatie behandelingen worden tumoren zodanig verhit dat er coagulatieve necrose wordt geïnduceerd.

High intensity focused ultrasound (HIFU) is een nieuwe technologie voor non-invasieve thermische therapie en kan worden gecombineerd met magnetic resonance imaging (MRI). MRI-geleide HIFU (MR-HIFU) biedt de mogelijkheid om tijdens een HIFU behandeling MRI scans te maken, die kunnen dienen voor planning, monitoring en evaluatie. In de MR-HIFU geïnduceerd thermische effecten kan onderscheid worden gemaakt tussen het directe verwarmingsproces en indirecte fysiologische effecten, zoals coagulatie en veranderingen in de bloedtoevoer.

In dit proefschrift is de focus gelegd op MRI methodes voor de evaluatie van MR-HIFU geïnduceerd thermische effecten. Het onderzoek is uitgevoerd in de context van het HIFU-CHEM project, uitgevoerd door een publiek-private consortium, gefinancierd door het Nederlandse Center for Translational Molecular Medicine (CTMM). Het doel van het HIFU-CHEM project was het verder ontwikkelen en testen van een MR-HIFU technologie platform, specifiek voor lokale chemotherapie met thermosensitieve liposomen. Het primaire klinische doel was palliatieve behandeling van pijnlijke botmetastasen.

De meest gebruikte methode in de kliniek voor het monitoren van de MR-HIFU behandelingen is de proton resonantie frequentie shift MR thermometrie (PRFS MRT). Met PRFS MRT kunnen (relatieve) temperatuur-veranderingen worden gemeten met een hoge temporele resolutie. Met de toepassing van MR-HIFU ablatie als palliatieve behandeling van pijnlijke botmetastasen, ontstond er vanuit de kliniek interesse in de kwaliteit en prestatie van PRFS MRT. In **HOOFDSTUK 2** hebben we retrospectief de klinische prestatie geëvalueerd van de PRFS MRT die werd gebruikt voor het monitoren van de MR-HIFU ablatie procedures van deze behandelingen. De belangrijkste bevinding was dat de nauwkeurigheid van de temperatuur metingen werd gehinderd door artefacten. De dominantste artefacten kwamen voort uit de ademhaling van de patiënten en waren zelfs aanwezig op anatomische locaties verder weg van de longen. Daarnaast was de kwaliteit van de beelden variabel tussen verschillende typen laesies en afhankelijk van de hoeveelheid corticale bot.

Een opkomende toepassing van MR-HIFU is tumorbehandeling in abdominale organen. Voor deze toepassing zullen hogere akoestische vermogens en meerdere sonicaties nodig zijn. Hierdoor kan er ongewenste warmteopbouw ontstaan in weefsels buiten het doelgebied, met name in de buikwand. De buikwand bevat zowel een vetlaag als een spierlaag en biedt daarmee de mogelijkheid om de multi-gradient echo (MGE) MRT methode te gebruiken. MGE MRT gebruikt het vet-signaal als referentie voor het water-signaal, waardoor temperatuurmetingen inherent gecorrigeerd worden voor drift in het magnetische veld. Daarnaast kunnen in potentie absolute temperaturen worden gemeten met de methode. In **HOOFDSTUK 3** laten we zien dat MGE MRT opwarmingsprocessen van opeenvolgende sonicaties in beeld kan brengen, zonder last te hebben van drift in het magnetische veld. Ook hebben we het gebruik van MGE MRT tijdens een klinisch MR-HIFU protocol gedemonstreerd in een patiënt. De relatieve temperatuur metingen waren nauwkeurig, echter, de absolute temperatuur metingen toonden systematische fouten.

Voor de berekening van absolute temperaturen met MGE MRT is een kalibratie nodig van de chemische verschuiving tussen water en vet. Echter, deze kalibratiewaarde hangt af van het nucleaire magnetische veld van de twee componenten, waarin variaties kunnen ontstaan door het verschil in

magnetische susceptibiliteit. **HOOFDSTUK 4** beschrijft een studie waarin de invloed van het magnetische susceptibiliteitsverschil tussen water en vet op de MGE MRT methode is onderzocht. Als gevolg van het magnetische susceptibiliteitsverschil wordt de sub-voxel verdeling van magnetische resonantie frequenties aangedaan en daarmee ook het MR signaal van het voxel in het tijdsdomein. Voor dit onderzoek zijn simulaties uitgevoerd met een numeriek fantoom van macroscopisch homogene water-vet systemen. De resultaten laten zien dat het zowel het water- als het vet-signaal een gecombineerd korte en lange tijdsgedrag vertonen, overeenkomend met de theoretische beschrijving van Yablonskiy en Haacke. Aan de hand hiervan zijn drie tijd-bereiken gedefinieerd waarin zowel het water- als vet-signaal of in het korte, of in het lange tijdsregime zit. Door het signaal in een van deze drie tijd-bereiken te bemonsteren, welke gedaan kan worden door de start van het bemonsteren uit te stellen, kunnen fouten in de MGE MRT methode worden gereduceerd. Verder onderzoek is nodig om de implicaties voor macroscopisch heterogene water-vet systemen te begrijpen.

De bovenstaande methoden refereren allen naar thermische ablatie met MR-HIFU. **HOOFDSTUK 5** beschrijft een onderzoek naar de potentie van twee MRI methodes om veranderingen in fysiologische parameters te detecteren als gevolg van MR-HIFU geïnduceerd milde hyperthermie. Dit onderzoek is uitgevoerd in een preklinische setting, met konijnen met geïmplanteerde Vx2 tumoren. Dynamic contrast enhanced (DCE)-MRI is een veelgebruikte methode om maps te maken van parameters gerelateerd aan de permeabiliteit en de bloed volume fractie. Met intravoxel incoherent motion (IVIM)-MRI kunnen maps worden gemaakt van perfusie-gerelateerde parameters, zonder contrastmiddel. De resultaten laten variaties zien in de gevonden veranderingen in parameters tussen konijnen. Dit heeft grotendeels te maken met de heterogeniteit van de groep vóór hyperthermie, in termen van tumorgroei en DCE en IVIM parameter verdelingen. We hebben laten zien dat veranderingen in DCE en IVIM parameters, geïnduceerd door MR-HIFU milde hyperthermie, konden worden gemeten en dat er plausibele verklaringen zijn voor de observaties. De exacte interpretatie van de parameters blijft echter een uitdaging, in het bijzonder wanneer er een mismatch is tussen de fysiologische processen onderliggend aan het MR signaal en de gebruikte modellen.

LIST OF PUBLICATIONS

PAPERS IN INTERNATIONAL JOURNALS

M.K. Lam, C.J.G. Bakker, C.T.W. Moonen, M.A. Viergever, and L.W. Bartels, Short- and long-time signal behavior of randomly distributed water and fat – implications for fat-referenced MR thermometry", *Submitted for publication*

M.K. Lam, C. Oerlemans, M. Froeling, R. Deckers, A.D. Barten-van Rijbroek, M.A. Viergever, C.T.W. Moonen, C. Bos, L.W. Bartels, "DCE-MRI and IVIM-MRI of rabbit Vx2 tumors treated with MR-HIFU induced hyperthermia", *Submitted for publication in a revised version*

M.K. Lam, M. de Greef, J.G. Bouwman, C.T.W. Moonen, M.A. Viergever, and L.W. Bartels, "Multi-gradient echo MR thermometry for monitoring of the near-field area during MR-HIFU heating", Physics in Medicine & Biology, 2015, vol. 60, p. 7729-7746.

M.K. Lam, M. Huisman, R.J. Nijenhuis, M.A.A.J. van den Bosch, M.A. Viergever, C.T.W. Moonen, L.W. Bartels, "Quality of MR thermometry during palliative MR-guided high-intensity focused ultrasound (MR-HIFU) treatment of bone metastases", Journal of Therapeutic Ultrasound, 2015, nr. 5, vol. 3, p. 1-15.

M. Huisman, M.K. Lam, L.W. Bartels, R.J. Nijenhuis, C.T.W. Moonen, F.M. Knuttel, H.M. Verkooijen, M. van Vulpen, M.A.A.J. van den Bosch, "Feasibility of volumetric MRI-guided high intensity focused ultrasound (MR-HIFU) for painful bone metastases", Journal of Therapeutic Ultrasound, 2014, nr. 2, vol. 16, p. 1-10.

Conference Abstracts

M.K. Lam, M. Huisman, R.J. Nijenhuis, M.A.A.J. van den Bosch, C.T.W. Moonen, L.W. Bartels, "Initial Experiences with MR Thermometry During Palliative Treatment of Bone Metastases with MR-HIFU", International Symposium of Therapeutic Ultrasound, 2014.

M.K. Lam, C. Bos, C.T.W. Moonen, M.A. Viergever, L.W. Bartels, "Precision and Accuracy of Intravoxel Incoherent Motion (IVIM) MRI: Applicability in Well-Perfused Tissues", International Society Magnetic Resonance in Medicine, 2014.

M.K. Lam, M. de Greef, L.W. Bartels, "Absolute MR Thermometry for Near-field monitoring during MR-HIFU heating", International Society Magnetic Resonance in Medicine, 2013.

M.K. Lam, M. de Greef, R. Deckers, L.W. Bartels, "Feasibility of absolute MR thermometry in bone marrow for MR-guided HIFU of bone metastases", International Symposium for Therapeutic Ultrasound, 2012.

M.K. Lam, T. Iwabuchi, K. Saito, K. Kuroda, "Echo Time Optimization in Multi-point Dixon Technique for Component Separation in Fat Temperature Imaging", Interventional MRI, 2010.

M.K. Lam, T. Iwabuchi, K. Saito, K. Kuroda, "Effect of Water Resonance Thermal Shift on Methylene T1 Estimation with Multiple Flip Angle Multipoint Dixon Technique for Fat Temperature Imaging", International Society Magnetic Resonance in Medicine, 2010.

"OOK GELOOF IK DAT HET KAN GEBEUREN MEN SLAGE

EN NIET MOET BEGINNEN MET TE WANHOPEN –

OOK AL VERLIEST MEN 'T HIER EN DAAR

EN OOK AL VOELT MEN SOMS EEN SOORT AFTAKELING,

TOCH IS HET ZAAK WEER OP TE LEVEN EN MOED TE VATTEN

AL KOMT HET OOK ANDERS UIT

DAN MEN AANVANKELIJK MEENDE.

...

WANT HET GROOTE GESCHIEDT NIET BIJ IMPULSIE ALLEEN

EN IS EEN AANEENSCHAKELING VAN KLEINE DINGEN

DIE TOT ELKAAR GEBRAGT ZIJN."

– VINCENT VAN GOGH

Uit een brief aan Theo van Gogh
's Gravenhage, zondag 22 Oktober, 1882.
(met toestemming van het Van Gogh museum)

Dankwoord

Wilbert, eens zei je dat wetenschappelijk onderzoek voor jou als het ware een speeltuin was. Die mindset heb ik altijd duidelijk terug gezien in je aanstekelijke enthousiasme en positiviteit. De beren op de weg werden door jou als het ware omgetoverd in schattige teddyberen, waardoor ik weer nieuwe moed kreeg. Tegelijkertijd was jouw behoedzaam kritische houding sturend. We konden goed praten, zowel op de inhoud als over de verschillende processen die ik tijdens mijn promotietraject heb doorgemaakt. Ik heb onze gesprekken als ontspannen en prettig ervaren, zowel in de makkelijkere als in de minder makkelijke periodes van mijn promotie-traject. Wilbert, bedankt!

Max, zo complex als een promovendus wetenschap kan maken in de diepte van de inhoud, zo helder kun jij het weer vertalen in overzichtelijke abstractie. Jouw ervaring en kennis in de wonderlijke wereld genaamd "de wetenschap", zowel op inhoudelijk vlak als op proces-niveau, is werkelijk inspirerend. Max, hartelijk dank voor het vertrouwen.

Chrit, ondanks je uitgebreide ervaring en kennis, je positie in de internationale kringen, ben je de bescheidenheid zelve. Benaderbaar en open voor ieders idee en visie. Ik heb veel bewondering voor de manier waarop je dichtbij jezelf blijft. Dank je wel voor je betrokkenheid en vertrouwen.

Kagayaki, thank you for leading my first steps in the MR thermometry research. It was an honor to have learned my first research skills from you. Thank you for the confidence and for keeping in touch. I am delighted to have you in my PhD committee.

Chris Bakker, al sinds het eerste college dat je me gaf vond ik je een inspirerende, pure wetenschapper, en dat vind ik nog steeds. Hartelijk dank voor je onuitputtelijke energie en bereidheid om mee te denken.

Clemens, jouw vermogen om continu te denken in realistische oplossingen zorgde altijd voor een frisse wind in de soms onmogelijk lijkende uitdagingen. Ik heb heel veel van je geleerd: effectief aanpakken van besprekingen, creatieve experimentele set-ups, het omdoen van een luier, om maar wat te noemen. Dank je wel.

"Konijnenteam" was mijn koosnaam voor het prettige samenwerkingsverband in de pre-klinische setting. Chris Oerlemans, "de konijnenman" zoals ik je noemde voor mensen die jou niet kenden, je hield altijd mijn energiepeil in het oog, dank je wel daarvoor. Angelique, bedankt voor je vrolijke en energieke inzet, op ieder willekeurig tijdstip van de dag. Nico en de anderen van het GDL, bedankt voor het mogelijk maken wat onmogelijk leek.

Merel, Robbert en Maurice, als "technische nerd" vond ik het erg waardevol om met jullie samen te werken. Het was leerzaam om bij de klinische behandelingen en voorbesprekingen aanwezig te zijn. Jullie perspectieven vanuit de klinische hoek hebben mijn visie verbreed, bedankt. Marlijne, bedankt voor je flexibiliteit en de ruimte om mijn scan te draaien bij de myoombehandelingen. Niels, Greet, Jörgen en Laura, bedankt dat jullie als ervaren MR laboranten altijd mee dachten en open stonden voor mijn ideeën als jonge wetenschapper; ik heb heel veel waardering voor jullie.

Martijn Froeling, bedankt voor de goede samenwerking en inhoudelijke discussies. Martijn de Greef, bedankt voor het meedenken en je behulpzaamheid. Mario and Gerald, thank you for all the times you saved me from hard- and software failures and stress. Roel, bedankt voor de waardevolle, interessante en gezellige discussies.

Dick en alle medewerkers van Keurslager Van Schip, hartelijk dank voor de behulpzaamheid, het meedenken en de flexibiliteit. Elke keer als ik wat kwam ophalen was weer een vrolijk begin van lange experimenten. Dank jullie wel!

OiO-stegers, dank voor de gezelligheid bij lunches, koffiepauzes en borrels!

Hendrik, bedankt voor je rol als MRfys-vraagbaken en als ervaringsdeskundige; jouw woorden "Het hoort bij promoveren, je komt er bovenop, ja écht." heb ik als een soort van mantra's tegen mezelf herhaald – en je had gelijk.

Pim en Lisette, als kamergenoten hebben jullie de vele stemmingen die mijn promotietraject rijk was meegekregen. Bedankt voor de ruimte, het luisteren en de gezellige, fijne sfeer! Chantal, bedankt voor je fijne gezelschap en luisterend oor tijdens congressen!

Job en Sjoerd, wat fijn dat ik altijd mocht binnenlopen om van gedachten te wisselen als ik weer eens vastliep in één of ander kronkel, of gewoon voor de gezelligheid! (Yinghe, sorry for the noise every time I came into your room to talk to those two; thank you for your tolerance!) Job, bedankt voor al je fancy scriptjes en prachtige krabbels en schetsjes (en voedsel), ongeacht hoe druk je het zelf had! Sjoerd, bedankt voor alle relativerende gesprekken en steun in zware tijden. Wat fijn dat je ook tijdens mijn verdediging naast me staat! Dank jullie wel, jullie zijn toppers!

Yolanda, wat was het heerlijk om alle lief en leed van het promoveren, maar ook alles daar buiten, met je te kunnen delen! Ochtendhumeuren, mislukte experimenten, falende computers, wanhoop tot in tranen toe; al hardop klagend konden we alles weer relativeren (of de vacature bij de supermarkt overwegen). Wat een geluk om met een goede vriendin de werkkamer te mogen delen tijdens mijn promotietraject! Geen idee hoe ik het had volgehouden zonder jou en ik ben blij dat je tijdens de verdediging naast me staat! Yol, bedankt voor alles!!

Kirsten, in de zwaarste periode was het moeilijk om me constant weer te herpakken. Jouw steun en vriendschap heeft me geholpen mezelf er doorheen te slepen. Duizendmaal dank Kirst!

Pieter, dank je wel voor je onvoorwaardelijke liefde, geduld en steun. Dankzij jou kan ik elke dag weer met nieuwe moed beginnen. Jij hebt me geleerd de positieve dingen te benoemen, waardoor ik in ging zien dat ik best wel zinnige dingen deed achter mijn stoffige bureau. Blij leren zijn met subdoelen en tussenresultaten binnen een immens project, genaamd het promotieonderzoek. Lieve Pieter, dank je wel dat je er altijd voor me bent!

Lieve pap en mam, van jullie heb ik geleerd wat doorzettingsvermogen is: dat wat er ook gebeurt, je verder moet én kunt. En ook al was het lastig voor te stellen wat mijn werk inhield, jullie hebben me altijd gesteund. Braaf kijkend naar een of andere powerpoint die ik graag wilde laten zien, of knikkend een eindeloos verhaal aanhoren dat niet te volgen was. Zoals mama altijd zei, 對牛彈琴. Juist jullie onbevangenheid en nuchtere houding blijven mij eraan herinneren dat “succesvol zijn” subjectief is en geluk in vele factoren te vinden is!

"I WAS BORN NOT KNOWING

AND HAVE HAD ONLY LITTLE TIME TO CHANGE THAT HERE AND THERE"

– *RICHARD P. FEYNMAN*

Curriculum Vitae

Mie Kee Lam was born on 17 July 1986 in Amersfoort, The Netherlands. From 2005 to 2008, she studied Physics (BSc) at Utrecht University. During her BSc research at the Biophysics department, she first experienced the joy of a multidisciplinary environment. From 2008 to 2010 she studied Biomedical Image Sciences (MSc) at Utrecht University with a focus on MR physics. She performed her MSc research on MR thermometry in Japan, under supervision of Kagayaki Kuroda. After graduation, she started her PhD at the University Medical Center Utrecht, of which the most important findings are presented in this thesis.